The Combined Use of Optical and SAR Data for Large Area Impervious Surface Mapping

Masterarbeit

zur Erlangung des Mastergrades
an der Naturwissenschaftlichen Fakultät der
Paris-Lodron Universität Salzburg

eingereicht von

Patrick Leinenkugel

Gutachter:

Prof. Dr. Blaschke

Fachbereich:
Geologie und Geographie

Salzburg, August 2010

Abstract

One of the megatrends marking our societies today is the rapid growth of urban agglomerations which is accompanied by a continuous increase of impervious surface (IS) cover. In light of this, accurate measurement of urban IS cover as an indicator for both, urban growth and environmental quality is essential for a wide range of urban ecosystems studies. The aim of this work is to present an approach based on both optical and SAR data in order to quantify urban impervious surface as a continuous variable on regional scales. The method starts with the identification of relevant areas by a semi automated detection of settlement areas on the basis of single-polarized TerraSAR-X data. Thereby the distinct texture and the high density of dihedral corner reflectors prevailing in build-up areas are utilized to automatically delineate settlement areas by the use of an object-based image classification method. The settlement footprints then serve as reference area for the impervious surface estimation based on a Support Vector Regression (SVR) model which relates percent IS to spectral reflectance values. The training procedure is based on IS values derived from high resolution QuickBird data. The developed method is applied to SPOT HRG data from 2005 and 2009 covering almost the whole are of Can Tho Province in the Mekong Delta, Vietnam. In addition, a change detection analysis was applied in order to test the suitability of the modelled IS results for the automated detection of constructional developments within urban environments. Overall accuracies between 84 % and 91% for the derived settlement footprints and absolute mean errors below 15% for the predicted versus training percent IS values prove the suitability of the approach for an area-wide mapping of impervious surfaces thereby exclusively focusing on settlement areas on the basis of remotely sensed image data.

Tóm lược

Một trong những xu hướng đánh dấu sự phát triển của xã hội chúng ta ngày nay là sự phát triển các quần thể đô thị, điều này đồng nghĩa với việc tiếp tục gia tăng độ che phủ bề mặt không thấm nước (IS). Do đó, việc đo đạc chính xác IS là một chỉ số cần thiết cho các nghiên cứu về phát triển đô thị, chất lượng môi trường cũng như hệ sinh thái đô thị. Mục tiêu của nghiên cứu này là trình bày một phương pháp xác định IS một cách định lượng dựa trên cả hai loại dữ liệu quang học và SAR ở quy mô khu vực. Phương pháp bắt đầu với việc xác định các khu vực dân cư có liên quan bằng phương pháp xác định bán tự động dựa trên dữ liệu TerraSAR-X, bằng cách đó, cấu trúc riêng biệt và có mật độ cao của góc nhị diện phản chiếu chiếm ưu thế trong các khu vực xây dựng được sử dụng để mô tả một cách tự động các khu vực dân cư bằng việc sử dụng phương pháp phân loại ảnh dựa trên đối tượng (object-based). Dấu vết của khu dân cư được sử dụng như là vùng tham khảo cho việc ước đoán IS dựa trên mô hình Support Vector Regression (SVR), mô hình này liên quan đến phần trăm diện tích IS và giá trị phản chiếu phổ. Phương pháp đã được phát triển và được áp dụng cho dữ liệu SPOT HRG từ năm 2005 và năm 2009, bao phủ gần như toàn bộ thành phố Cần Thơ, ở đồng bằng Sông Cửu Long, Việt Nam. Thêm vào đó, phân tích xác định thay đổi đã được ứng dụng để kiểm chứng sự thích hợp của mô hình làm cơ sở cho việc xác định tự động sự phát triển xây dựng trong môi trường đô thị. Độ chính xác toàn phần từ 84% đến 91% cho việc xác định dấu vết của khu dân cư, và giá trị sai số trung bình tuyệt đối dưới 15% của kết quả ước đoán so với phần trăm giá trị thực địa IS chứng tỏ sự phù hợp của phương pháp cho việc thành lập bản đồ bề mặt không thấm nước khu vực rộng lớn dựa trên dữ liệu viễn thám.

Acknowledgements

At this point, I would like to thank all those who have supported me throughout the duration of this thesis.

I would like to express my deep appreciation to Professor Dr. Thomas Blaschke for his valuable advice, friendly help and willingness to evaluate this thesis.

The thesis was written at the German Remote Sensing Data Center (DFD), an institute of the German Aerospace Center (DLR). In this connection, I would like to express my sincere gratitude to my supervisor Dr. Thomas Esch, leader of the team "Urban Areas and Land Management". His personal guidance provided a sound basis for the successful execution of this study.

In addition, the study was carried out within the framework of the German-Vietnamese WISDOM project. I am therefore deeply grateful to Dr. Claudia Künzer, project leader of the WISDOM project and leader of the team „Land Surface Dynamics". Her personal interest, expertise and guidance were invaluable to the completion of this thesis.

Furthermore, I am very grateful to the whole WISDOM team at the DFD, in particular to Juliane Huth, Dr. Steffen Gebhardt and Dr. Thilo Wehrmann who supported me in many ways during my work period at the DFD.

I would especially like to thank Tuan Vo Quoc who helped me a lot during my stay in Vietnam and who kindly translated the abstract of this thesis into Vietnamese.

Last but not least, I wish to express my deepest gratitude to my parents for their dedication and moral encouragement throughout the entire period of my studies.

List of Figures

Chapter 1: Introduction

Chapter 2: Theoretical Background

Chapter 3: Study Area

Chapter 4: Materials and Preprocessing

Chapter 5: Methodology

Chapter 6: Results

Chapter 7: Discussion

Chapter 8: Outlook

List of Tables

Chapter 1: Introduction

Chapter 2: Theoretical Background

Chapter 4: Materials and Preprocessing

Chapter 5: Methodology

Chapter 6: Results

Chapter 7: Discussion

Abbreviations

ATM	Atmospheric correction
B1/B05/B0	Bare soil assigned impervious/intermediate/pervious
BGIS	Ball's Global Imaging System
C	Coefficient of Variation
CART	Classification and Regression Tree
CNES	Centre National d'Etudes Spatiales
CORINE	Coordinated Information on the European Environment
C_{th}	Scene specific speckle heterogenity
C_{xy}	Local image heterogeneity
DBC	Distinct Backscattering Centre
DFD	German Remote Sensing Data Centre of the DLR
DLR	German Aerospace Centre
DN	Digital number
D_{xy}	Local speckle Divergence
EADS	European Aeronautic Defence and Space Company
EBU	Enclosed by Urban
EMR	Electromagnetic Radiation
ETM+	Enhanced Thematic Mapper Plus
GHz	Gigahertz
GIS	Geographic Information System
GPS	Global Positioning System
GUA	Group Urban Area
GUF	Group Urban Footprint
GUS	Group Urban Structures
HH	Horizontal send, horizontal receive (polarisation)
HIS	Histogram Matching
HRG	Haute Resolution Geometrique
HSI	Hue-Saturation-Intensity
HV	Horizontal send, vertical receive (polarisation)
IN-SAR	Interferometric Synthetic Aperture Radar
IS	Impervious Surface
I_{xy}	Intensity value
LOO	Leave One Out
LOS	Line of sight
LSMA	Linear Spectral Mixture Analyses
LULC	Land-use/Land-cover
LUT	Look-up table

MAE	Mean Absolute Error
MAUP	Modifiable Arial Unit Problem
MAX	Maximum
ME	Mean Error
MGD	Multi-look ground range detected
MIN	Minimum
MODTRAN	Moderate resolution atmospheric transmission
N	Eqivialent number of looks
NDVI	Normalized Difference Vegetation Index
NIR	Near-Infrared
NPS	Nonpoint Source Pollutants
OBIA	Object based image analyses
ORG	Original
PUS	Potential Urban Structures
QB	QuickBird
R^2	Coefficient of Determination
RAR	Real Aperture Radar
RMSE	Root Mean Square Error
SAR	Synthetic Aperture Radar
SD	Standard Deviation
SFIM	Smoothing Filter-based Intensity Modulation
SM	Stripmap
SPOT	System Probatoire d'Observation de la Terre
SRM	Structural Risk Minimisation
SVM	Support Vector Machines
SVR	Support Vector Regression
SWIR	Short Wave Infrared
TIFF	Tagged Image File Format
TM	Thematic Mapper
TSX	TerraSAR-X
UA	Urban Area
UN-HABITAT	United Nations Human Settlements Programme
UTM	Universal Transverse Mercator
VH	Vertical send, horizontal receive (polarisation)
VHR	Very high resolution
VIS	Vegetation-Impervious surface-Soil
VNIR	Visible and Near-Infrared
VV	Vertical send, vertical receive (polarisation)
W1/W05/W0	Water assigned impervious/intermediate/pervious
WGS	World Geodetic System

Contents

Chapter 1

Introduction

One of the megatrends marking our societies today is the worldwide growth of the urban population in comparison to the number of people living in rural environments (TIBAIJUKA 2008). Particularly from 1950 onwards, urban growth intensified raising the proportion of people living in cities from one-third to one half in 2000 and will presumably further rise to two-thirds of the global population by 2050 (see FIG. 1-1). Alongside the indisputable advantages of this trend, the continuous growth of urban environments also brings irreversible changes in consumption and production patterns relating to land, water and other natural resources, which may have an adverse impact on the ecosystem as a whole (TIBAIJUKA 2008).

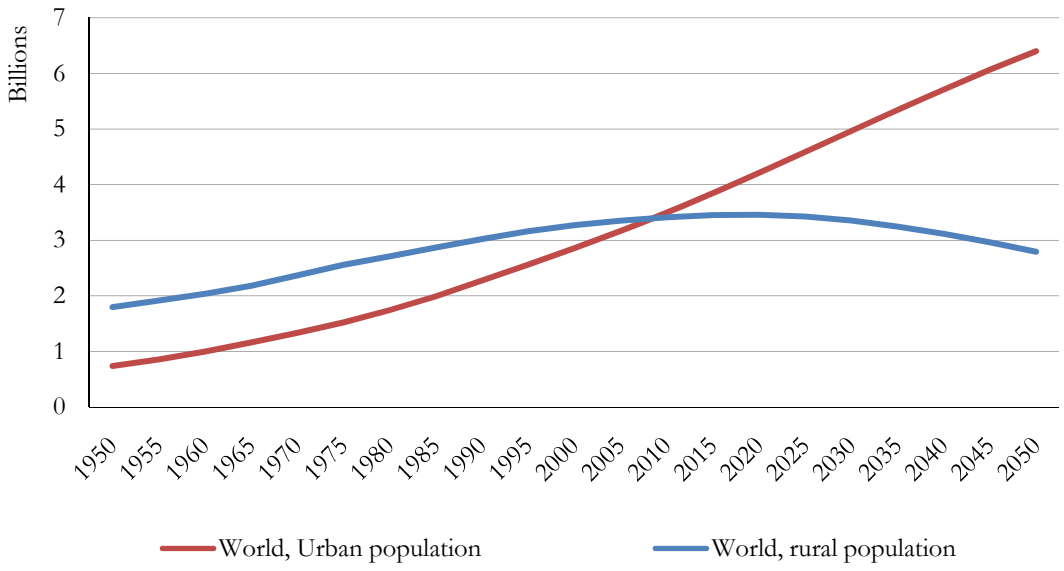

Fig. 1-1: World urbanisation prospects.

Source: UN-HABITAT (2010)

In view of these developments, a timely and accurate estimation of both urban growth and its effects on the environment is essential for a sustainable, responsible urban development and planning (JAT ET AL. 2008, PRASADA MOHAPATRA AND WU 2007).

In this respect, impervious surface (IS) cover has become established as a well-accepted indicator for analyzing the spatial and temporal dynamics of urban growth. Furthermore, impervious land cover also has emerged as an important environmental indicator, as it contributes significantly to the environmental impacts of urbanization (ARNOLD and GIBBONS 1996).

1.1 Impervious surface - an anthropologic and environmental indicator

Impervious surfaces can be defined as any surface cover that prevents the infiltration of water into the soil and is primarily associated with anthropogenic altered surfaces such as those related to transportation (streets, highways, parking lots, driveways, sidewalks etc.) and building rooftops (YUAN AND BAUER 2007, WENG 2007, LU AND WENG 2006, BAUER ET AL. 2007). Beside these most prevalent and easily identified types, compacted soil can also be considered as an impervious surface (ARNOLD and GIBBONS 1996).

Since most of these are man-made ground covers related to the development of residential, commercial or industrial areas, IS cover information is used in many urban modelling studies by city planners, economists and resource managers to analyse settlement patterns, to assess future growth and to create planning scenarios (HEROLD ET AL. 2003). Furthermore, a lot of studies deal with the correlation between IS cover and population density such as LU, WENG and LI (2006), who relate the degree of imperviousness in residential areas to census data, in order to determine population estimations. In combination with other statistical parameters such as socio-economic data, IS information may also provide an indicator for the quality of life within urban environments as reported by LI and WENG (2007).

On the other hand, with the emergence of urban sprawl many studies have recognized the potential of impervious coverage information as a valuable and cost-effective means for assessing environmental quality (ARNOLD AND GIBBONS 1996, BRABEC ET AL. 2002). With increasing proportions of sealed ground cover, natural soil functions are significantly restricted thereby substantially affecting the way that water is transported and stored within the water cycle (ARNOLD and GIBBONS 1996). Due to obstructed infiltration, the propor-

tion of impervious surface cover within an area bears a direct relation to the volume, duration and intensity of urban runoff and has an indirect relation to groundwater recharge and base flow (see FIG. 1-2) (WENG 2007). In addition, storm flows and floods occur more frequently which reach their peaks more rapidly than is the case in rural areas(Arnold and Gibbons 1996). The intensification of land use and the increase in urban features such as buildings and transport structures lead to a corresponding increase in so-called nonpoint source pollutants (NPS), which refer to pollutants from many diffuse sources, including pathogens, nutrients, toxic contaminants and debris (ARNOLD and GIBBONS 1996, WENG 2007). The increased runoff then transports these pollutants directly or indirectly into waterways or groundwater, which threaten the health of aquatic organisms and their human consumers (PRASADA MOHAPATRA and WU 2007, ARNOLD and GIBBONS 1996, BRABEC et al. 2002, WENG 2007).

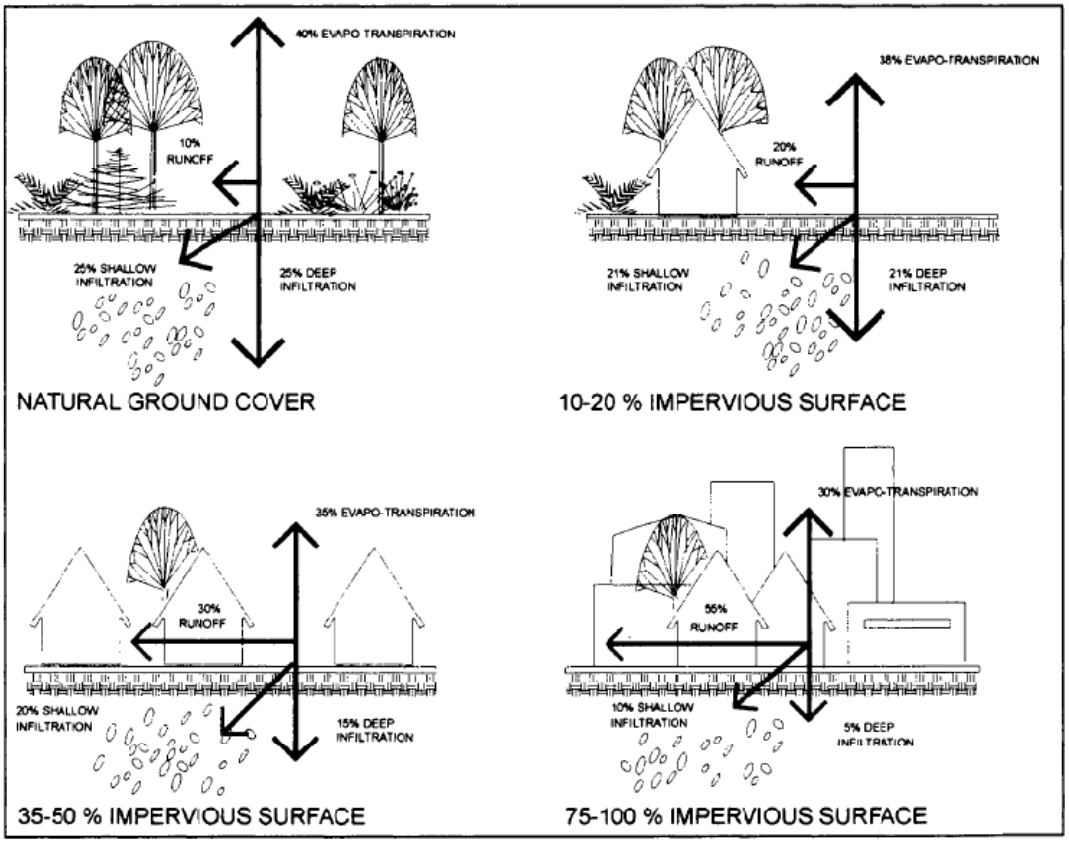

Fig. 1-2: Relation between impervious surface cover, infiltration and urban runoff.

Source: ARNOLD and GIBBONS (1996)

Alongside the impact that impervious surfaces have on hydrologic-related aspects of the environment, the effects on urban climatology must be also be taken into account. High proportions of non-evaporating, impervious materials increase sensible heat fluxes at the expense of latent heat fluxes within the urban canopy (YUAN and BAUER 2007). In addi-

tion, anthropogenic heat generated by traffic, industry and domestic buildings also heat up the urban environment. Thus, the extent and spatial occurrence of impervious surface areas may also be indicative of urban heat island effects (PRASADA MOHAPATRA and WU 2007, HU and WENG 2009, WILSON et al. 2003, YUAN and BAUER 2007, WENG 2007, YANG et al. 2003). Furthermore, as increasing proportions of IS inevitably lead to a decrease in agricultural land and natural habitat, many studies have observed a loss in biodiversity as well as a deterioration in habitat quality on land and in water (BOLAY et al. 1997, LU and WENG 2006, LU et al. 2006, CABLK and MINOR 2003, GOETZ and FISKE 2008)

1.2 Previous studies of impervious surface estimation

A wide range of techniques exists for estimating and mapping impervious surface. The appropriate method however, depends on the size of the area being considered and the degree of accuracy being required. Since the latter is generally related to the time, effort and financial resources available, the larger the area is to be investigated, the more cut backs have to be made on the level of accuracy to be obtained. The most accurate results are achieved by on-site measurements using surveying equipment such as GPS. However, due to the intensive efforts involved in collecting the data, this method is only practicable for site level applications (ARNOLD and GIBBONS 1996). The manual digitizing of impervious surface cover from detailed hard-copy maps or high resolution aerial photographs provides an efficient approach for local or community-scale areas, this is however expensive and time consuming for regional or national scales (BRABEC et al. 2002, ARNOLD and GIBBONS 1996). This method has been the main approach until the 1970s and 1980s, but with the emergence of more efficient techniques in digital image processing and the development of new satellite sensors the interest in automated methods, based on remotely sensed satellite images, has rapidly increased (WENG 2007). Satellite-based approaches may provide a better compromise between accuracy and cost compared to conventional surveying and mapping techniques, with respect to large area impervious surface analyses (ARNOLD and GIBBONS 1996). Furthermore, the aerial view facilitates uninterrupted broad area surveying, which is not obstructed by access restrictions to private ground. Moreover, remote sensing allows a retrospective look at the subject matter by means of archive material enabling change to be documented and comparisons to be drawn.

In order to take advantage of the extensive coverage of satellite images, most studies in this field facilitate sensors with spatial resolution between 10-100m, such as the Landsat

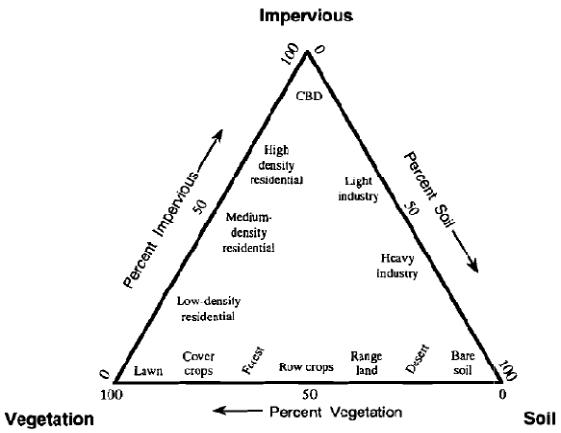

Fig. 1-3: Some examples of urban and near-urban features placed in the ternary V-I-S model
Source: RIDD (1995)

TM/ETM+ sensors (see TABLE 1-1) featuring spatial resolutions between 30-60m and swath widths of 185 km. However, the primary drawback with the application of medium resolution image data to urban settings is the so called mixed pixel problem. Medium resolution imagery is regarded as too coarse with respect to the heterogeneity of urban landscapes (WENG 2007). Within the extent of one pixel, various types of impervious ground coverage may be mixed with pervious land-cover types such as trees or grass patches and consequently cannot be extracted and quantified unambiguously (see CHAPTER 2.2). The description of urban areas through a combination of impervious surface materials, green vegetation and bare soil as the main land-cover components of urban ecosystems was proposed by RIDD (1995) who developed a vegetation-impervious surface-soil (VIS) model (see FIG. 1-3) for standardised urban ecosystem analysis.

To overcome the difficulties posed by mixed pixels, many image processing methods have been developed which aim to estimate subpixel imperviousness, implying the proportion of impervious ground cover within the extent of one resolution cell. TABLE 1-1 lists the different methods and sensors used in impervious surface studies which have been published in two popular journals[1] in the field of remote sensing over the last five years. These studies can be categorized according to the main methodical concepts of impervious surface analyses into image classification, multiple regression, linear spectral mixture analyses and machine learning algorithms.

Methods based on image classification link characteristic degrees of imperviousness to land-use/land-cover (LULC) categories to produce average per-class estimates. Thereby LULC information can either be derived from prior image classification or from already existing geodata, such as CORINE land-cover classes or AKTIS vector data. A major issue is the defining of the key determinant, i.e. the percentage imperviousness per land use category, which can vary significantly between the individual studies such as shown in

[1] Remote Sensing of Environment, International Journal of Remote Sensing

Table 1-2, as a result of the different methods used to derive these averages (BRABEC et al. 2002). DOUGHERTY et al. (2004) compared a traditional approach of visual estimation of IS cover per land-use class from aerial photography, with an automated approach based on a decision tree classifier applied to satellite data. They concluded that accuracy in IS cover estimations can significantly vary according to the number of land-use classes applied and thus, recommended the latter approach as more favourable. Another approach based on land-use classification which is generally used for large areas assessments, is to broadly assume 100% imperviousness for all categories related to urban land-use such as carried out by SIEDENTOP and FINA (2008) or MEINEL et al. (2007). These approaches however focus on small scale land-use analyses rather than on the estimation of actual degrees of impervious surface. Generally, methods based on classification only provide a lumped measure of imperviousness per LULC class and do not provide spatially detailed (at the pixel resolution) estimates of imperviousness (CHABAEVA ET AL. 2007), as do the other methods mentioned below.

Table 1-1: Recent studies of impervious surface analyses including sensors and main methodical concept

SENSORS	MAIN CONCEPT	AUTHORS
Landsat ETM+	Regression tree modelling	Xian and Crane (2005)
Landsat ETM+	Linear spectral mixture analysis	Lu and Weng (2006)
Landsat ETM+	Linear spectral mixture analysis	Powell et al. (2007)
Landsat ETM+	Linear spectral mixture analysis	Lu et al. (2006)
Landsat ETM+	Linear spectral mixture analysis	Lee and Lathrop (2005)
Landsat ETM+	Linear spectral mixture analysis	Yuan and Bauer (2007)
Landsat ETM+	Linear spectral mixture analysis	Li and Weng (2007)
Landsat ETM+	Image classification	Powell et al. (2008)
Landsat ETM+	Linear regression and decision tree modelling	Goetz and Fiske (2008)
ASTER	Neural networks, linear spectral mixture analysis	Pu et al. (2008)
EO-1 ALI	Linear spectral mixture analysis	Weng et al. (2008)
ASTER	Artificial neural networks	Hu and Weng (2009)
Landsat ETM+	Support Vector Regression	Esch et al. (2009)
Airborne	Support Vector Machines	Van der Linden and Hostert (2009)
IKONOS	Decision tree classifier, linear spectral mixture analysis	Lu and Weng (2009)
IKONOS	Linear spectral mixture analysis	Wu (2009)
SPOT5, ERS-2	Classification and regression tree modelling	Jiang et al. (2009)
Landsat ETM+	Linear spectral mixture analysis	Myint and Okin (2009)
Landsat ETM+	Linear spectral mixture analysis	Weng and Lu (2009)
Landsat ETM+	Linear spectral mixture analysis	Van de Voorde et al. (2009)
ASTER	Linear spectral mixture analysis	Weng et al. (2009)
Landsat ETM+	Image classification	Luo and Mountrakis (2010)

Table 1-2: Percent impervious area ascribed to various land use categories, used in various studies

	Percentage TIA							
Land Use Category	Cooper (1996)[a]	Taylor (1993)[b]	Alley and Veenhuis (1983)[c]	City of Olympia (1995)[d]	Stankowski (1972)[e]	Griffin et al. (1980)[f]	USDA (1986)[g]	Rouge Program Office (1994)[h]
Agricultural land/ open space	5	2-5	—	—	0	—	—	1.9-2.0
Public and quasi-public	—	—	—	—	50-75	—	—	—
Parks	5	5	—	—	0	—	—	10.9
Golf courses	5	20	—	—	—	—	—	—
Low-density single-family residential	10	< 15 (< 1 u/ac.)		—	12	14-19 (0-2 u/ac.)	12 (1 u/2 ac.)	18.8
Medium-density single-family residential	35	20 (1-3 u/ac.)	13-16 (1-2 u/ac.)	—	25	34-42 (2-8 u/ac.)	20 (1 u/ac.)	37.8
"Suburban" density 4 u/ac.	—	—	22-31 (2-4 u/ac.)	—	—	—	25	—
High-density single-family residential	60	40 (3-7 u/ac.)	30-49 (> 4 u/ac.)	40 (3-7 u/ac.)	40	25-48 (8-22 u/ac.)	30 (3 u/ac.) 38 (4 u/ac.)	51.4
Mobile homes	—	70	—	—	—	—	—	—
Multifamily	—	80 (> 7 u/ac.)	53-64	48 (7-30 u/ac.)	60-80	47-65 (> 22 u/ac.)	65 (8 u/ac.)	—
Commercial	90	60-90	66-98	86	80-100	89-96	85	56.2
Industrial	—	—	60	—	40-90	—	72	75.9
Highways	100	100	—	—	—	—	—	52.9
Construction site	—	50	—	—	—	0	77	—

Source: BRABEC et al. 2002

The multiple regression approach relates impervious surface cover to remote sensing variables. Thereby, in most cases the strong inverse proportional relationship between vegetation and impervious surface fraction is utilized (see FIG. 1-3). ALLEN, PATKI and PASULA (2007) classified the range of the Normalized Difference Vegetation Index (NDVI) (see CHAPTER 2.2) into seven classes and assigned a common IS value to each class. They recommend this technique as preferable to other analytical techniques, such as analyses based on automated land-cover classifications. BAUER et al. (2007) used a linear regression model to derive subpixel IS estimates as a continuous variable, based on the inverse relation of imperviousness with the greenness component of the Tasseled Cap Transformation of Landsat TM/ETM+ data. The agreement between the reference and the estimated IS area resulted in a coefficient of determination (R^2) ranging from 0.80 to 0.94 which however was highly dependent on seasonal variability. Alongside spectral reflectance characteristics, geographic information system (GIS) variables can also be used as reported by CHABAEVA et al. (2007). They used a regression model with land-cover and population density data as independent variables to estimate percent imperviousness, resulting in a higher accuracy (Root Mean Square Error (RMSE) of 4.56) compared to a comparable Classification and Regression Tree (CART) sub-pixel analysis (RMSE of 5.48).

One of the most popular approaches generally used to account for the mixed pixel problem are Linear Spectral Mixture Analyses (LSMA). The concept of LSMA assumes that the total measured spectrum of a mixed pixel is the sum of the spectra of all land-cover components, weighted by their respective fractions (ADAMS and GILLESPIE 2005). When the characteristic spectra of the pure land cover materials (endmembers) are known, it is then possible to quantify the proportions of the mixture constituents forming the aggregated spectrum of a pixel. With respect to impervious surface estimation, different approaches of LSMA are employed. LEE and LATHROP (2005) for example, directly extracted impervious surface as one of the endmembers by applying a LSMA to Landsat ETM+ imagery, in order to extract impervious surface, managed/unmanaged lawn and tree cover as key land-cover components in an urban/suburban setting. Also MYINT and OKIN (2009) similarly extracted impervious surface cover directly as an endmember together with the other fractions i.e. vegetation, bare soil and shade. Thereby, IS proportions resulted in a Pearson correlation of 0.86 when compared to reference information derived from high resolution QuickBird data. Another approach is to derive fraction images, which are subsequently used to compute impervious surface proportions. LU and WENG (2007) for instance, estimated impervious surface by the use of an LSMA approach by extracting four endmembers, namely vegetation, high-albedo, low albedo and soil from Landsat Etm+ imagery. Finally, impervious surface cover was extracted from the high- and low-albedo fraction images by using the distinct land surface temperature characteristic of built-up areas, taken from the Landsat ETM+ thermal band. A comparison of the resulting IS fraction image with reference data from orthophotographs resulted in an RMSE of 9.22%.

The main methods for impervious surface estimation based on advanced machine learning algorithms include classification and regression tree classifier (CART), artificial neural networks (ANN) or Support Vector Machines (SVM). These kinds of statistical models use sophisticated algorithms, based on repeated learning from training data, in order to model complex relationships between input and output values (ROGAN et al. 2008). Within the CART approach, a rule-based binary decision tree recursively splits the training data into smaller subsets which are then used for the prediction of continuous variables. In this manner, nonlinear relationships between predictive and target variables can be taken into account with the potential of producing better results compared to the simple linear regression models. XIAN (2007) for example, used Landsat ETM+ reflectance, thermal bands and the NDVI together with other geoinformation such as slope as independent variables, while a set of training IS values formed the dependent variable in a CART model. Differ-

ences between modelled and true IS cover ranged from 15.1 to 16.1 for the RMSE. Artificial neural networks (ANN) are non-linear, statistical models simulating the fundamental functionality of biological neural networks by an interconnected and cascaded set of functions (nodes) represented in a network structure. PU et al. (2008) used a ANN to derive the fractions of four endmembers including high and low albedo impervious surfaces from ASTER VNIR and SWIR mixed pixels. Thereby, the input nodes are connected to the reflectance of the ASTER bands, while the nodes of the output layer result in a vector that corresponds to the fractions of the endmembers within a pixel. Results of the spectral mixture analysis were obtained with reasonable accuracy, showing an R^2 of 0.73 for the impervious surface fraction. Especially nonlinear mixtures between the soil and impervious surfaces fractions were handled with higher accuracy compared to linear regression methods, due to the nonlinear nature of the ANN.

1.3 Research Objectives

ESCH et al. (2009, 2007) developed an approach for impervious surface estimation by using a Support Vector Regression (SVR) model which correlates impervious surface values to the spectral characteristics of Landsat7 ETM+ pixels. SVR generally produce better results compared to conventional regression models due to their special kind of statistical machine learning algorithms, the functionality of which is explained in detail in CHAPTER 0. As the approach has been developed for large area analyses on a regional or national scale, additional geodata is required to limit the modelling process to the actual areas of interest, namely areas related to residential, industrial and commercial, or transportation land use. As a result, this approach is only feasible for areas where this kind of land-use data is readily available. The methodical transfer to other regions can therefore pose a difficult challenge, particularly in developing countries which frequently only have an insufficient or decentralised geodata infrastructure.

This thesis therefore, aims to provide a comprehensive approach for large area impervious surface mapping which is solely based on remotely sensed imagery and thus, can be applied independently of external geodata. For this reason, the methodical concept of using a SVR for the estimation of imperviousness was combined with an approach for the automated detection of settlements on the basis of SAR data, developed by ESCH et al. (2010). Furthermore, additional research was carried out to validate the efficacy of the combined ap-

proach in accurately quantifying changes in impervious surface cover. Within this context, the following questions were at the centre of this thesis:

- Does the automated detection of settlement areas on the basis of high-resolution SAR data provide a reliable basis for large area impervious surface mapping?
- What degree of precision can be obtained by applying the SVR approach to SPOT HRG data?
- Does the SVR approach provide an appropriate methodical basis for a continuous large-area monitoring of IS cover developments?

This study is linked to the Vietnamese-German multidisciplinary project WISDOM (www.wisdom.caf.dlr.de) which aims at the implementation of a water related Information System for the Mekong Delta (KUENZER et al. 2009), containing information from the fields of water quantity, water quality, land-cover and land-use, socio-economy, and others. The results derived from this study will be finally integrated into the Information System. In addition to the methodical objectives mentioned above, the study therefore also aims at the derivation of information products for the study area, Can Tho Province, located centrally in the Mekong Delta, listed as follows:

- Extraction of *information relating to settlement structures* in 2009
- Quantification of *absolute impervious surface cover* within the settlement areas for 2005 and 2009
- Quantification of *changes in impervious surface cover* between 2005 and 2009
- Computation of *averages related to impervious surface cover for administrative units*

Chapter 2

Theoretical Background

In this chapter, the theoretical foundations of remote sensing central to the understanding of the techniques and concepts applied in this study are elucidated. Firstly, the methodical principles of satellite remote sensing are elaborated, which are followed by a description of the characteristics of remotely sensed image data. Subsequently a detailed explanation of the functionality of Support Vector Machines (SVM) used for pixel based image classification and regression are presented followed by a short introduction into object based image analyses (OBIA) using the Software eCognition/Definiens. Finally, the basic methods for accuracy assessment applied in the field of remote sensing are discussed. These sections are based on the theoretical principles of MATHER (2004), RICHARDS and JIA (2006), JENSEN (1986, 2007) und CONGALTON and GREEN (2009) if no other sources are indicated.

A significant subject area of this work deals with the evaluation and analysis of radar images. Thus, the second part of this chapter focuses on the principles of radar based remote sensing thereby concentrating on the system- und target parameters of SAR radar systems most significant for settlement extraction. In this context, the basic principles of radar theory in this chapter are based on LILLESAND, KIEFER and CHIPMAN (2004) as well as on RYERSON et al. (1998) if no other sources are indicated.

2.1 Principles of Remote Sensing

The key characteristic of the science of remote sensing is the collection of information relating to an object or phenomenon (mostly located on the earth's surface), by the use of sensing devices that are not in direct physical contact with the target. This is achieved by

analysing and interpreting measurements of electromagnetic radiation (EMR), which is either emitted by the sun (passive systems) or by an artificial source carried on the remote platform (active systems). In the former case, the incident radiation of the sun is reflected, absorbed, transmitted, or emitted in an individual and characteristic manner dependent on the biophysical nature of the surface cover. The returning energy is received by the sensor in different wavelength bands forming so-called spectral signatures, which can be utilized to identify the reflecting surfaces (see FIG. 2-1). Optical remote sensing systems utilize energy from the visible to the near infrared range (about 0.3 and 1.4 μm) of the electromagnetic spectrum, whilst multispectral sensors are additionally sensitive to longer wavelengths including also the thermal bands (8 to 14 μm) of the spectrum.

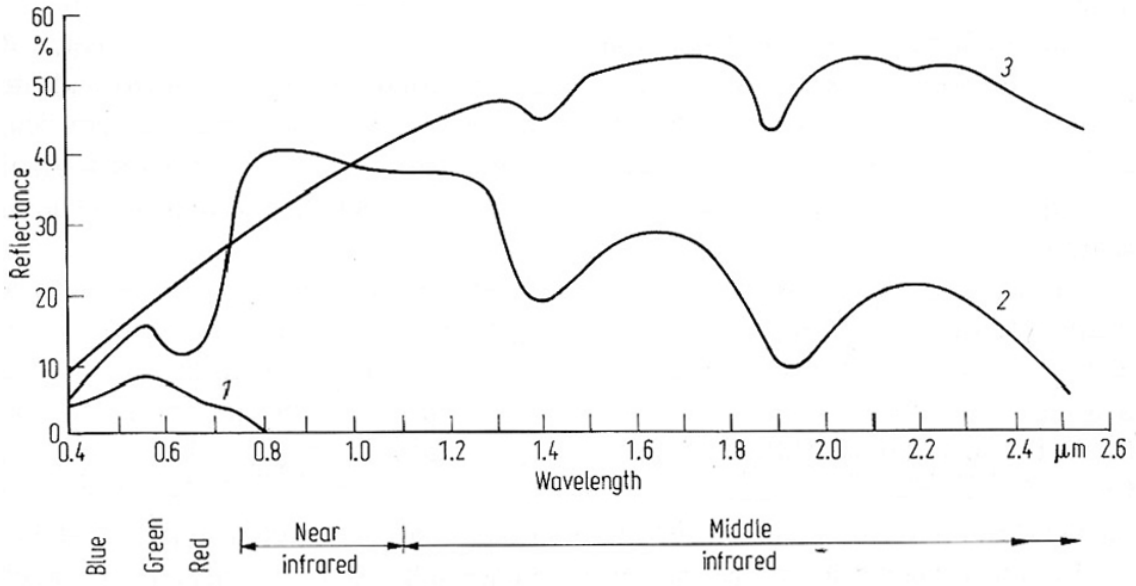

Fig. 2-1: Spectral reflectance characteristics or water (1), vegetation (2) and bare soil (3)
Source: RICHARDS & JIA (1999)

With this in mind, it becomes clear that remote sensing only provides information about the (bio)physical characteristics of the land surface (land-cover). Homogenous land cover types however can be further characterised by heterogeneous land-use. The latter reflects the social and economic purposes of land and their impact on the land surface processes (EOERTH 2010') which leads to a finer subdivision into classes relating to agriculture (even individual crop types), forestry, infrastructure, or further managed surfaces. Basically, land-use information cannot be observed directly from remotely sensed images, but can be derived indirectly by the integration of natural and social scientific assumptions (EOERTH 2010).

The limited ability to extract land-use information directly from satellite data has also implications for impervious surface calculation. The land-cover class bare soil for example, occurring in natural environments or used for agriculture generally features high infiltration rates and consequently, is characterised by very low levels of imperviousness. When soil characteristics are altered, for example when bare soil is used for transport, parking or storage, the same land-cover class is characterised by highly compacted material and encrusted surfaces and consequently, features high rates of imperviousness (see FIG. 2-2).

Fig. 2-2: Compacted Soil featuring high levels of imperviousness (Can Tho, January 2010)

2.2 Characteristics of digital image data

The reflectance measured by the sensor, covering a swath on the earth through an oscillating scanning mirror or a CCD array, is used to derive an image which is spatially composed of discrete picture elements, the so-called pixels. The brightness value of a pixel is proportional to the intensity of the received radiant flux and is categorised into discrete numerical levels, so-called digital numbers (DN). The number of these minimally distinguishable brightness levels is defined by the sensitivity of the sensor, known as its radiometric resolution.

The size of the area on the ground covered by a single pixel defines the spatial resolution of the sensor, which has significant effects on the level of spatial detail. The comparison of pixels from a pansharpened QuickBird scene having pixel sizes of 0.6m * 0.6m (FIG. 2-3a), with the pixels originating from the SPOT HGR sensor (FIG. 2-3b) featuring pixels with 10m*10m in size, demonstrates the effect of mixed pixels already mentioned in CHAPTER 1.2. The lower the spatial resolution, the more land cover classes are included within the extent of a single pixel. The characteristic spectra of each class thereby are merged together weighted by the fractions of the classes forming the aggregated spectrum of the pixel. The extraction of individual land-cover classes therefore becomes a difficult task, since in addition to the identification of the class of interest (e.g. impervious surface) also its relative proportion in the mixture has to be determined (RST 2010). Consequently, improvements

in spatial resolution increase the probability that phenomena with a limited extent are more accurately detected, which is for example necessary in urban remote sensing applications.

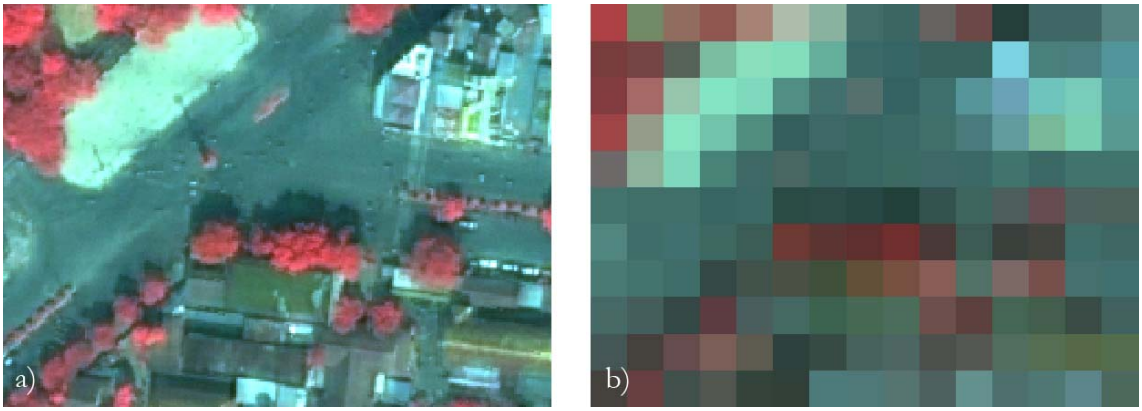

Fig. 2-3: Pixels of pansharpened QB image a); pixels of SPOT HRG image b)

The improvement in spatial resolution is accompanied by a decrease in areal coverage of a single scene. Generally, with broad areal coverage the revisit period of the satellite, known as the temporal resolution of a sensor, becomes shorter. Consequently, for applications where a frequent coverage is the key factor as is the case for many environmental monitoring applications, a sensor with a wide swath and broad coverage is often more appropriate. Furthermore higher resolution, leads to significantly higher data volume and thus requires increased computational as well as financial resources for the same areal coverage. Spatial resolution therefore significantly dictates the operational spectrum of a sensor.

The spectral resolution of the sensor is defined through its sensitivity to the number and dimension of specific wavelength intervals in the electromagnetic spectrum, which are also referred to as spectral bands. The higher the spectral resolution of a system is, the closer the spectral signature of an individual surface feature can be resembled. Certain bands are optimal for obtaining specific information of certain features – such as the red and near infrared bands to discriminate vegetation types and vigour. The Normalized Difference Vegetation Index (NDVI) for example, is computed from the red and NIR band according to equation (2.1), and is frequently used for the evaluation of photosynthetic vegetation (TUCKER 1979).

$$NDVI = \frac{NIR - red}{NIR + red} \tag{2.1}$$

2.3 Support Vector Machines

Support Vector Machines (SVM) originate from the field of machine learning methodology and were introduced to remote sensing by GUALTIERI and CROMP (1998) as a supervised image classification technique (RICHARDS and JIA 2006). In contrast to knowledge-based classification techniques, whereby the classification is implemented by logical rules, SVM are solely based on a training set to 'learn' the input-output relationship. Consequently, the user does not require any prior expert knowledge which has to be explicitly developed and defined in class descriptions. Compared to other unsupervised classification methods such as Maximum Likelihood Classifier which are based upon probability distribution models, SVMs are non-parametric classifiers which generate their output results via a geometric approach in a multidimensional vector space (RICHARDS and JIA 2006). A comprehensive description of the concept of SVM can be found in a number of publications, such as VAPNIK (1995, 1998), SCHÖLKOPF and SMOLA (2002, 2004), BURGES (1998) or CRISTIANINI and SHAWE-TAYLOR (2000) which also build the theoretical basis of this chapter. From a remote sensing perspective, SVM were applied in image classification by TZOTSOS and ARGIALAS (2008) or MELGANI and BRUZZONE (2004).

As a supervised classification approach, SVM learn from training examples and are able to generalise when applied to new data. The training data set S can be described according to equation (2.2):

$$S = \{(x_1, y_1), \ldots, (x_k, y_k)\} \subseteq (X \times Y)^n \tag{2.2}$$

Whereby each training example consists of two components, namely an input value x_i, which can be typically defined as a vector in an n-dimensional feature space X, and an associated output value or label y_i which can be either a categorical attribute (classification) or a real number (regression) of the nonempty set Y.

The geometric interpretation of the training procedure can be described by determining an appropriate set of parameters that places a decision surface, the so called hyperplane, between the different classes of training samples according to their position in an n dimensional feature space (see FIG. 2-4). The hyperplane can be written as

$$f(x) = \langle w, x \rangle + b \quad w \in R^N, b \in R \tag{2.3}$$

where $\langle \cdot, \cdot \rangle$ denotes the dot product, w the normal perpendicular to the hyperplane, and b the bias.

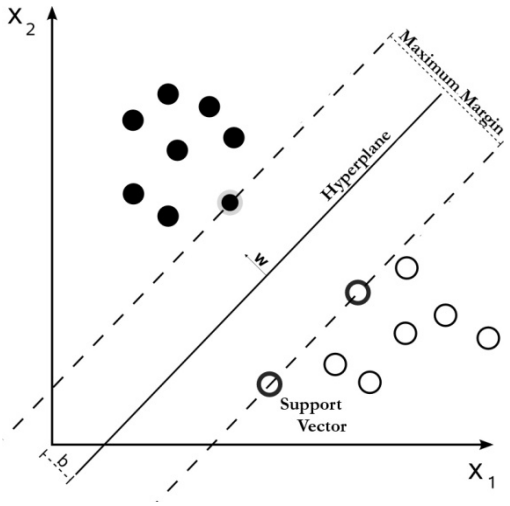

Fig. 2-4: Separating hyperplane for a binary classification

Among the set of functions (i.e. planes) which have the capacity of separating the data, the difficulty is to find the optimal one which provides the best generalisation performance related to unseen data. It is not sufficient to find a function which minimises the error amongst the training samples (=empirical risk minimisation), since this does not automatically imply a small error when applying the function to unseen examples (SCHÖLKOPF and SMOLA 2002). A hyperplane that perfectly fits the specific constellation of the training pattern also takes its particularities (i.e. random error or noise) into account. This case is known as overfitting and generally leads to very complex decision functions which provide only weak results when applied to new data. SVM address this problem by the means of an automatic optimization procedure which finds a compromise between the complexity of the hyperplane and its success at best fitting the training examples. This concept is known as structural risk minimisation (SRM) and has shown to be superior, to traditional empirical risk minimisation (GUNN 1998).

Based on the structural risk minimisation theory, the optimal hyperplane can be distinguished as that which maximizes the margin between the patterns of the different classes and the hyperplane (FIG. 2-4). Thereby the maximum margin can be defined by two additional, marginal hyperplanes that border the training points closest to the separating surface, the so-called support vectors (BURGES 1998). Consequently, only a small subset of the training set determines the position of the hyperplane whilst the remaining points have no influence on the hyperplane at all.

In most applications however, it is impossible to construct a linear separating hyperplane such as shown in Fig. 2-5a. This problem is addressed by mapping the training data $x_1, \ldots, x_n$ from its original space into a higher-dimensional feature space F. The transformation of the data is done via a so-called kernel function Φ.

$$x = (x_1, \ldots, x_n) \longrightarrow \Phi(x) = \big(\Phi_1(x), \ldots, \Phi_N(x)\big) \tag{2.4}$$

Within this higher-dimensional feature space F the set of input features become linear-separable, enabling a linear hyperplane to be constructed (FIG. 2-5b) that corresponds to a

nonlinear decision surface in the original feature space (FIG. 2-5c) (SCHÖLKOPF and SMOLA 2002). The four basic kernel functions are of linear, polynomial, radial or sigmoid nature. The choice of the appropriate kernel type and the optimisation of the Kernel parameters can pose a challenge and is a means by which the generalisation performance can be improved (Chih-Wei et al. 2008).

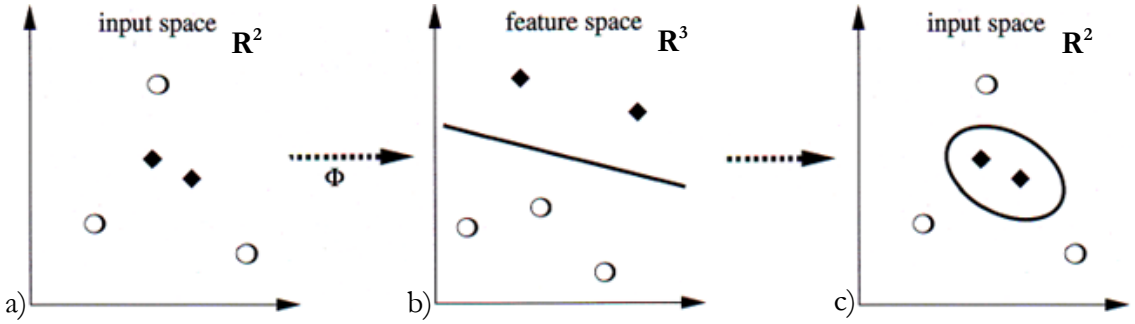

Fig. 2-5: Non-separable training data in the original input space a), linear separable training data in the higher dimensional feature space b), nonlinear decision surface in the original input space c)
(Source: modified according to SCHÖLKOPF and SMOLA 2002)

SV regression is a modified version of SV classification, which aims at finding a function that approximates all training pairs (x_i, y_i) with a deviation not exceeding a certain threshold ε (FIG. 2-6a) (SCHÖLKOPF and SMOLA 2004). In order to assure the feasibility of this restricted form of regression (especially at small ε) and to allow a degree of generalisation, the margin of tolerance ($\pm\varepsilon$) is extended by a loss-function, The latter enables the exception of outliers by using a set of so-called slack variables ξ which measure the deviation of the training samples from the hyperplane (TZOTSOS 2006). FIG. 2-6b illustrates the so-called e-insensitive loss function as a cross-section of the regression function. As far as the precision ε, the cost function is 0 and the training samples remain unaffected. However, training samples located outside of the margin, are penalized in a linear fashion according to the degree of deviation from ε.

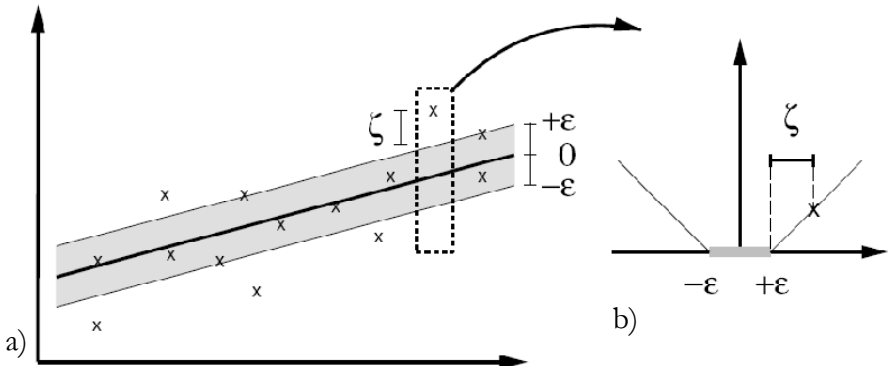

Fig. 2-6: The soft margin loss setting for a linear SVM
(Source: SCHÖLKOPF and SMOLA 2004)

2.4 Object bases image analyses

The traditional classification approaches of digital satellite data are based on the pixels as the smallest units of an image. These methods allocate a pixel into classes according to its spectral properties regardless of its context (BAATZ and SCHÄPE 2000). When pixels are significantly smaller than the objects of interest, working with groups of pixels representing so called patches on the ground can reveal a surplus of important spectral and spatial information in order to analyse the image. In this respect, a patch refers to a spatial unit which differs from its surroundings in nature or appearance and forms a basic structural and functional unit of the landscape (BLASCHKE and STROBL 2001).

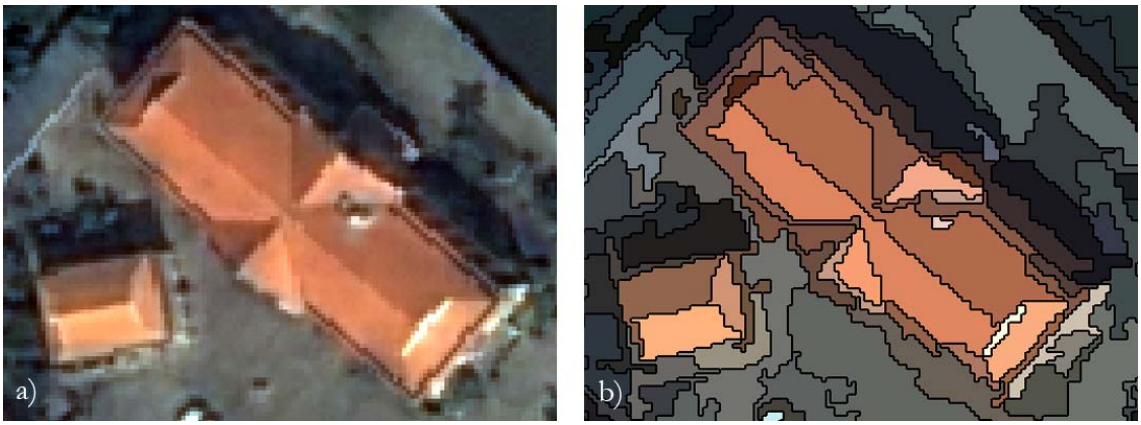

Abb. 2-4: pixel based a) and object based b) representation of image data

On the one hand, using the spectral properties of all pixels within an object, additional spectral information such as average reflectance can be derived to address high intra-class spectral variability. On the other hand, since image analysis implies dealing with image semantics (BAATZ and SCHÄPE 2000), additional spatial information such as the shape and size of objects, as well as their context and relationships to other objects can be taken into account (BLASCHKE 2010).

The most common way of grouping pixels into meaningful image objects is by image segmentation (Baatz and Schäpe 2000). In this work, the multi resolution segmentation implemented within the object-oriented software *eCognition,* was applied. The segmentation is based on a bottom-up region merging technique that merges pairs of image objects (beginning with the single pixels), in iterative cycles to larger objects. For each possible merger, a homogeneity criterion describing the similarity of adjacent image objects is compared with a user-determined threshold. This threshold, called scale parameter, defines the maximal permitted degree of heterogeneity and indirectly controls object size, as a low value only permits fewer merges resulting in smaller image objects. The homogeneity is assessed ac-

cording to parameters of colour and shape, which can be individually weighted by the user. The colour criterion is defined by the sum of standard deviations in the bands,

$$h_{colour} = \sum_c w_c \cdot \sigma_c \qquad (2.5)$$

h = heterogeneity colour
w_c = weight per band
σ_c = standard deviation

while the form criterion is defined by smoothness and compactness of the objects:

$$h_{compact} = \frac{l}{\sqrt{n}} \qquad h_{smooth} = \frac{l}{b} \qquad (2.6)$$

h = heterogeneity compactness
l = length of the object's outline
n = number of pixels of the object

h = heterogeneity smoothness
l = length of the object's outline
b = shortest length of the bounding box

Segmentation levels of different scales can be arranged in a hierarchical network of image objects, with each segment being connected to its vertical and horizontal neighbours. In this way, not only spatial topology but also hierarchical relationships can be taken into account.

eCognition also provides properties for a knowledge-based classification of the objects generated. As a first step, a classification scheme is created - the so-called class hierarchy, whereby each class is defined by a specific class description. The latter is composed of membership rules, which in turn are defined by a set of spectral, shape, textural, or hierarchical characteristics of the derived objects. The individual characteristics can be combined by the logical operations *And* or *Or,* shown in FIG. 2-7a. Furthermore, it is possible instead of applying crisp membership rules (yes/no), to define a continuous range of (fuzzy) membership ranging between 0% and 100% as shown in FIG. 2-7b.

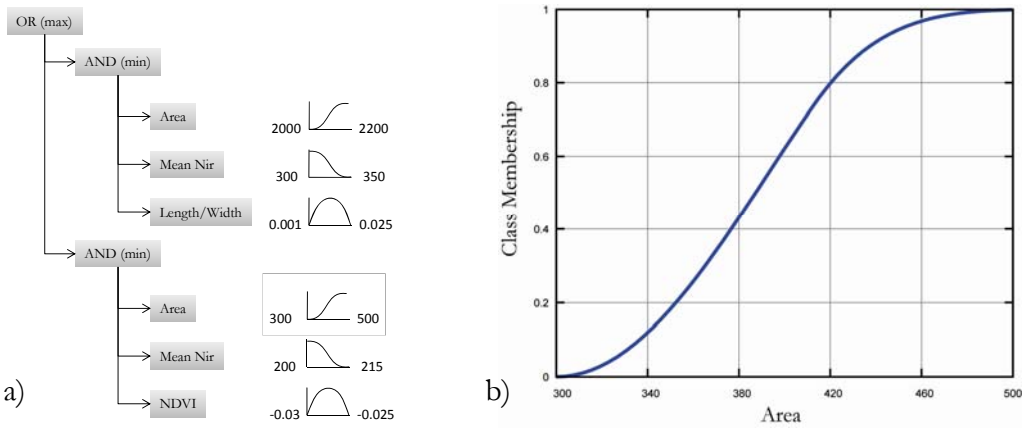

Fig. 2-7: Class description using logical operators a) and fuzzy membership rules b)

During the classification process, each object is evaluated on the basis of the class descriptions, resulting in the output of the specific degree of membership to each class. The maximum membership degree determines the final classification of the object (DEFINIENS 2007).

2.5 Validation principles

Remotely sensed information is only useful when some measure of its quality is known. The most widely accepted method to determine the classification accuracy is the comparison of a sample of locations from the classified or modelled results with the actual conditions prevailing at the same locations on the ground, constituting the so-called ground truth data. As the name suggests, this information is assumed to represent true values and may be derived from in-situ investigation, geographic information data, or from the interpretation of remotely sensed data obtained at a higher resolution. From these checks, the number of samples labelled correctly together with the number of samples labelled erroneously for each class can be expressed in tabular form according to TABLE 2-1. From this so-called error or confusion matrix, a range of descriptive and analytical statistical accuracy measures such as the overall accuracy, producer's accuracy, user's accuracy, or the kappa coefficient can be calculated.

Table 2-1: Illustration of an error matrix with

		GROUND TRUTH CLASSES			TOTAL CLASSIFIED
		A	**B**	**C**	
PREDICTED CLASSES	**A**	n_{AA}	n_{AB}	n_{AC}	n_{A+}
	B	n_{BA}	n_{BB}	n_{BC}	n_{B+}
	C	n_{CA}	n_{CB}	n_{CC}	n_{C+}
TOTAL GROUND TRUTH		n_{+A}	n_{+B}	n_{+C}	n

Source: modified according to FOODY (2002)

Overall Accuracy indicates the percentage of correctly classified sample points and can be computed by dividing the total correct number by the total number of pixels in the error matrix (2.7) (Foody 2002). This non-site specific measure however does not reveal any information about the nature of the errors.

$$\text{Overall Accuracy} = \frac{\sum_{k=1}^{q} n_{kk}}{n} * 100 \qquad (2.7)$$

In general, the producer is mostly interested in the probability with which a certain land use category on the ground is correctly classified in the map. This measure is called producer's accuracy and can be derived by dividing the total number of correctly classified pixels in a category, by the total number of pixels of that category as derived from the reference data (2.8) Consequently, all pixels belonging to the category of interest that the classifier has failed to recognise contribute to the error of omission (Congalton 1991, Jensen 1986).

$$\text{Producer's Accuracy} = \frac{n_{ii}}{n_{+i}} \tag{2.8}$$

On the other hand, the so called user's accuracy is a measure of classification reliability, indicating the probability with which a pixel designated to specific class of interest, truly represents that class on the ground. This measure is derived by dividing the total number of correct pixels in a category by the total number of pixels that were classified in that category (2.9) (Jensen 1986, Congalton 1991). Pixels that were wrongly classified in this context contribute to the error of commission

$$\text{User's Accuracy} = \frac{n_{ii}}{n_{i+}} \tag{2.9}$$

A further measure for classification accuracy is the kappa coefficient (K). It is used to indicate the level of classification accuracy compared to a classification obtained by chance. K can be calculated from the difference between the specific coincidence of the classified and reference pixels and a random coincidence of reference pixels and a random classification according to equation (2.10), whereby q denotes the number of classes in the classification results (Foody 2002).

$$\text{Kappa coefficient} = \frac{n\sum_{k=1}^{q} n_{kk} - \sum_{k=1}^{q} n_{k+}n_{+k}}{n^2 - \sum_{k=1}^{q} n_{k+}n_{+k}} \tag{2.10}$$

2.6 Radar fundamentals

In contrast to optical remote sensing platforms, radar systems supply their own source of illumination (active systems). The energy used is based on microwave radiation with frequencies between 0.2 and 40 Gigahertz, which correspond to wavelengths within the approximate range of 1 m to 1 mm. TABLE 2-2 lists the common wavelength bands applied in pulse transmission.

Table 2-2: Frequency and wavelength of radar bands

BAND	FREQUENCY [GHZ]	WAVELENGTH [CM]
P-band	0.22 - 0.39	77 - 136
L-band	1.0 - 2.0	15 - 30
S-band	2.0 - 4.0	7.5 - 15
C-band	4.0 - 8.0	3.75 - 7.5
X-band	8.0 - 12.0	2.4 - 3.75
K_u-band	12.5 - 18.0	1.67 - 2.4
K_a-band	26.5 - 40.0	0.75 - 1.18

The application of microwave radiation for earth observation has a significant advantage over optical sensors, due to the fact that this portion of the electromagnetic spectrum is scarcely affected by the atmosphere. Consequently, microwave radiation is capable of penetrating the atmosphere under almost all weather conditions. As radar systems are active systems, they can also be used independent of natural light.

FIG. 2-8 illustrates the geometric concept and nomenclature of spaceborne radar data collection. Side-looking radar systems generate continuous strips of image data that parallel the satellites flight track. This happens by the transmission of short pulses of microwave energy moving radially outward from the satellite's antenna in a perpendicular direction to the flight track (i.e. range direction). As the satellite advances, the antenna as well as the illuminated area on the ground (i.e. the antenna footprint) are continuously repositioned along the flight direction resulting in continuous swaths of ground coverage. The transmitted radar pulse is reflected from the features on the ground so that a portion of the backscattered energy can be received from the antenna. By measuring the return time of these backscattered signal echoes, the slant range which is the direct distance between the antenna and the reflecting objects can be determined.

In contrast to optical systems, the spatial resolution of SAR sensors is defined in two distinct directions - perpendicular to the flight track called range direction, and parallel to the flight track called azimuth direction. In range direction, two ground features can be imaged

separately, if their reflected signals do not timely overlap so that the antenna can receive them separately. Therefore, the slant range distance between two features has to constitute more than half of the pulse length, the length of time that the antenna emits its burst of energy.

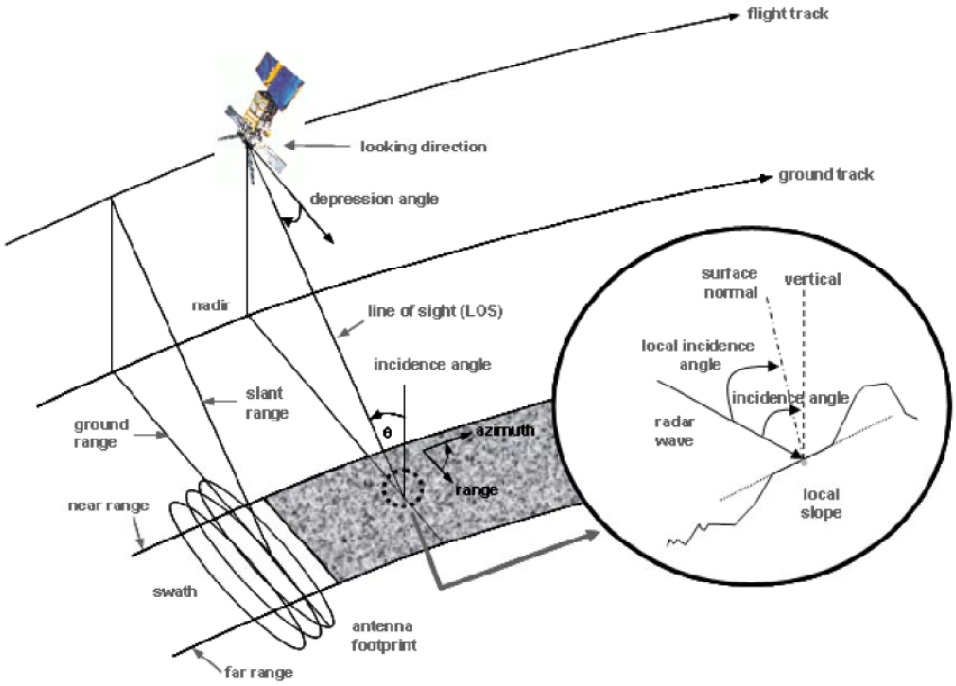

Fig. 2-8: Nomenclature used for radar data collection

Source: Esch (2006)

The spatial resolution in azimuth direction is a direct function of the wavelength and the ground range distance and inversely proportional to the antenna length. Consequently, if high resolution at long range is the objective, very high frequencies or enormous lengths of the antenna were necessary, which however can only be adjusted to a certain limit. Consequently, the usage of Real Aperture Radar (RAR) systems generally is limited to low altitudes and the operation of short wavelengths, which however restricts the area of coverage and increases the susceptibility to atmospheric distortions.

Therefore, synthetic aperture radar (SAR) systems utilize the sensor motion along track to synthesize the effect of a very long antenna. Thereby, ground targets are recorded from different viewing angles during the over flight with the returning energy pulses being processed according to the principle of Doppler frequency shifts. The result of this mode of operation gives rise to very narrow beam widths thereby facilitating high spatial resolution without limitations to antenna lengths or operating wavelengths.

2.6.1 System Parameters

The primary radar system parameters affecting the intensity of radar returns are the used wavelength, polarisation and the incident angle for radar pulse transmission.

Wavelength

The wavelength of radar energy significantly affects the interaction between radar signal and illuminated objects on the ground. Beside the fact that azimuth resolution is higher for shorter wavelengths, there are two main parameters, which are directly dependent on radar wavelength: depth of penetration and surface roughness. The longer the wavelength of microwave radiation is, the deeper the ability to penetrate into a medium. With respect to the ability of settlement detection, long wavelengths such as L-band radiation may reveal surface features such as buildings or streets hidden under the vegetation canopy, while shorter X-band radiation cannot. In addition, radar pulses of different wavelengths affect the scatter properties of a surface feature and thus produce variable returns. According to the Rayleigh criterion, surface roughness is defined relative to the wavelength of the radar signal. A surface which appears smooth at one wavelength resulting in a darker image tone may appear quite rough at another wavelength, resulting in a brighter image tone (see also CHAPTER 2.6.2 below).

Polarisation

Radar signals can be filtered in a way that the electromagnetic waves are restricted to either a horizontal (H) or a vertical (V) plane perpendicular to the direction of wave propagation. This filtering is referred to as polarisation, which can be categorised into four different combinations of signal transmission and reception. Like-polarised imagery results from either horizontal or vertical send and receive combinations (HH or VV), whilst cross-polarised imagery is obtained from mixed horizontal and vertical send and receive combinations (HV of VH). Whether like-polarised or cross-polarised images have higher information content for settlement extraction is not conclusively reported by previous studies. The study of HENDERSON and MOGILSKI (1987) for example which dealt with the effect of polarisation on urban land use mapping, indicated that no single polarisation was preferable for all land use categories.

Incident angle

A further parameter affecting radar returns is the incident angle, defined as the angle between the incident radar beam at the ground and a vertical plane at the point of incidence (FIG. 2-8). The incident angle increases from the near range to the far range resulting in

altered surface roughness properties in a way that rough surface features become smoother and thus appear darker towards the far range (see CHAPTER 2.6.2 below). Furthermore, higher incident angles give longer radar shadows, which can especially obscure settlements located at backslopes (see CHAPTER 2.6.2 below).

2.6.2 Target Parameters

Properties of surface or target features influencing the intensity of radar returns are dielectric properties, surface roughness and feature orientation.

Dielectric Properties

The complex dielectric constant indicates the conductivity of a surface feature, which significantly depends on its proportions of water, salt or metal. The dielectric constant strongly influences the absorption and propagation of electromagnetic waves and directly affects the intensity of radar returns. In urban environments, objects with high dielectric constants comprise metal bridges, metal rooftops, silos, railroad tracks or poles, which appear as bright features in the image. In natural settings, water has a very high dielectric constant making moisture in soil or vegetation a factor of uncertainty for settlement detection, as they can produce bright returns similar to such settlement features mentioned above.

Surface Roughness

Surface roughness characterises the amount of height variations on the ground, however is also dependent on the wavelength and the incident angle, as mentioned in CHAPTER 2.6.1. Roughness of the terrain can be categorised according to three different scales, however no clear-cut dividing line exists. Microscale roughness refers to height variations of some fractions of the wavelength and strongly determines image tone, i.e. the mean brightness, of a resolution cell. In this context, smooth surfaces lead to specular reflection (FIG. 2-9b), which redirects the radiation away from the source and thus results in dark image tones. Rough surfaces in contrast, are diffuse reflectors (Fig. 2-9a) and scatter incident energy in all directions. Thereby, a significant portion of the incident energy returns to the antenna resulting in relative bright image tones. Mesoscale roughness characterises height variations comparable to the spatial resolution of the radar system. At this scale, roughness characteristics directly influence image texture, which becomes coarser with increasing variability in the surface structure. Macroscale roughness is predominantly controlled by regional topography and the natural relief, resulting in texture patterns many times larger than the resolution cell of the radar system.

Particularly bright responses can be observed from corner reflectors, as shown in FIG. 2-10. Corner reflectors arise when two or three planar and smooth surfaces are oriented at a right angle. This kind of corner arrangement can cause double or multi reflections of the radar pulse when the open angle faces the radar sensor as illustrated in FIG. 2-9c. As corner reflectors such as house walls or lamp posts generally constitute spatially restricted areas, they also are known as point targets and typically appear as extremely bright spots in the radar image (see FIG. 2-10). Because straight lines and sharp angles are more commonly characteristic of human-altered landscapes, dihedral or trihedral corner reflectors occur predominantly in urban environments.

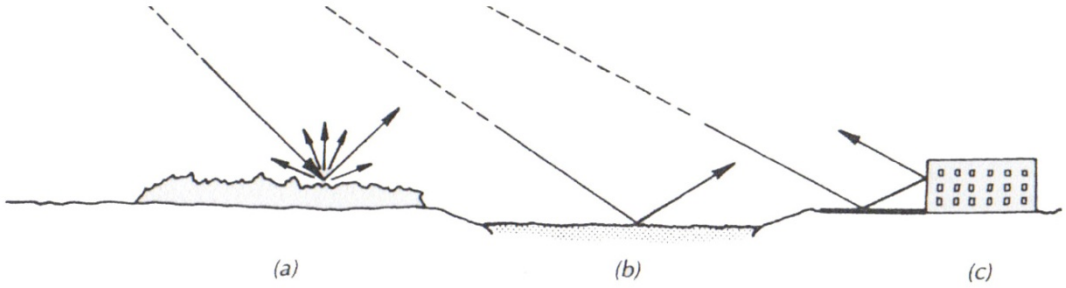

Fig. 2-9: Radar reflection from various surfaces: (a) diffuse reflector; (b) specular reflector; (c) corner reflector
Source: modified according to (LILLESAND et al. 2004)

Radar Imaging Geometry

Because of the special geometric characteristics of side-looking image acquisition, the geometry of radar imagery is fundamentally different to that of optical imagery. The most important geometric effects which influence the detection and analysis of settlements are the foreshortening, layover, and shadow effect.

As distance is measured as a function of time, terrain slopes facing the antenna are not presented true to size in the image, which can be explained by the reduction in slant range distance with increasing vertical position of a feature. This phenomenon, referred to as radar foreshortening, causes the size of the sloped surface to become compressed on the image, which becomes more pronounced the closer the slope approaches perpendicularity to the look direction. For vertical features such as buildings, trees, or bridges the top is even closer to the radar antenna than the base and therefore is recorded sooner. As this causes a feature to be projected in the image as bent over the closer features in ground range, the effect is referred to as radar layover. The greater these geometric distortions are the more energy per unit area is presented in the affected area on the image. Consequently, foreshortening and layover zones appear in brighter image tones, as can be seen from Fig.

2-10. These distortions in relief displacement are most severe at near range and small incident angles. A further effect of the side-lighted character of radar systems results in areas being blocked from illumination by the radar beam, which occurs on areas to the rear of vertical features facing the antenna. These sharply defined shadow areas are completely black and in contrast to their counterparts in optical satellite images contain no information at all.

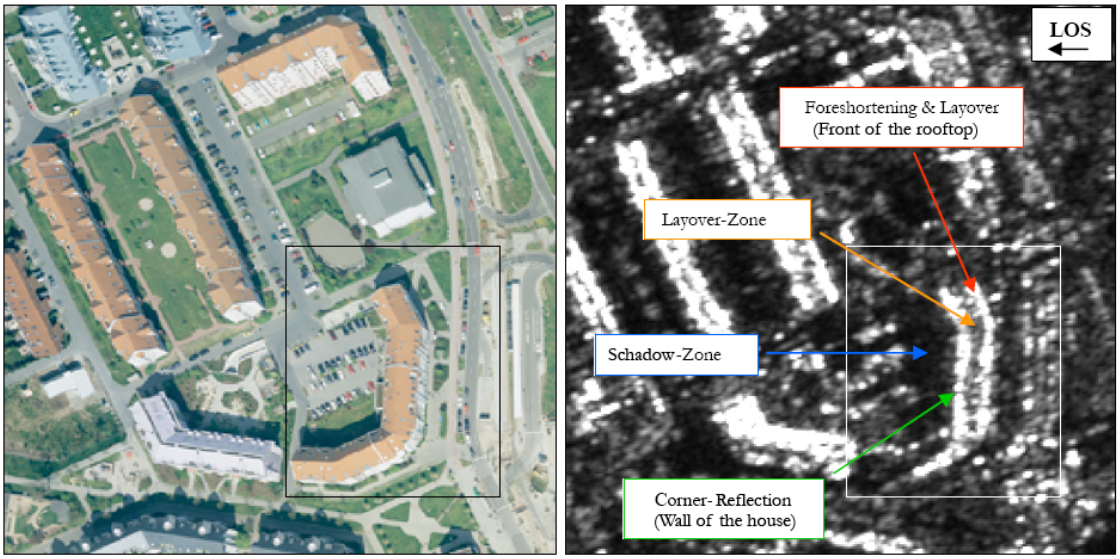

Fig. 2-10: Distortions and shadow effects in urban environments due to image geometry and feature orientation
Source: modified according to ESCH (2006)

2.6.3 Speckle

Speckle is a system-inherent noise phenomenon, which is always present in images recorded by SAR sensors (Esch et al. 2010). It is caused by the interference pattern of the returning microwave signal, which in fact consists of contributions from many independent scattering centres within one resolution cell (Goodman 1976, Ulaby et al. 1986). Depending on their phase, the individual return signals interfere with one another either constructively or destructively, resulting in a seemingly random pattern of brighter and darker pixels (GOODMAN 1976). As this grainy appearance is always present in addition to real textural information, two different types of areas can be dis-

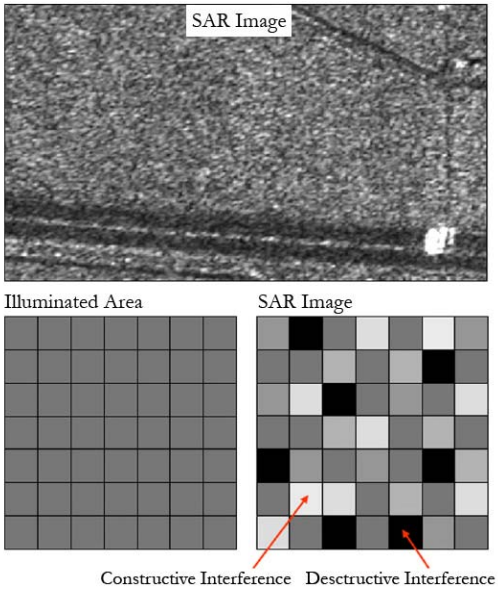

Fig. 2-11: Speckle in radar images

tinguished in radar images. In homogenous areas, the only image texture that may be observed is associated with speckling (Frulla et al. 2000). Heterogonous regions in contrast, feature true radiometric and textural information resulting from the backscatter properties of the individual objects on the ground, which however is superimposed by speckling (ULABY ET AL. 1986, FRULLA ET AL. 2000).

Speckle can be reduced be either applying filters (e.g. Lee, Frost) or by multiple-look processing, where several independent images of the same area are used for averaging neighbouring pixel values thereby producing a smoother image. These images, also known as looks, are produced by using different portions of the satellites synthetic aperture, which however has negative effects on spatial resolution (FRULLA et al. 2000). In light of this, beside the number of looks also the resolution of a system affects the quality of a radar image.

Chapter 3

Study Area

The study site comprises an area of approximately 1400 square kilometres covering the administrative area of Can Tho Province in the centre of the Mekong Delta (see FIG. 3-1). In this region of south-western Vietnam, the Mekong River branches into several tributaries approaching and emptying into the South China Sea. Highly populated stream environments, like the Mekong Delta, are some of the most fragile and threatened environments in the world, due to the strong interaction between the aquatic and terrestrial environmental systems, which each can be affected by human disturbances (GILLIES et al. 2003). In addition, being a low-lying coastal region the Delta and its population is especially vulnerable to a rise in sea level induced by climate change.

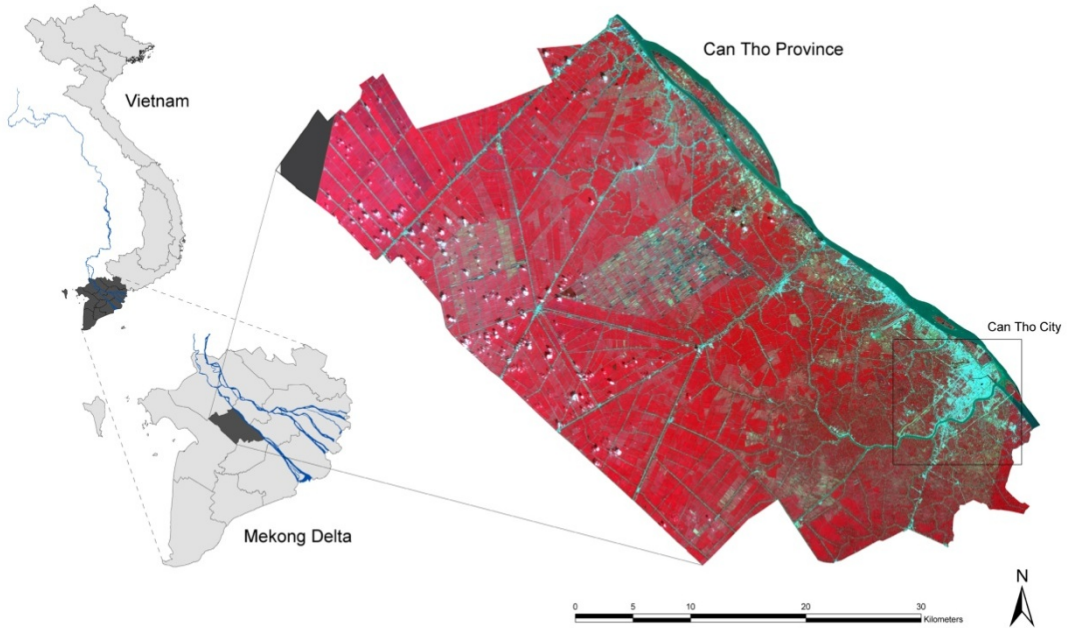

Fig. 3-1: Overview of the study area

Can Tho Province is like the whole Delta a largely rural area, dominated by agricultural land (FIG. 3-2a). This is mostly irrigated crop land for rice paddy cultivation, with seasonally flooded wetlands and numerous aquaculture ponds for shrimp farming. In addition, the landscape is interspersed by a dense and complex hydrologic network of man-made canals, dykes and sluices built for transportation and to provide flood protection, prevent salinity intrusion and to control irrigation (EVERS and BENEDIKTER 2009). As Vietnam's "rice basket" (MATHER 2009) the Mekong Delta accounts, together with the Red River Delta, for almost 70 percent of the irrigation sector making it the greatest rice producing area in the country and Vietnam the second largest rice exporter in the world (EVERS and BENEDIKTER 2009).

Although the Delta is primarily rural, it is with 17.7 million people and 430 people per square kilometre also one of the most densely populated and dynamic regions in Vietnam. Can Tho Province features a population density of ~860 persons per square kilometre and therefore, lies even more than three times above the national average of 260 persons per square kilometre (GSOV 2010). The south-eastern part of the province, where the corresponding provincial capital Can Tho City is located, is characterised by high density urban development. From this area, settlement activities have extended along the Mekong and spread to its main branches and channels, functioning as important transportation infrastructures. As the largest city in the region, Can Tho is also the political, economic, cultural and transportation focal point of the Delta. Therefore, it has continuously attracted rural migrants and stimulated significant growth in the surrounding region. Between 1995 and 2008, the urban population of Can Tho Province grew from 344,000 inhabitants to more than double, reaching 744,000 people (GSOV 2010). This corresponds to an annual growth rate of over 6% whereby the national average is "only" approximately 3.8% (FIG. 3-2b).

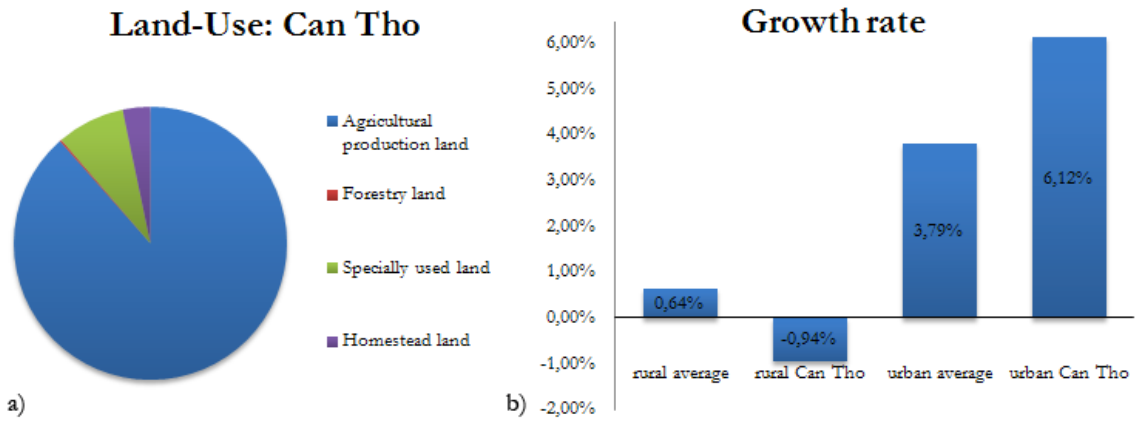

Fig. 3-2: Land-use in Can Tho Province a); National population growth rate compared to Can Tho Province b)
Source: General Statistics Office Vietnam (GSOV 2010)

The population development in rural areas of the province however indicates a negative growth trend. One can conclude from this that, although within the province twice the number of people is still living in rural areas, the population pressure emanating from the cities will eventually exert considerable strain on open spaces and agricultural land, surrounding the major agglomerations. The increase in land consumption for residential, commercial and industrial purposes has increased particularly since the introduction of the Doi Moi reforms (Renovation) in 1986 which saw the shift from a centrally planned to a market-driven society. With the diversification of capital investment, the creation of a property market and the commercialization of the housing sector, it is apparent how such forces have started to overshadow the influence of central planning as a city-shaping force, resulting in many distinct manifestations in the underlying urban landscape (QUANG and DETLEF KAMMEIER 2002). The commercial and tourist-related redevelopment of Can Tho City has led to an intensification of urban structures in the central areas and along Hậu Giang River. Simultaneously, the development of new residential buildings and industrial complexes in the North, South, and West of the urban fringe areas has facilitated the loss of considerable stretches of former agricultural ground. Furthermore, the expansion of the road network system has facilitated further site development and additional growth. With the completion of a new highway which by-passes Can Tho City in the South and the strategically important Can Tho Bridge over the Mekong, it can be assumed that the current population dynamics and construction development will continue to evolve.

Due to the special hydrological character of the area, the ecological system is particularly vulnerable to the impacts of these developments. The concentration of settlement activities in the direct vicinity of canals and waterways results in high proportions of imperviousness directly located at the stream network. This intensifies the discharge of polluted runoff, as almost 100% of it will reach the surface-water body whereby nonpoint source pollutants are not filtered by riparian buffer zones (BRABEC et al. 2002). Furthermore, with approximately 1900 mm precipitation per year of which 95% occur between May and November, the pluviometry is high and concentrated within a few months of the rainy season (BOLAY et al. 1997). This results in intensive peak discharges which particularly threaten water quality and pose a higher potential for torrential flooding. In light of this, Can Tho Province and Can Tho City in particular are especially sensitive to the environmental effects accompanying increasing proportions of impervious surface cover, as elucidated in CHAPTER 1.1.

Chapter 4

Materials and Preprocessing

In the first part of this chapter, an overview is presented of the various types of image data used in this work and the corresponding sensor systems which recorded these data. Following this, the main preparation and correction steps taken prior to the utilization of the images, are elucidated in detail.

4.1 Materials

TerraSAR-X (TSX) is a side-looking X-band Synthetic Aperture Radar (SAR) satellite which was launched on June 15, 2007. The satellite was developed and is now operated by the German Aerospace Centre DLR and EADS Astrium GmbH, as a joint venture. The active antenna allows four different recording modes (Stripmap, High Resolution Spotlite, Spotlite, ScanSAR) to support a variety of applications ranging from medium resolution, polarimetric imaging to high resolution mapping (FRITZ and EINEDER 2009). The basic imaging mode is the Stripmap mode featuring a constant azimuth resolution of 3.3 m and a swath width of 30 km. In this study, only images recorded in the Stripmap mode were used. The characteristic parameters of this mode are listed with the properties of the platform in TABLE 4-1.

SPOT 5 (SPOT) is the fifth SPOT (Système pour d'Observation de la Terre) satellite launched on May 4, 2002 by the French Centre National d'Études Spatiales (CNES). The satellite carries two imaging devices named "Haute Resolution Geometrique" HRG with visible and near-infrared bands at 10m, a shortwave infrared (SWIR) band at 20m and a panchromatic band at 2.5m (JENSEN 2007). Characteristics of the HRG sensor are summa-

rised in TABLE 4-1. In addition, the HRG incorporates a controllable mirror which allows images to be obtained on both sides of the satellite track resulting in angles of incidence in a range of ± 31.05° (BLAIS and HERMIER 1995, SPOT 2010). The HRG sensor features swath widths of 60 x 60 km or 60 km x 120 km in twin-instrument mode and thus, is especially appropriate for medium-scale applications (at 1:25 000 and 1:10 000 locally) (SATIMAGINGCORP 2010).

QuickBird (QB) is a high resolution, commercial satellite launched on October 18, 2001 which is owned and operated by *DigitalGlobe*. The satellite with its BGIS 2000 (Ball's Global Imaging System) sensor collects panchromatic imagery at 0.6 m resolution and multispectral imagery at 2.4 m resolution (TABLE 4-1). Similar to the HRG sensor, the QB camera allows across-track and additional in-track pointing. Due to the high spatial resolution, only swath widths of 16.5 km can be recorded making the satellite an appropriate source for analyses at local scales (SATIMAGINGCORP 2010).

Table 4-1: Technical parameters and properties of the sensors used in this work

	SPOT-5 (HRG)	QUICKBIRD	TERRASAR-X (STRIPMAP)	
Band wavelength (nm)	480 - 710 (pan)	450 - 900 (pan)	**Band wavelength (cm)**	3,1 (X)
	500 - 590 (green)	450 - 520 (blue)	**Radar frequency**	9.65 GHz
	610 - 680 (red)	520 - 600 (green)	**Antenna size**	
	790 - 890 (near IR)	630 - 690 (red)	**Incidence angle range**	20-45°
	1580 - 1750 (mid IR)	760 - 900 (near IR)	**Polarization**	HH or VV
Spatial resolution (m)	2.5 x 2.5 (pan)	0.6 x 0.6 (pan)	**Range resolution (m)**	3,3
	10 x 10 (multi)	2.4 x 2.4 (multi)	**Azimuth resolution (m)**	1,75-3,49
Swath width (km)	60	16,5	**Swath width (km)**	30*50km
Revisit time (days)	26	40362	**Revisit time (days)**	11 days

All in all, two TSX, two QB and four SPOT images were used in this study. All scenes were stored in the GeoTIFF format and featured a UTM map projection (Zone 48N) with a WGS-84 datum. When categorizing the different datasets according to their methodical usage, three main categories could be identified, namely settlement delineation, model training and finally, model application and change detection (see FIG. 4-1 and TABLE 4-2).

The delineation of the settlements is solely based on single-polarised (HH) TSX scenes. For this, two datasets recorded on 2009-01-13 and 2009-24-01 were available which together covered almost the whole area of Can Tho Province (FIG. 4-1a). The datasets were acquired in Stripmap mode (SM) and were processed as a multi-look ground range detected (MGD) product, so that the scenes existed as spatial enhanced intensity images with a reso-

lution of 2.75 m. In addition, subsets of two QB scenes recorded on 2007-01-27 and 2006-12-22 were used for validation purposes.

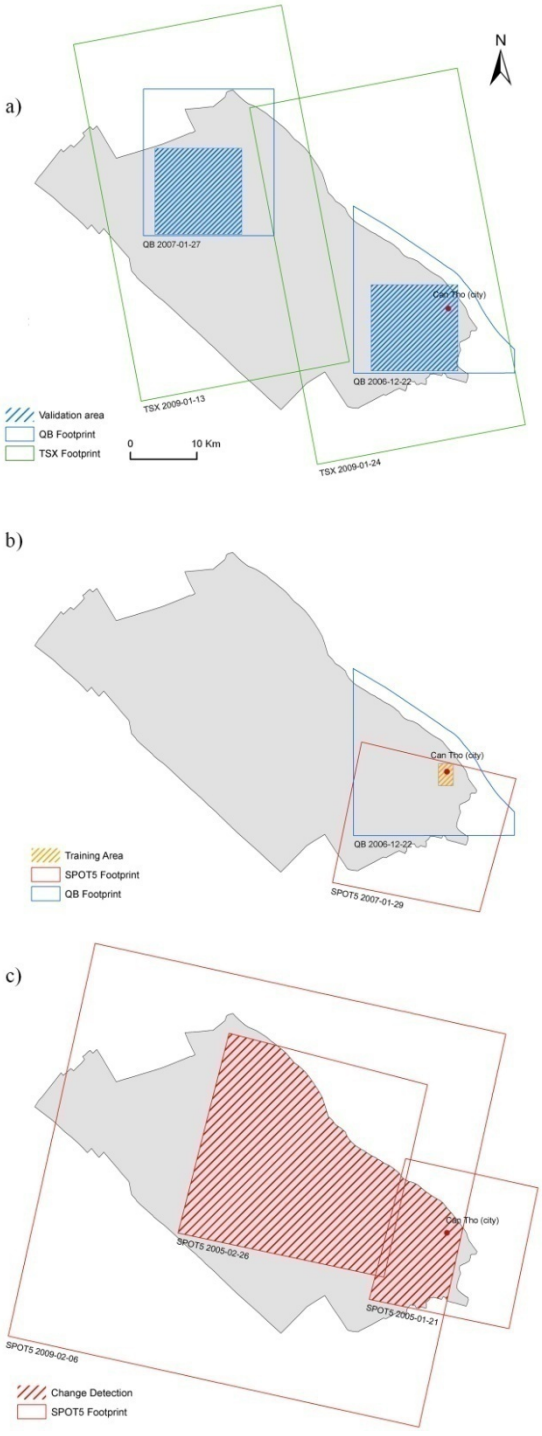

Fig. 4-1: Overview of image data used in this work

The training procedure of the SVR models was based on a pair of multi-resolution, optical datasets: firstly, a high resolution image and secondly, an image of comparable lower resolution, both of which had to cover the same training area (FIG. 4-1b). In addition, in order to minimize external distortions recording dates had to ensue within a tight time frame. For the high resolution image a QB scene was used, recorded on 2006-12-22. The second image had to originate from the same sensor as the images that were subsequently used for the model application. In this case a SPOT 5 scene was chosen which was recorded on 2007-01-29. For simplicity, SPOT scene and QB scene are hereafter called training image data in the course of this study.

For model application and the subsequent change detection analysis (FIG. 4-1c), the recording time of the images was again the determining acquisition factor. In order to detect noticeable changes in construction activities, it is crucial that a sufficient time period lies between the two recording dates used for change detection. In addition, only images recorded within the months of December and February were appropriate, for which there were two reasons. Firstly, seasonal flooding and high cloud predictability prevailing within the remaining months obscure important information about the actual land-cover. Secondly, for the change detection analysis it was crucial to minimize pixel brightness variations between the datasets arising from plant phenology or from seasonal

variability in the atmosphere and sun conditions. Consequently, for model application three SPOT 5 scenes were available: two quarter scenes recorded on 2005-01-21 and 2005-02-26 formed the basis for an impervious surface map for 2005, and a further full scene recorded on 2009-02-06 provided the basis for an impervious map for 2009. With an interval of four years and a seasonal coincidence with variations in time of less than three weeks, the data basis was appropriate for change detection analysis. For simplicity, these images are hereafter called application data in the course of this work.

Due to the above mentioned criteria, data acquisition proved to be challenging since a further criterion, namely a minimum of cloud cover, was essential for all images.

Table 4-2: Used image data according to main application

APPLICATION	SENSOR	DATE	DATA BASIS FOR
Settlement Delineation	TSX	2009-01-13	Settlement Extraction
	TSX	2009-01-24	Settlement Extraction
	QB	2006-12-22	Urban subset for Validation
	QB	2007-01-27	Rural subset for Validation
Model Building	QB	2006-12-22	IS values for training data (labels)
	SPOT	2007-01-29	Reflectance for training data
Model Application	SPOT	2005-01-21	Impervious Surface estimation 2005
	SPOT	2005-02-26	Impervious Surface estimation 2005
	SPOT	2009-02-06	Impervious Surface estimation 2009

4.2 Preprocessing

Remote sensing images are always accompanied by errors in geometry and pixel brightness, referred to as radiometric errors. When images are to be utilized, it is frequently necessary to correct these errors if the accuracy of the results is not to be prejudiced (RICHARDS and JIA 2006). This especially applies to analyses when images from different recording times (multitemporal) or from different sensors (multi-sensoral) are to be compared, as the absolute pixel positions of the different scenes and the state of the atmosphere at the respective recording times will undoubtedly vary (Mather 2004).

4.2.1 Geometric Correction

Image geometry errors can arise due to systematic and non-systematic distortions during the satellite's scanning process. Systematic distortions result from the motions of the platform and its scanners (scan time skew) relative to the earth's rotation as well as from the fact that spatial resolution varies from the image centre to the swath edge (panoramic effect). Non-systematic distortions arise from instabilities occurring in the satellite's orbit and

from terrain-induced feature displacements orthogonal to the nadir line (KUENZER 2005, JENSEN 1986, RICHARDS AND JIA 2006).

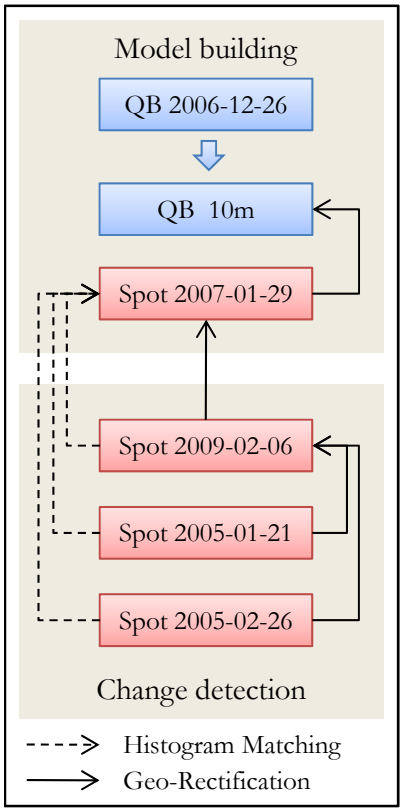

Fig. 4-2: Geometric Correction and Histogram Matching

The fact that the subsequent model building process and the change detection application are based on pixel-by-pixel comparisons, it is of utmost importance that the pixels of the respective images are positioned to correspond with one another. Since the absolute positions according to a Cartesian coordinate system were not imperative, an image-to-image registration was chosen, instead of absolute georeferencing. Thereby, one image serves as a master to which the others, known as the slaves, are to be registered. The method depends upon establishing mathematical relationships between the locations of pixels in the slave image and the corresponding coordinates of the pixels in the master image (RICHARDS and JIA 2006). Due to the difficulties attached to the registering of SAR to optical images and the very accurate spatial coincidence of the TSX and QB scenes, the latter was chosen as the master image whereas the 2007 SPOT scene, in a first step, constituted the slave image (see Fig. 4-2). To overcome the difficulties of finding common Ground Control Points attributable to the large difference in pixel size, the QB image was rescaled to fit the spatial resolution of the SPOT scenes. Subsequently, the SPOT 2009 scene was co-registered to the SPOT 2007 scene. Thereby, some difficulties arose due to the limited overlapping areas of the images, which prevented the even distribution of Ground Control Points over the entire scene. For the change detection application the SPOT 2005 images were then co-registered to the SPOT 2009 scene.

For all corrections the mapping functions were chosen as polynomials of the first and second order. Polynomial coefficients were estimated by about 25-30 pairs of Ground Control Points and a root mean square error (RMSE) of less than 0.5 pixels was obtained. A nearest-neighbour resampling algorithm was chosen to transfer the pixels with their original brightness values to the corresponding display grid location.

4.2.2 Radiometric Correction

Radiometric errors result from distortions arising from the sensor and from the influence of the atmosphere (RICHARDS and JIA 2006). The latter results from the fact that the atmosphere is a transmission medium, through which radiation is affected by absorption and scattering on the way from the source to the sensor (Richards and Jia 2006, Jensen 1986). In addition, the reflectance of a surface varies with the viewing angle, as well as with the solar illumination angle, which is especially severe if the sensor is capable of off-nadir viewing such as the SPOT HRG sensor (MATHER 2004). The variation in reflection intensity implies that depending on the recording conditions, same surface materials can result in varying brightness values which hamper the extraction of reliable terrain information. Due to Rayleigh and Mie scattering, the effects of the atmosphere are higher in the visible blue band in comparison to the middle infrared band (RICHARDS and JIA 2006).

4.2.2.1 Atmospheric Correction

In order to account for these radiometric biases, radiative transfer models such as MODTRAN are developed to estimate the atmospheric propagation of electromagnetic radiation for various conditions of the atmosphere.

In this study, the atmospheric correction was carried out for all SPOT scenes with the software package ATCOR-2. By specifying the influence of the atmosphere, solar illumination, sensor viewing geometry and terrain information for every image, ATCOR calculates an individual, sensor-specific look-up table (LUT) based on the MODTRAN4 code (BERK et al. 1998) which is then applied to the respective scene. More information about the functionality of ATCOR-2/3 can be found at (RICHTER 2008). Fig. 4-3 demonstrates the radiometric enhancement of a SPOT subset after atmospheric correction with ATCOR.

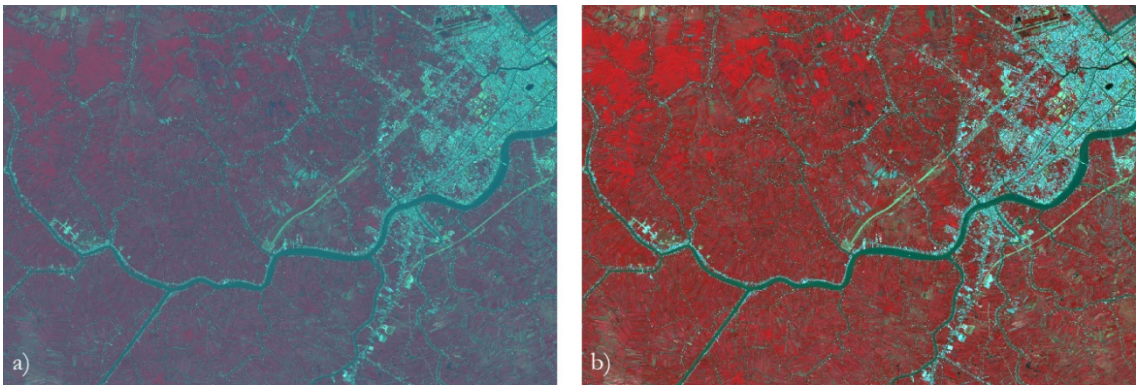

Fig. 4-3: Subset of the original image a) and of the enhanced image after atmospheric correction b)

4.2.2.2 Histogram Matching

In addition to the atmospheric correction, the histograms of the application data were matched to those of the SPOT training image. FIG. 4-5 and the corresponding TABLE 4-3 demonstrate the radiometric differences for each band between the 2007 training image and the corresponding bands of the 2009 application scene, after atmospheric correction and histogram matching. The offset on the diagonal for each plot in FIG. 4-5 indicates the atmospheric distortion in brightness for each spectral band. It can be seen that when compared to the original images (left column), the brightness values converged after atmospheric correction (middle column), though radiometric discrepancies still remained too high. The implication of these divergences is that the utilisation of one standardised regression model for all application data would have clear limitations. For this reason, histograms were matched to further minimise the brightness value variations across the scenes (right column).

In the histogram matching procedure, a look-up table of the reference image is mathematically derived which serves as a function for converting the histograms of the input images. In order to obtain optimal results, it is important that the look-up table to be calculated represents the area of interest as closely as possible. This required therefore an initial preparation of the reference image according to the following criteria:

The first criterion was that the reference and input histograms were based on the same relative distribution of land cover. This was assured by clipping the reference image to the intersecting area of the input scenes.

The second criterion entailed that only areas significant for the impervious surface estimation were included. By excluding irrelevant areas such as cultivated land, wetlands or water areas, the reference look-up table solely represents the pixel values within settlement areas. This was done respectively, by either extracting built-up areas using the settlement mask derived from the TSX scenes (see CHAPTER 5.1), or by excluding vegetation areas using a NDVI threshold (see CHAPTER 2.2).

The third criterion required that only areas were included in the reference histogram which had not been subject to land cover changes, in relation to the respective input data. This was assured by applying an image differencing method (for detailed descriptions see CHAPTER 0) involving the separate subtraction of each application image from the reference image. The fundamental principle of remote sensing implies that a difference in the spectral response of a pixel on two dates must exist when land undergoes a change or dis-

turbance between two dates (JENSEN 1996). Consequently, the resulting differential values were positive and negative (max ±255) in areas of radiance change and zero in areas of no change. Assuming that especially high deviations arise from land cover changes on the ground, all pixels featuring differences in brightness over one or two standard deviations respectively were defined as "real change" and consequently, were excluded from the histogram calculation.

In order to find the most appropriate reference histogram, four masks were derived which were specifically tailored for each application image and differed according to the combination of the above mentioned criteria:

- MASK A: only the *intersecting* area AND the *settlement* areas
- MASK B: only the *intersecting* area AND *settlement* areas AND *change* areas below *two standard deviations*
- MASK C: only the *intersecting* area AND *change* areas below *one standard deviation*
- MASK D: only the *intersecting* area AND *built-up* areas (NDVI mask) AND *change* areas below *two standard deviations*

The masks were then statistically evaluated by comparing the histogram-matched pixel values with those of the reference image (computation of mean, absolute mean, standard deviation) according to FIG. 4-4. Thereby, the best results were obtained by using MASK B, shown in TABLE 4-3.

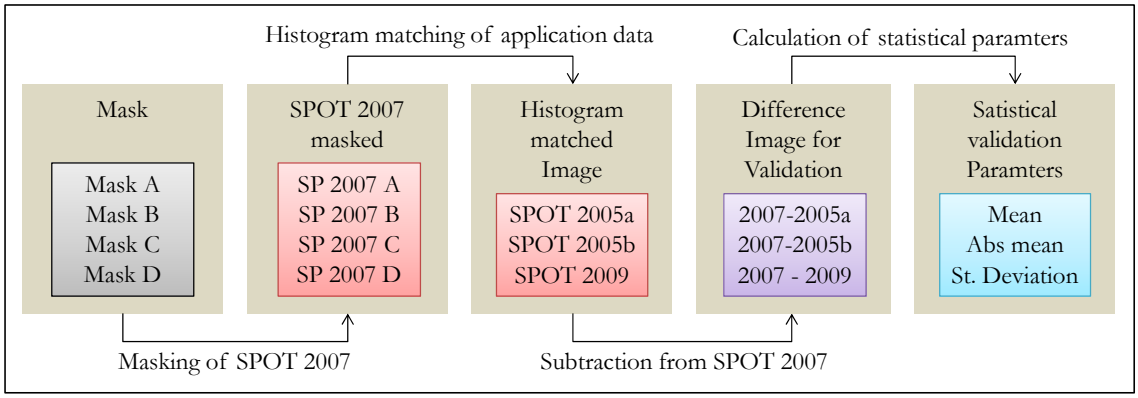

Fig. 4-4: Workflow of the histogram matching

Table 4-3: Average deviation and fluctuation of the 2007 and 2009 SPOT pixels for each band of the original scenes (Org), after atmospheric correction (Atm) and after histogram matching (His)

	Mean Org	Sd Org	Mean Atm	Sd Atm	Mean His	Sd His
green	50,5	8,4	3,9	6,5	1,4	6,15
red	39,4	12,8	4,2	8,2	1,9	7,6
nir	-30,9	14,5	12,8	22,0	-2,8	20,2
mir	15,2	12,6	20,3	11,4	0,2	11,1

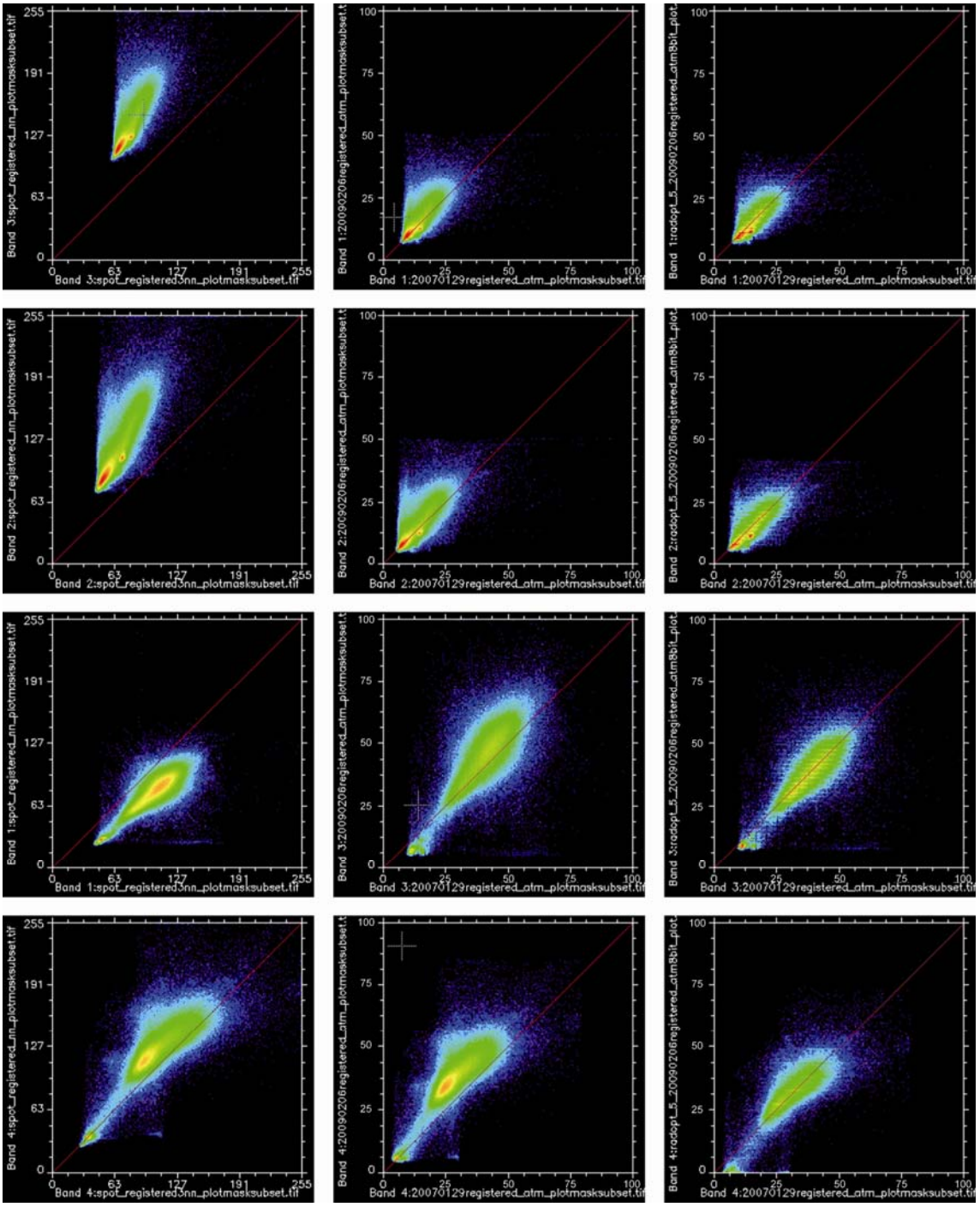

Fig. 4-5: 2007 SPOT pixels (horizontal axis) plotted against 2009 SPOT pixels (vertical axis) for each band (row) of the original scenes (left column), after atmospheric correction (middle column) and histogram matching (right column)

The matching of the histograms was conducted with an IDL software tool (KIERMAIER 2010), which is based on an iterative regression method. The algorithm automatically plots the input pixel values against the values of the reference image, in order to compute the look-up table by means of an iterative optimisation procedure using standard descriptive statistical and regression methods.

4.2.3 Pansharpening

The preprocessing of the QB reference image comprised the enhancement of the spatial resolution by an image fusion technique. Image fusion can lead to more reliable results in image classification and to increased interpretation capabilities by reducing spatial ambiguities (POHL and VAN GENDEREN 1998). The concept of all fusion techniques is to combine two or more different images to form a new enhanced image. In the context of this study, the 2.4 m monochromatic bands of the QB scene were merged with its panchromatic band featuring a spatial resolution of 0.6 m. By doing so, the assets of the multispectral bands were combined with those of the panchromatic band, to produce a fused image with high spectral and spatial resolutions. In order to gain an advantage for a subsequent classification, it is important to preserve the spectral properties. Therefore, a spectral preserve fusion technique was applied, as developed by LIU (2000). The main concept of this method is the so-called Smoothing Filter-based Intensity Modulation (SFIM). By using a ratio between a higher resolution image and its low-pass filtered image, spatial details can be modulated to a co-registered, lower resolution multispectral image. According to LIU (2000), this technique is superior for improving spatial detail of multispectral images with their spectral properties reliably preserved, when compared with other techniques such as the HSI and Brovey pansharpening approach. FIG. 4-6 shows the original images and the result of the resolution merge for an image detail of the QB scene.

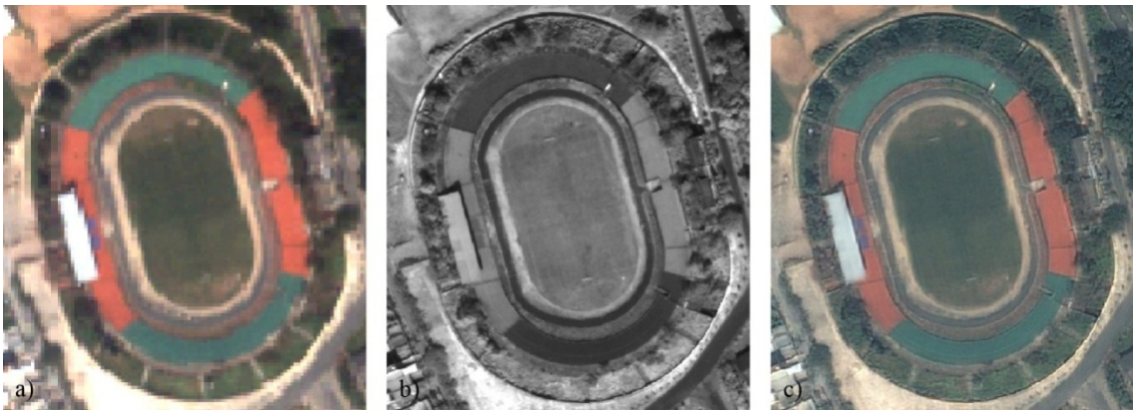

Fig. 4-6: Multispectral low resolution QB bands a) ; panchromatic high resolution QB band b); enhanced multispectral high resolution QB bands c).

Chapter 5

Methodology

If a spatially inclusive and comprehensive estimation of IS coverage is the goal, it is necessary to separate the natural environment or cultivated land from developed/urban areas, so that impervious surface estimation focuses exclusively on the settlement areas. There are several reasons for this:

Firstly, by solely focusing on the settlement areas, the accuracy of the IS estimation can be improved. Bare soil and barren land often feature similar spectral properties like that of built-up land and therefore indicate high values of imperviousness in the resulting IS maps. Within urban environments, high IS values for these land cover types are in most cases appropriate. In rural or natural environments however, these land cover types are generally characterised by high infiltration rates (see CHAPTER 2.1). Secondly, average IS thresholds for example used to indicate environmental quality on district levels (ARNOLD and GIBBONS 1996) are normally calculated on the basis of settlement areas only and without reference to the region as a whole, making a corresponding settlement mask for such analyses indispensable. Finally, the fact that IS modelling is applied to wide-spread regions means that calculation efforts can be significantly decreased by masking out irrelevant areas, thereby accelerating the whole modelling process.

ESCH et al. (2007, 2009) used LULC vector data of the German Official Topographic Cartographic Information System (ATKIS) to identify the relevant settlement areas. All non relevant areas, defined as those not related to transport or commercial/industrial/residential land use, were identified in a GIS and excluded from the subsequent impervious surface estimation process.

In this study, an approach developed by ESCH et al. (2008, 2010) was applied which identifies settlement areas by a semi automated detection method on the basis of single-polarized TSX data. Thereby, the distinct texture and the high density of dihedral corner reflectors prevailing in built-up areas are utilized to reconstruct the settlement body by the use of an object-based image classification method. The settlement footprints then served as the reference area for the impervious surface estimation by masking out all non-settlement areas from the application data (see FIG. 5-1).

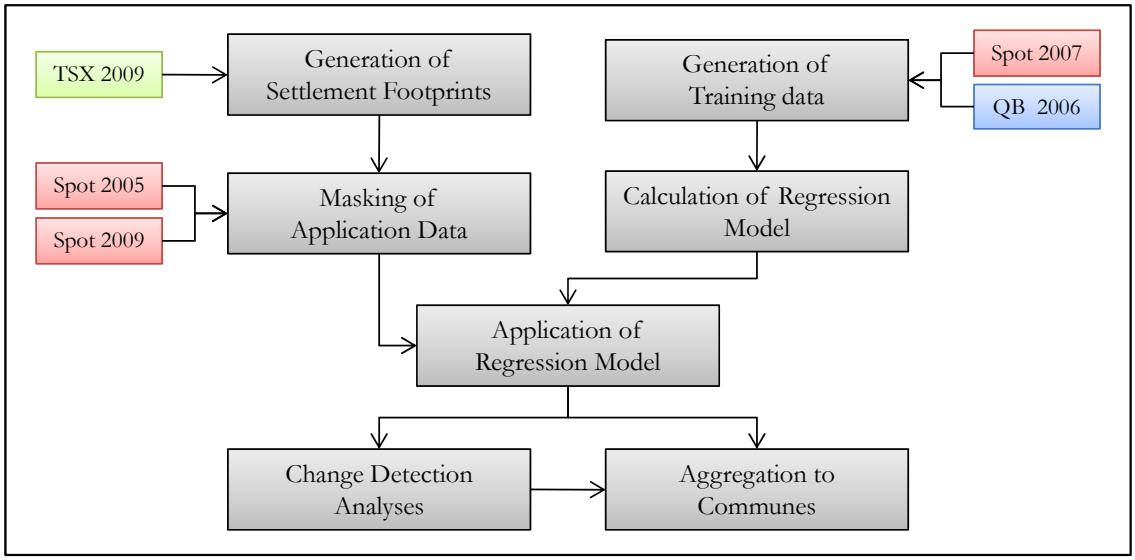

Fig. 5-1: Methodical concept of impervious surface mapping using optical and SAR remote sensing data

The actual approach for impervious surface estimation applied was based on the studies of Esch et al. (2007, 2009). The methodology allows subpixel urban IS to be quantified as a continuous variable for large area assessments by utilizing multisensor datasets of different spatial resolutions. The approach is based on a Support Vector Regression model (see CHAPTER 0), that maps pixel values of medium resolution data to IS percentages by means of a machine learning algorithm. The training data which is necessary to build the regression model was derived respectively, from high resolution LU vector data (ESCH et al. 2009) or high resolution IKONOS satellite data in the study of ESCH et al. (2007).

In this study (see FIG. 5-1), the training data was obtained from pansharpened QB imagery with a spatial resolution of 0.6 m. In a first step, on the basis of the QB subset a land cover map was derived by an object based image classification approach. Secondly, the specific land cover categories were assigned characteristic values of IS estimates. The resulting IS grid was then rescaled from 0.6 m to 10 m producing a training grid of actual subpixel IS cover, that matches the grid system of a corresponding SPOT subset. Together these data

formed the training basis used to build a SV regression model, which statistically correlates percent IS to the spectral reflectance of the SPOT pixels.

Finally, the regression model was applied to the modified application data which comprised SPOT5 scenes from 2005 and 2009, clipped to the settlement areas of the study area, in order to derive subpixel IS estimates at 10 m resolution. The derived impervious surface maps formed the foundation for further processing steps, such as change detection analysis or the calculation of average IS values for administrative units.

5.1 Delineation of Settlement Footprints

In this chapter, the approach for the automated delineation of settlement areas is elucidated in detail. Preceding this, the requirements of such masks for impervious surface calculation are discussed.

5.1.1 The ontology of a settlement

The perspective and contextual framework in which a phenomenon is perceived is defined as its domain. Depending on the domain, a perceptive scheme of knowledge leads to defining criteria which typically describe that particular phenomenon. This set of criteria is known as its ontology (HOFMANN et al. 2008). With this in mind, the phenomenon settlement has to be examined from the perspective of two different domains: On the one hand, it is crucial to analyse the phenomenon settlement according to the requirements of its contextual use in impervious surface estimation. On the other hand, the phenomenon settlement, examined from a SAR image domain, results in a different ontology than when describing settlements in reality or from optical imagery.

5.1.1.1 Settlement in the context of impervious surface estimation

This study aims to assess the percentage of IS cover occurring within the area of settlements. Within this context, it becomes clear that the area of interest not only focuses on apparent non-vegetative, structures such as buildings or roads defining the 'built environment' (Schneider et al. 2010), but also includes all other manifestations of urban life such as municipal parks, enclosures, ponds, gardens or other open spaces. Consequently, settlement is understood as a land-use category comprising heterogeneous mixtures of impervi-

ous (cement, asphalt, concrete), pervious (grass, shrubs, and trees) and other (water, bare soil) land-cover classes (RIDD 1995, SCHNEIDER et al. 2010). The built environment however, remains the dominant characteristic of the settlements.

A further aim of this work is to identify and quantify changes in IS cover. In this context, areas showing high construction activities are of considerable interest. Logically, these do not predominate in the areas of existing high settlement density in the centre, but are located in the more sensitive, outer perimeters which are still characterised by a rather scattered land occupation and a relatively small degree of built environment. In light of this, rather than adopting a conservative definition restricting the area of interest to the core settlement body, a generous interpretation of the term 'settlement' is more suitable, which also includes settlement structures undergoing development.

The settlement mask is also intended to be used as a reference basis for calculating average IS values for administrative units. A narrow definition of 'settlement' however leads to higher average IS values compared to a more generous definition of 'settlement', encompassing higher fractions of pervious surface cover within the boundary. This phenomenon, known as the Modifiable Arial Unit Problem (MAUP) (OPENSHAW and TAYLOR 1979), can easily lead to wrong conclusions when comparing statistical aggregated results without paying attention to their respective calculation basis. Assuming that many policy decisions are based on the associations obtained from such aggregated data (YANG 2010), it is important to provide a clear conceptual definition of the reference area which, when provided together with the statistical results, ensure an objective and robust basis for comparisons. This especially applies to the rather ambiguous phenomenon of settlements.

5.1.1.2 Settlement from a SAR image domain

The characteristics most typical for built-up areas were concisely described by WINDLER and WINKLER (1950): settlements are characterised by a high density of buildings, arranged in an anisotropic manner showing a certain degree of cohesion. When examining a phenomenon from the perspective of the image domain, a different set of descriptive criteria forming its ontology is needed than that pertaining to a real world domain (HOFMANN et al. 2008). This fact is especially evident when applied to image analyses with radar data: microwave backscatter primarily determined by structural and dielectric attributes of the illuminated ground target (see CHAPTER 2.6.2.) bear no direct relationship to their counterparts in the visible part of the spectrum, these being dependent on reflective characteristics

of the earth's surface (RIEDEL et al. 2008, LILLESAND et al. 2004). Consequently, microwave responses require a markedly different "view" on settlements compared to views obtained by optical data or by observing settlements in real life (LILLESAND et al. 2004). When evaluating the definition of WINDLER and WINKLER (1950) from a microwave remote sensing perspective, buildings can be assumed in radar images based on patterns of spatially limited areas of very high intensity values, as house walls form dihedral corner reflectors and constitute sources of layover and foreshortening effects. Furthermore, flat areas such as streets, gardens, or parking lots in the direct vicinity of vertical structures result in shadow effects and high levels of mesoscale surface roughness, resulting in a specific and distinct image texture in SAR images. By using an object based image analysis approach, which facilitates the inclusion of topological properties in the classification process, the anisotropic nature of settlements, i.e. the distinct degree of cohesion, can be utilized for their identification.

5.1.2 Object-based extraction of settlement areas

The approach presented here was developed by ESCH et al. (2008, 2010) in order to classify urban areas as a land-use category on the basis of single-polarized TSX intensity images. So far, the method had only been selectively tested on high density metropolitan areas. The transfer of this method to impervious surface estimation analysis however, demanded different requirements to the approach as previously mentioned. In addition, the large area mapping of settlement areas had to encompass both high density structures in urban environments and low density structures prevailing in the rural areas. Furthermore, the method had not yet been applied to areas strongly characterised by naturally-occurring and man-made hydrologic elements, such as found in Can Tho Province.

The semi-automatic approach could be categorised into four main steps. First of all, a standardised texture image was generated which served, together with the intensity image, as a basis for the image classification. As this is an object-based approach, carried out by means of the object-oriented image analysis software *eCognition*, the second and third steps comprised the image segmentation and the classification procedure. The last step incorporated the generalisation and smoothing of the classification results.

5.1.2.1 Generation of Texture Image based on Speckle Analysis

When radar images are interpreted, a feature widely used to discriminate between different land-use types is the texture of the image, which in many cases can be more useful than the actual image tone (ULABY et al. 1986, RIEDEL et al. 2008). Image texture describes the variation in tone which arises from the varying scattering properties of a target, elucidated in CHAPTER 2.6.2. This intrinsic image texture however is always superimposed by speckle noise occurring as a random pattern of brighter and darker pixels (ESCH et al. 2010, FRULLA et al. 2000) , distorting the true image-information (see CHAPTER 2.6.3). Fully developed speckle, prevailing over homogenous areas follows a Gaussian distribution, while in heterogeneous areas such as urban landscapes, the multiple scattering processes within a resolution cell generally shows a directional behaviour, resulting in an anisotropic distribution of speckle noise (ULABY et al. 1986, FRULLA et al. 2000, ESCH et al. 2010). In view of this, it can be assumed that the deviation from fully developed speckle at a given point rises with an increasing quantity of true structures within the extent of a resolution cell (ESCH et al. 2010). This characteristic can be utilized by subtracting a scene specific, theoretical random variable of fully developed speckle – the so called *scene specific speckle heterogeneity* C_{th}, from the local variability in image tone – *the local image heterogeneity* $C_{x,y}$. In this way, a standardised texture parameter, the so-called *local speckle divergence* $D_{x,y}$ is generated, accentuating the anisotropic behaviour of speckle within heterogonous areas. Homogenous areas in turn, always feature values near to zero in the resulting texture image, independent of the system parameters of the SAR or raw-data processing steps applied.

In general, the level of speckle is proportional to the average brightness of a region, featuring a standard deviation that is a constant fraction of the local image tone (RYERSON et al. 1998). Consequently, a widely accepted statistical measure used to quantify speckle in SAR data is the coefficient of variation C which is defined as the ratio of the standard deviation σ to the mean μ and thus, provides a normalized measure of dispersion:

$$C = \frac{\sigma}{\mu} \tag{5.1}$$

Local image heterogeneity

The *local image heterogeneity* $C_{x,y}$ can be calculated by the local coefficient of variation which is defined as:

$$C_{x,y} = \frac{\sigma_{x,y}}{\mu_{x,y}} \tag{5.2}$$

Whereby $\sigma_{x,y}$ is the local standard deviation, and $\mu_{x,y}$ the local mean calculated in a defined, local neighbourhood surrounding each pixel. A critical issue when applying local parameter operations is the choice of the kernel to be used for calculation. In general, an increase in kernel size results in statistically more significant and reliable results, but on the other hand also blurs and smoothes the relevant texture and transition zones resulting in a loss of spatial detail. In addition, high kernel sizes lead to a drastic increase in computational efforts. FRULLA et al. (2000) plotted the coefficient of variation for typical homogenous and heterogeneous areas as a function of the window size. Their results showed that for pixels within homogenous regions, the coefficient of variation remained approximately constant with increasing window sizes, whilst in heterogeneous areas, the coefficient varied up to a value of 11*11 pixels, from which point it remained unchanged. ESCH et al. (2010) pointed out that kernel sizes less than 9*9 pixels generally led to a poorly developed structuring, whilst very large kernels of 99*99 pixels for example, resulted in very smooth structures inappropriate for complex urban environments. RIEDEL, TIEL and SCHMULLIUS (2008) recognized a significant increase in classification performance alongside increasing kernel sizes and maintained that the loss of spatial detail is largely compensated, when using an object-based classification strategy. They finally used a 23*23 window size in order to generate a texture image for mapping urban areas from SAR data. In this study, a window size of 15*15 pixels was chosen for calculating the *local coefficient of variation* which coincided with the kernel size, used by ESCH et al. (2010) and lay between the critical value of 11 pixels and the resource-intensive window size of 23 pixels.

Scene-specific speckle heterogeneity

The *scene-specific speckle heterogeneity* C_{th} was derived by using a formula of ULABY et al. (1986) who developed statistical image models to separate the spatial variability attributable to scene texture from that to speckle, respectively. Thereby, the speckle random variable is dependent on the equivalent number of looks N, used in the context of raw data processing (see CHAPTER 2.6.3), which can be calculated by multiplying the effective number of looks in azimuth L_a and range L_r direction, generally reported in the metadata:

$$N = L_a * L_r \tag{5.3}$$

Since the probability density function (PDF) of fully developed speckle is an exponential distribution in the case of a single-look image, the PDF for an N-look image is the convolution of N exponential distributions, resulting in a gamma distribution Γ (Ulaby et al. 1986). In this respect, the mean value of the speckle random variable for an N-look inten-

sity image is also based on the gamma distribution, dependent on the equivalent number of looks:

$$\mu = \frac{\Gamma(N + 1/2)}{N^{1/2}\,\Gamma(N)} \tag{5.4}$$

The standard deviation can then be calculated from (5.4) by:

$$\sigma = \sqrt{1 - \mu^2} \tag{5.5}$$

Finally, the theoretical C_{th} can be calculated from (5.4) and (5.5) by the coefficient of variation C using equation (5.1).

Local speckle divergence

The *local speckle divergence* $D_{x,y}$ can then be quantified by subtracting the *scene specific coefficient of variation* from the *local estimated coefficient of variation*:

$$D_{x,y} = C_{x,y} - C_{th} \tag{5.6}$$

The resulting texture image $D_{x,y}$ showed low values within homogenous areas, such as cultivated land or water areas and mid to high values within more heterogeneous areas, indicating the presence of settlements. However, $D_{x,y}$ also showed some local irregularities to this trend, as extremely high values occurred along the margins of areas with significantly differing image tones. This was particularly apparent at the borderlines between water and land areas (see FIG. 5-2). As these high values distract from actual settlement structures and so, distort the classification process, these locally restricted effects were diminished by means of spatial smoothing. Thus, according to the recommendation of ESCH et al. (2010) the texture layer was averaged by applying a local mean filter with a kernel size of 13x13 pixels.

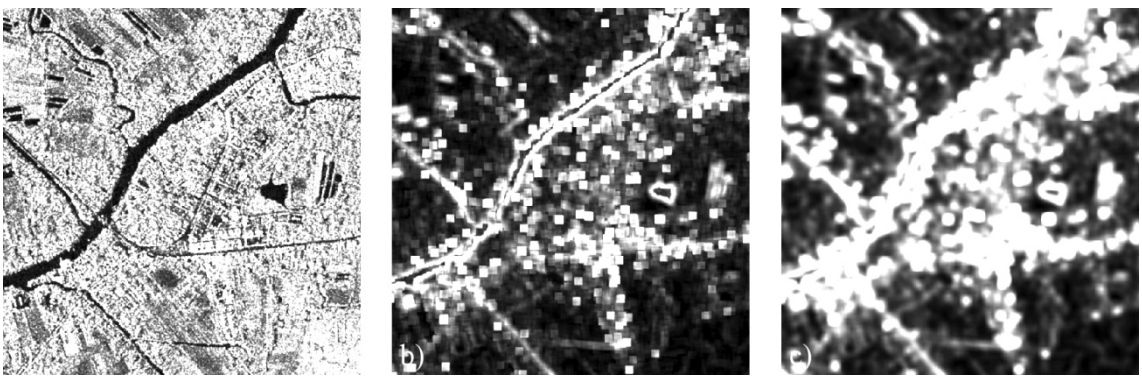

Fig. 5-2: Appearance of water areas in the intensity image a); in the original texture image b); and in the smoothed texture image c)

5.1.2.2 Object-oriented segmentation based on the intensity image

Image segmentation is the first step towards classification using OBIA and should not be underestimated, if accurate mapping results are to be achieved. Using eCognition with its multi-resolution segmentation, it is possible to generate several segmentation levels which are linked to each other in a hierarchical manner (BAATZ and SCHÄPE 2000). According to the method of (Esch et al. 2010), a top-down segmentation approach was performed on the original intensity image, resulting in two segmentation levels of different scales (see FIG. 5-3). These consisted of *Level 1* (L1) featuring large-scale segments in order to roughly delineate potential urban areas, and *Level 0* (L0) with comparably small image objects. In order to find the most suitable segmentation parameter for L1, different thresholds were compared with those used by ESCH et al. (2010). As the thresholds of the latter also seemed to be appropriate for the scenes in this work, a scale parameter of 150, a shape factor of 0.3 and a compactness of 0.8 were chosen. While L1 held image objects which coincided with the main large-scale structures such as settlement units, agricultural sections, and other objects of comparable size, small-scale features such as rooftops, single trees or small road segments, became merged with the surrounding area. The diverse spatial variations in back-scatter properties of these features however are essential for the identification of built-up areas and consequently, have to be represented by individual objects (ESCH et al. 2010). Hence, for the generation of the segmentation level L0 the scale parameter was set to 25, resulting in significantly smaller segments measuring up to one pixel in size. Such small object sizes, in combination with the large coverage of TSX Stripmap scenes, however pose a serious challenge when using standard desktop computers for image segmentation. Therefore, the segmentation at L0 was only applied to potential urban areas which were identified according to criteria, typical for urban environments: the existence of dihedral corner reflectors which could be assumed to exist when objects had high differences in intensity $I_{x,y}$ between darkest and brightest pixels; and high mesoscale surface roughness implying high average texture values $D_{x,y}$ (ESCH et al. 2010). The thresholds were determined by means of a trial and error procedure. In this study, the computational performance was inferior compared to optimal classification results and therefore, thresholds were set quite generously to ensure that no potential urban structures were overlooked.

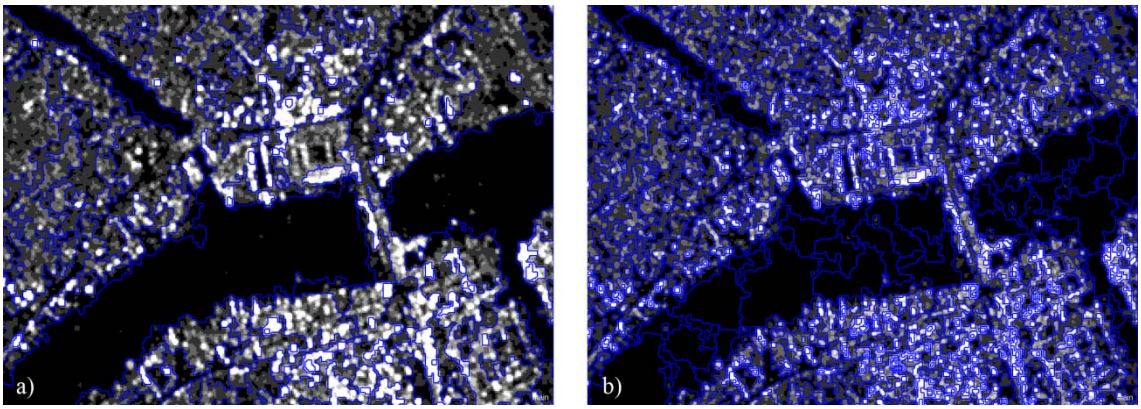

Fig. 5-3: Segmentation levels L1 with courser image objects a); and the finer segmentation level L0 b)

5.1.2.3 Object-oriented classification

The classification approach of ESCH et al. (2010) was adopted to fit the needs of impervious surface calculation as well as those of the local settlement structures. Additionally, an algorithm for classifying water was implemented, and a special morphological filter was applied to retrieve the final settlement footprints.

Based on the objects of the fine segmentation level L0, the approach utilizes the most typical characteristics of built-up areas mentioned afore; based on an iterative region-growing approach constituting five methodical steps (see FIG. 5-4).

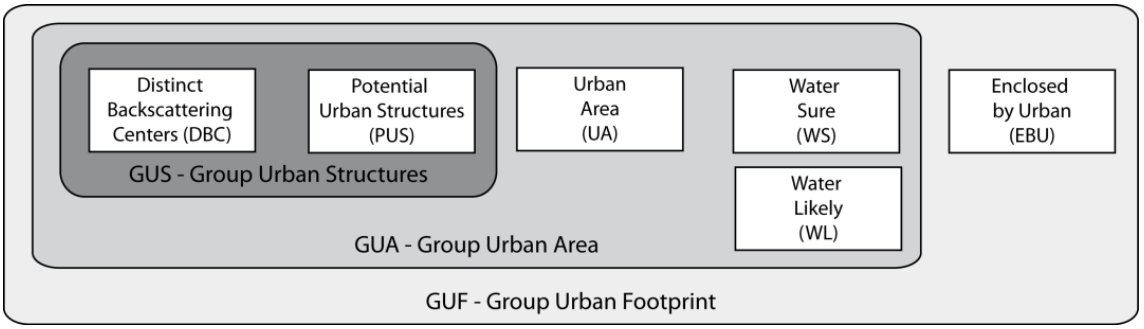

Fig. 5-4: Schematic concept of object-oriented classification procedure of urban footprints

Identifying Seed Objects

As mentioned above, settlements are generally well accentuated by bright spots in SAR images due to dihedral or trihedral corner reflectors. The first classification step therefore aimed to identify the corresponding image objects characterised by an extraordinary high intensity and texture value. Thus, a class *distinct backscattering centre* (DBC) was set up to classify all objects which had a minimum intensity value $I_{x,y}$ of 300 and a minimum texture value $D_{x,y}$ of 1200 (see FIG. 5-5a).

Extending Seed Objects:

DBCs are not exclusive to purely urban environments as natural vertical structures such as trees, hedges or riverbanks can also lead to double-bounce effects (RYERSON et al. 1998). In urban environments however, vertical man-made structures such as buildings, lamp-posts, walls etc. are distributed in a highly concentrated, anisotropic manner forming patterns of distinct DBC clustering; a unique characteristic that rarely occurs in the context of natural land cover types (ESCH et al. 2010). Hence, the analysis subsequently focused on the vicinity of the DBC objects in order to identify further structural elements, indicative of settlements, so called *potential urban structures* (PUS). PUS objects have to feature high intensity values similar to DBC objects and in addition, have to feature at least 3 DBCs in a neighbourhood of 40 pixels. Because of the additional limiting vicinity criterion, the threshold value for $I_{x,y}$ could be reduced to 200. DBC and PUS objects together form the abstract class *Group Urban Structures* GUS (see FIG. 5-4 and FIG. 5-5b).

Building the settlement area:

The goal of the third classification step was to reconstruct the body of the settlement by filling the gaps between the GUS objects. Again, an iterative region-growing approach was used to utilize the anisotropic distribution of man-made structures: potential *urban area* (UA) objects have to feature a minimum speckle divergence value $D_{x,y}$ of 1000 in combination with at least 15 existing *Group Urban Area* (GUA) objects, in the surrounding area of 25 pixels. GUA is a semantic group which comprise all GUS and UA objects (see FIG. 5-4). Consequently, the first cycle is based solely on the existence of GUS objects. Subsequently, the next iteration loop also includes the UA objects classified in the preceding cycle. The classification is repeated until no further segments are designated as GUA. In this way, areas which initially featured a high density of GUS object were successively classified as UA objects (see FIG. 5-5c). Furthermore, additional rules were added to prevent the classification of water surfaces as UA. Potential UA objects have to feature a minimum intensity value of 62 or a very high speckle divergence value $D_{x,y}$ of 8000, whilst their super-object (L1) has to exceed an intensity value $I_{x,y}$ of 55. Finally, isolated GUS objects which did not have any UA objects in a neighbourhood of 10 pixels were identified, in order to exclude them from the GUA class.

Identifying water areas

Water surfaces within the settlement areas were classified as a separate land cover type. Therefore, all unclassified objects were assigned to the class *water sure,* if the image intensity $I_{x,y}$ did not exceed a value of 60 and shared at least 30% of their border with GUA objects. As the class *water sure* also belongs to the semantic class GUA (see FIG. 5-4), the classification extended with each cycle, from the edges towards the isolated objects in the centre of the water areas. However, some water surfaces still remained unclassified as they exceeded an intensity value of 60, and for this reason a subclass of *water sure*, *water likely* was introduced. The threshold for the maximum $I_{x,y}$ value was therefore increased to 100, making it necessary to implement further limitations: objects have to share a common border of 50% with GUA objects and 10% with water sure objects. Again, the identification was carried out until no further segments were assigned to the class *water likely* (see FIG. 5-5d).

Building the final footprint

The last step of the classification procedure comprised the identification of unclassified areas completely enclosed by GUA objects which were then assigned to the class '*enclosed by urban'* (EBU). Following this, all EBU objects having common borders were merged and classified according to their size: EBU objects showing a cumulative area larger than 10000 pixels were removed from the EBU class on the assumption that objects of this size represent open land, not belonging to the settlement area. The remaining EBU objects were then combined together with the GUA class to the semantic group '*urban footprint'* (GUF), on the assumption that objects of this size represent areas belonging to the normal urban topography (see FIG. 5-5e,f).

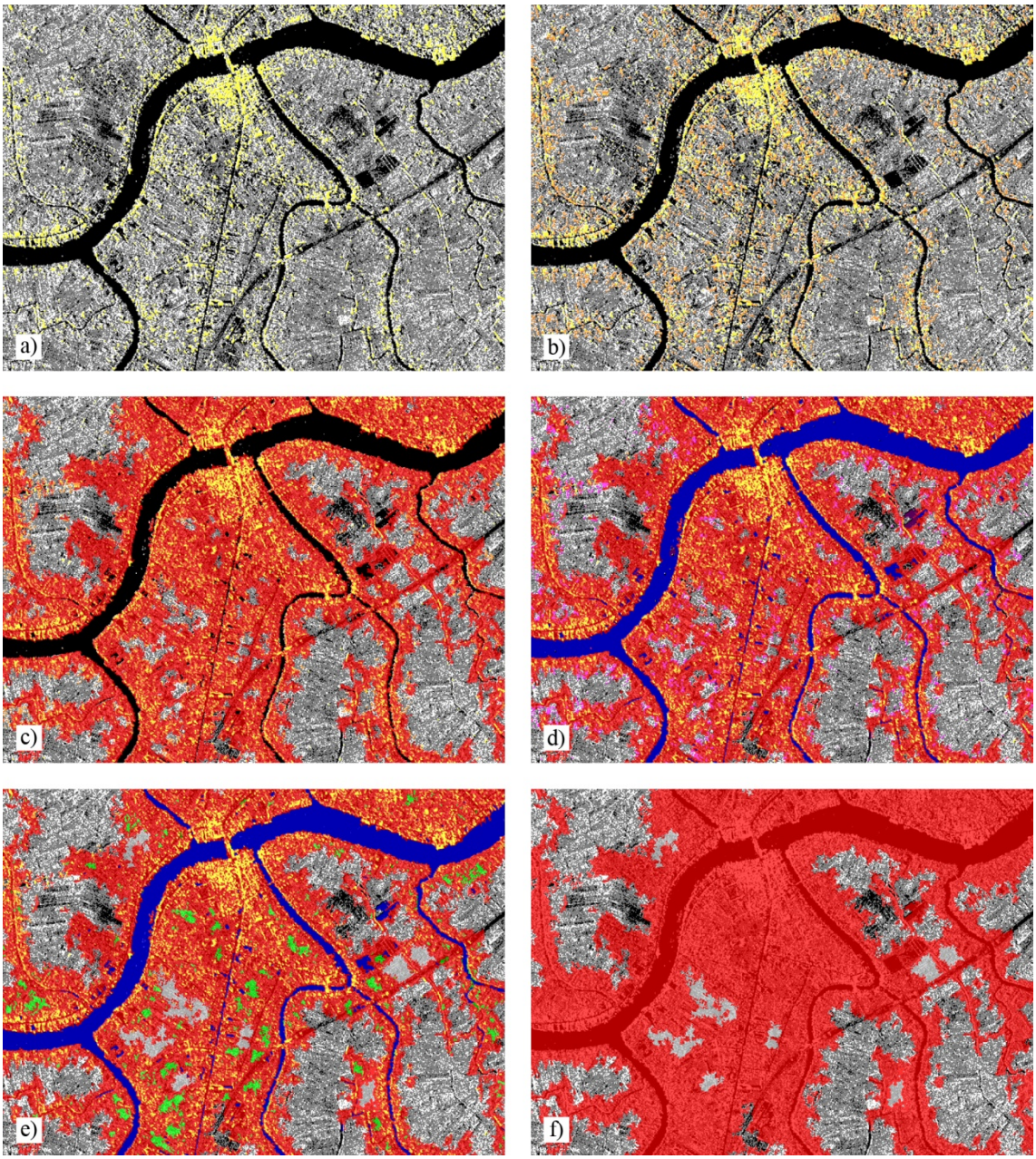

Fig. 5-5: Sequence of classification steps. Identification of DBCs a); PUS b); UA c); Water d); EBU e); and the final settlement footprint GUF f)

5.1.2.4 Smoothing

GUF objects were exported as a grid file for a subsequent pixel-based generalisation and smoothing process which was carried out by using the model maker in ERDAS Imagine. The generalisation processing was carried out by applying several filters, following the closing concept of mathematical morphology. Therefore, an initial morphological dilation was applied to settlement areas only, using a maximum filter and a window size of 11*11 pixels. In this way, the settlement areas were buffered and settlement fragments lying in direct proximity were connected. This was followed by applying a morphological erosion process

to the settlement areas, using a minimum filter and a window size of 11*11 pixels. This aimed to eliminate small objects which had not been merged by the dilation process and to restore objects to their original size. A majority filter with a window size of 17*17 pixels was applied separately after the dilation and erosion process, in order to smooth the edges of the settlement footprint.

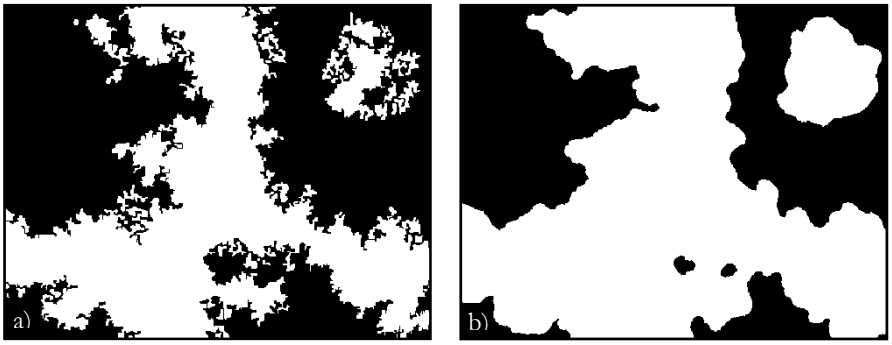

Fig. 5-6: Original settlement areas a); settlement areas with smoothed borders b)

5.2 Preparation of the training data

Training data in general are usually understood as a group of known items, which can be split into training items to be classified and their respective training labels, which together are used for further image classification (see CHAPTER 2.3). Within the context of impervious surface estimation, the SPOT pixels are the training items each associated with an individual value of imperviousness as their respective labels. In this chapter, the preparation of the training IS values for use in the training procedure is elucidated in detail. A schematic representation of the workflow is illustrated in FIG. 5-7. Firstly, a mask was generated on the basis of the pansharpened QB subset (FIG. 5-7a) by classifying the image into sealed, unsealed, and other areas (FIG. 5-7b). This was done by an object-based classification approach requiring prior image segmentation. Subsequently, the mask was rescaled to a coarser resolution (FIG. 5-7c-e) in order to correspond with the pixels of the application data.

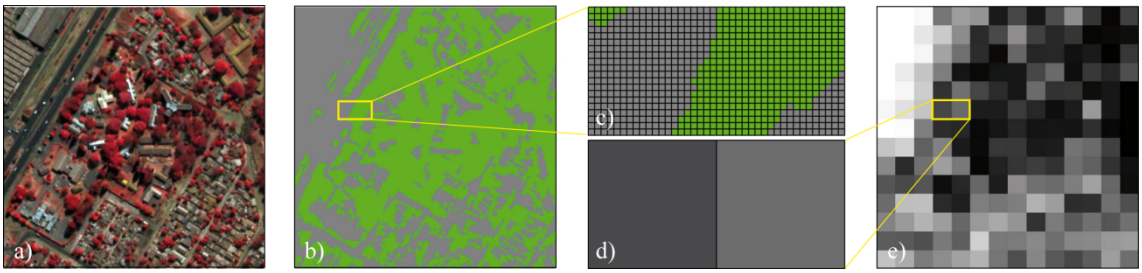

Fig. 5-7: Methodical concept of IS training data preparation

5.2.1 Segmentation

As already mentioned, the segmentation procedure is an important step towards image classification. Within this procedure, segmentation was based on eCognition's multi-resolution segmentation (BAATZ and SCHÄPE 2000) thereby using all four bands - blue, green, red and NIR - of the pansharpened QB scene. In addition, an iterative segmentation optimisation algorithm (ESCH 2006) was applied which facilitates multi-scale image objects within one single segmentation level.

Firstly, two segmentation levels were generated linked in a bottom-up hierarchy: the *base level* holding objects representing the smallest patches of interest in the scene, followed by the *optimisation level*, holding slightly coarser image objects due to a higher scale parameter value. The nature of the scale parameter implies that, compared with the objects of the optimisation level, the segments of the *base level* are characterised by smaller segments with higher homogeneity within itself and higher heterogeneity between the individual objects respectively. The segmentation optimisation starts by comparing every object of the base level (*subobject*) with its superordinate object (*superobject*) of the optimisation level according to its spectral heterogeneity. Those subobjects which differ significantly in their spectral properties actually have to be represented by an individual object on the optimisation level. Therefore, these objects are classified as significant subobjects and are subsequently integrated as individual objects into the segmentation structure of the optimisation level (see FIG. 5-8). The first cycle of the optimisation procedure ends by renaming the base level. For the subsequent iteration the modified optimisation level is appointed to the new base level, and the scale parameter for the new optimisation level is increased. The procedure continues in a new cycle and ends once more with the renaming of the new base level. The cycle is iterated until the largest objects of the final optimisation level adequately represent the largest patches of interest within the image.

The degree of similarity between sub and super-object is defined by the level of correspondence relating to the objects' spectral reflectance properties and to their absolute brightness values. The first criterion is realised by comparing the offset of the DN between sub- and super-object over all bands, whereby only the parallelism of the spectral signatures are taken into account. However, a marked difference in the absolute values of reflectance between two materials featuring a similar spectral signature can exist. In light of this, the second criterion evaluates the absolute level of reflectance between sub- and super-object

by considering the deviation of the objects' brightness, which is defined as the mean of all four bands.

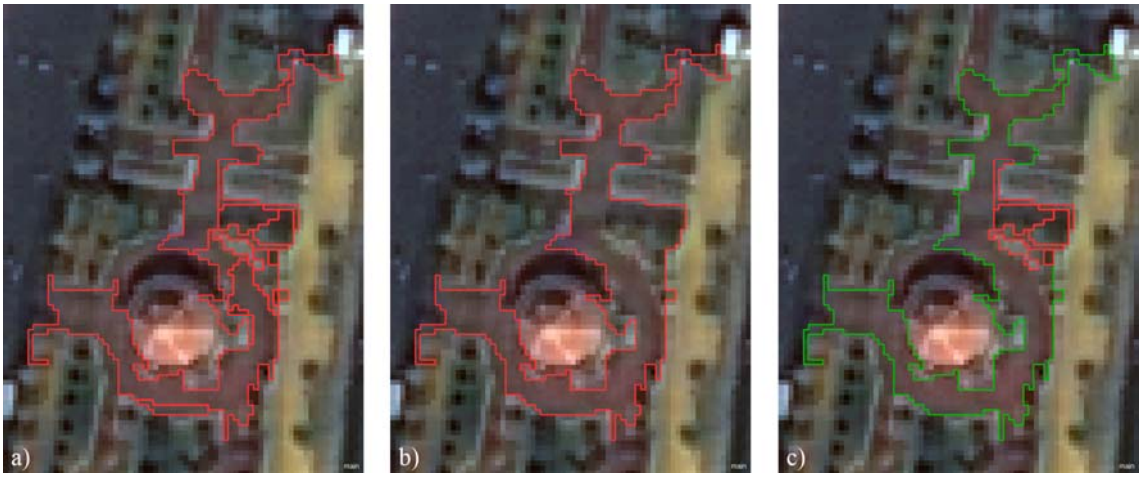

Fig. 5-8: Segmentation optimisation showing the base level a); the initial optimisation level b); and the modified optimisation level (significant subobjects in red) c)

5.2.2 Classification

The objective of the classification procedure was to identify two main categories, namely impervious and pervious areas. In addition, bare soil and water areas were classified as separate categories, as these land-cover types cannot be clearly assigned to either of the two previously mentioned classes. The image classification was based on the definition of fuzzy membership rules, the basic functionality of which was already explained in CHAPTER 2.4. The attributes used for the classification were partly based on the attribute selection of TAUBENBÖCK (2008) who developed a rule-based classification approach in order to classify urban land cover from VHR optical satellite data. Since the membership rules in most cases comprised numerous combinations of the object features, a detailed elucidation would be too involved at this point and thus is not provided here. Consequently, only the main characteristics of the individual class descriptions utilized for feature extraction are presented, together with the object- and class-related features used, as listed in TABLE 5-1.

In the first step, only objects were classified which were most easily distinguishable and could be identified without any ambiguity. These comprised vegetation areas and mostly larger objects, resulting from homogenous spectral reflectance properties. Large homogeneous areas of water could be identified by their size and characteristic low reflectance properties in the near infrared band. In order to detect large ponds and flooded paddy fields, typically featuring rectangular shapes, the additional shape parameter *length/width* was applied. Vegetation patches were classified by the sole use of the NDVI. Large areas of

bare soil, generally featuring a spectral similarity to built-up areas, were detected according to their brighter surfaces, their irregular shape, or their very large sizes in comparison to open spaces covered by tar or concrete (TAUBENBÖCK 2008). Subsequently, the most obvious streets were identified by making use of their characteristic elongated shape. Shadows, caused by tall buildings or tree crowns, were identified by facilitating the very low brightness values of corresponding objects which were defined as the mean value of all four bands. All objects which could not be identified unambiguously remained unclassified. Furthermore, built-up areas with the exception of streets also remained unclassified.

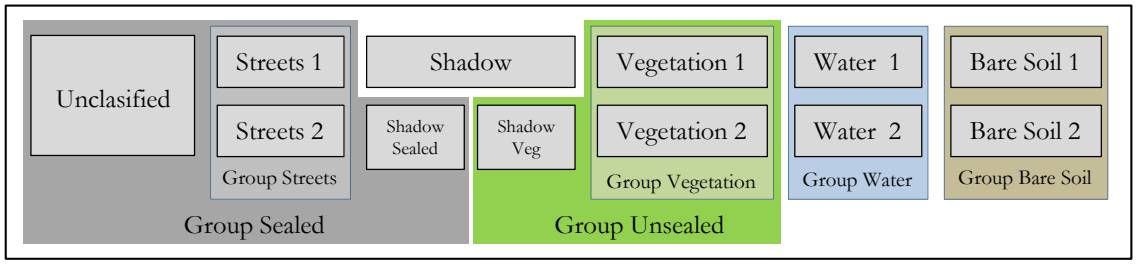

Fig. 5-9: Classes and semantic groups in the classification process

In the second step, the existing classification was extended to the remaining unclassified objects. Therefore, thresholds for shape and object-related features were relaxed and additional class-related rules were introduced. Assuming that most land-cover types such as streets, rivers, or vegetation areas are characterised by an anisotropic pattern and a continuous spatial sequence, the objects classified in the first step served as seeds within their respective group to extend the classification to adjacent, more ambiguous objects (see FIG. 5-9). This was done by using the class-related feature r*elative border to,* specifying the proportion of mutual border which objects share with others of a defined class. Similar to the region-growing approach applied to water objects described in CHAPTER 5.2.2, the classification was iterated several times, so that the individual classes (water, street, bare soil, and vegetation) grew successively from the seed objects until all objects in their respective groups were identified. In this way, streets and rivers which were particularly characterised by spatially continuous courses were classified with high levels of reliability and accuracy. As incident radiation is significantly reduced within shaded areas, their ground cover type cannot generally be identified by their reflection characteristics and thus frequently cause uncertainty in the classification of urban environments (LU and WENG 2006, HUNG and GERMAINE 2008). In order to assign these areas as representative as possible to either sealed or unsealed land cover, shadow areas were divided into pervious or impervious land cover-categories, dependent on their surroundings. Those shadow areas which shared a common border of at least 50% with objects from the groups *vegetation* or *water*, were desig-

nated to the class *shadow vegetation*. Subsequently, *shadow vegetation* was combined with the group *vegetation* to form the group *unsealed*. Finally, streets and the remaining shadow areas formed together with the remaining unclassified built-up areas the group *sealed*.

Table 5-1: Object- and class-related features used for classification

	WATER	BARE SOIL	VEGETATION	SHADOW	STREETS
Step1	Area, Mean NIR, NDVI, Length/Width	Area, Brightness, NDVI, Length/Width, Ratio Green/Red, Length, NDVI	Area, NDVI	Area, Brightness	Length, Width, Length/Width, NDVI
Step2	Area, Mean NIR, Rel. border to Water (Step1)	Area, Brightness, NDVI, Rel. border to Bare soil (Step1)	NDVI, Rel. border to Vegetation (Step 1)	Rel. border to Vegetation or Water	Rel. border to Streets (Step1)

5.2.3 Reclassification

After exporting the land cover map, the classes were re-coded according to their characteristic degree of imperviousness. Assuming that rooftops, concrete, tarred and similar surface-cover completely prevent the infiltration of water, pixels of the class *sealed surface* were assigned the value of '1' representing 100% imperviousness. In contrast, it was assumed that vegetated areas totally constituted pervious materials and were, therefore, assigned the value of '0' to represent 0% imperviousness. In most studies, land-cover types with uncertain or ambiguous IS characteristics such as water or bare soil are either allocated to one of the above mentioned categories, or are totally excluded from the model generation. However, so far no research has been carried out to evaluate the effects of water or bare soil areas on the IS estimation of the remaining categories (i.e. sealed, vegetation). Consequently, in addition to an IS training dataset excluding water and bare soil areas, six more IS datasets were generated each holding a different value of imperviousness for bare soil and water, to analyse their impacts on the IS estimation performance (see TABLE 5-2). All values were converted to floating point format, in order to facilitate the exact calculation of averages in the course of the subsequent rescaling process.

Table 5-2: Training IS grids featuring various combinations of imperviousness for water and bare soil

LAYER	SEALED	VEGETATION	WATER	BARE SOIL
w0b0	1	0	0	0
w1b0	1	0	1	0
w0b1	1	0	0	1
w1b1	1	0	1	1
w0b05	1	0	0	0.5
w1b05	1	0	1	0.5
wxbx	1	0	-	-

5.2.4 Aggregation

In the last step of the preparation procedure, IS values were rescaled to fit the resolution of the application data, using the image processing software ENVI. Thereby, the individual IS values are aggregated within the extent of a SPOT resolution cell (10*10 m). As a SPOT pixel is not evenly divisible by a pansharpened QB pixel (0.6*0.6 m), the IS values are automatically weighted according to their contributing allotments, followed by the calculation of the weighted mean for each 10*10 m cell. Finally, the resulting values expressed percent IS for each SPOT pixel in a range between 0 and 1.0.

5.3 SVM training and IS modelling procedure

The training procedure, which constitutes the actual building of the model, as well as its subsequent application, was done using a stand-alone software tool especially developed for impervious surface estimation, by the Institute for Remote Sensing at Wurzburg University. The tool incorporates the SVM library LIBSVM for SVM classification, regression, distribution estimation and multi-class classification (CHIH-CHUNG and CHIH-JEN 2010).

The training data comprises all four bands of the 2007 SPOT subset as input values, and the corresponding training IS values generated from the QB subset as their labels. As the HRG sensor features a radiometric resolution of 8-bit, input values X form a subset of the natural numbers $\mathbb{N}$. The IS values are floating-point numbers ranging from 0 to 1. Thus, the labels constitute a subset of the real numbers $\mathbb{R}$ (HIMMLER 2008). Consequently, equation (2.2) mathematically defining the training set can be reformulated to:

$$S = \{(x_1, y_1), \ldots, (x_k, y_k)\} \subseteq \mathbb{N}^4 \times \mathbb{R} \tag{5.7}$$

Although the training IS values range between 0 (0%) and 1 (100%), the modelled IS estimations might be less than 0% or more than 100% imperviousness for a pixel. This can be attributed to the fact that the output values from the regression are only estimates and consequently scatter around the original input values. Since values outside the range of 0% and 100% are physically impossible, lower and upper bounds (minimum value: 0; maximum value: 1.0) are implemented in the SVR, which automatically reclassify estimates greater than 1 or less than 0 to these outer limits.

The SVM library LIBSVM facilitates the selection of various kernel types namely, a linear, polynomial, sigmoid, or a radial basis function. The latter was chosen in this study follow-

ing the recommendation of CHANG and LIN (2010) and BACHHOFER (2008) who tested the above mentioned kernel in IS calculation. In addition, the software tool incorporates an optimisation algorithm, which automatically finds the best settings by an iterative procedure: once the kernel type is chosen the algorithm uses a subset of the training data in order to systematically test various SVR parameters. This is done by calculating the difference between the modelled output values and the values provided by the training IS input data for each parameter combination. Those settings resulting in the lowest deviations are then chosen for the actual IS calculation (ESCH et al. 2007).

The training procedure results in a regression model, which can be stored in an external file. Thus, the model can be applied on various datasets independent of a previous training procedure. All in all, according to the different training data sets, seven different models were generated (see FIG. 5-10). Each model was then applied to the SPOT application data from 2005 and 2009, which had been previously clipped to the settlement areas by using the derived settlement masks, referred to in CHAPTER 5.1. As a result, corresponding impervious surface maps were obtained for each application scene.

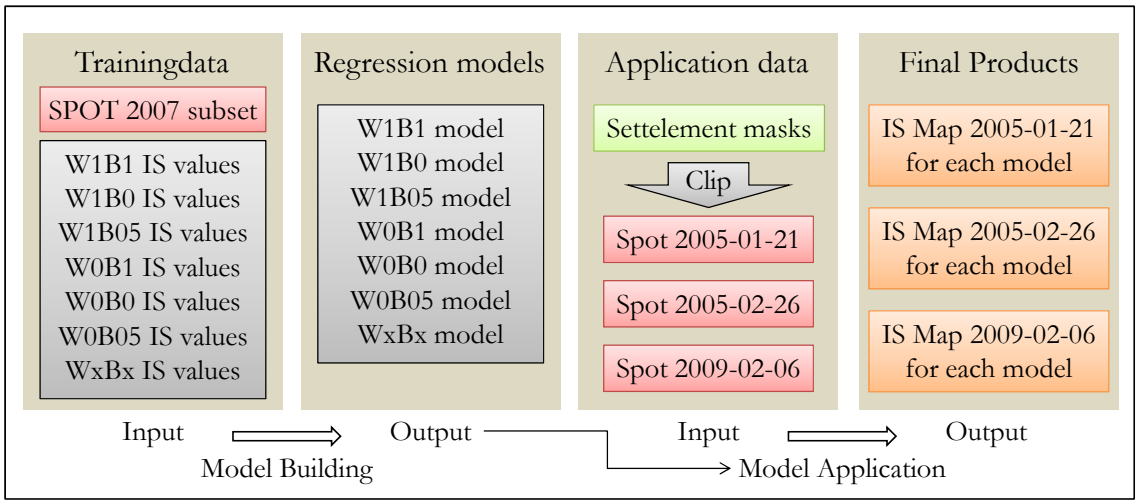

Fig. 5-10: Workflow of model building and model application

5.4 Change Detection Analysis

As mentioned at the beginning, it is the particularly densely populated southern part of Can Tho Province which is a highly dynamic region and where intensive urbanization and extensive agriculture must coexist. In view of the increasing conversion of agricultural land to suburban land, not only information about the degree of imperviousness at specific intervals is of interest, but also the amount of change and development in land consumption. Changes, primarily of a structural nature, are conventionally detected manually, based on a visual comparison of aerial photographs, which is both time consuming and costly (DEKKER et al. 2009). Thus, digital change detection methods were developed which correlate and compare two or more sets of aerial or satellite imagery, allowing an automated identification of LULC changes. In this chapter, a digital change detection method is described which was applied to detect changes in IS cover by using the previously derived impervious surface maps.

Although some object-based change detection approaches exist, most methods are based on comparing two or more datasets, pixel-by-pixel. With some exceptions, the wide range of change detection methods can basically be categorized in three main methodical groups: classification, change vector analyses and image algebra (NIEMEYER ET AL. 2008). Classification change detection methods require the previous classification of at least one of the images to be compared. The Post-classification Comparison for example, starts with an initial LULC classification of both datasets ('date 1' and 'date 2'). The pixels are then compared according to their respective class memberships and stored within a change detection matrix, from which "from-to" changes can easily be analysed. Within Spectral Change Vector Analysis, the spectral appearances of the pixels are directly compared without a preceding classification process. The location of each pixel in the feature space is compared according to each recording date. The vector describing the direction and magnitude of change from 'date 1' to 'date 2', is called a spectral change vector and reveals a lot of information, when correctly analysed (JENSEN 1996). In this work an Image Algebra Change Detection method was applied, which identifies the amount of change by directly comparing the pixel values through arithmetic operations, such as band rationing or image differencing.

The latter involves subtracting the imagery recorded on 'date 1' from that recorded on 'date 2'. The method was already applied within the course of radiometric correction, as referred to in CHAPTER 4.2.2.2. In this case, however, instead of reflexion values from image data,

percent impervious surface is subtracted. The histogram of the resulting difference image is assumed to follow a normal distribution, with its peak around zero indicating no change, whereas areas of change are represented by positive and negative values, reaching a potential range between -1 to 1 (see FIG. 5-11).

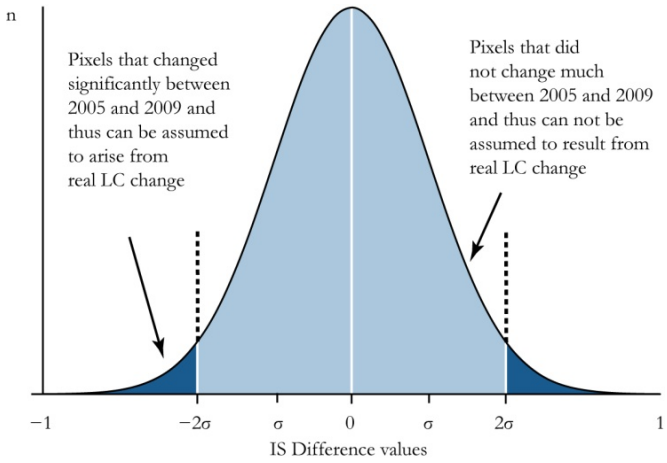

Fig. 5-11: Schematic diagram of the IS change histogram

It is evident however that unchanged areas on the land surface may also vary in their IS values. Consequently, the second step comprised the definition of threshold boundaries separating areas of real change from those which have not changed on the ground, but featured values other than '0' in the histogram. As the modelled values are only based upon a regression estimation, the uncertainty of the IS predictions has to be taken into account when defining the appropriate thresholds. In CHAPTER 5.6.3, the robustness or reliability of the regression model was evaluated by calculating the standard error between training and modelled IS values. Consequently, a range of two standard deviations (±0.3) was defined as a "confidence interval," in which the fluctuations around the mean value are not assumed to result from real changes. Deviations beyond this threshold were assumed to arise from real IS cover changes. Consequently, pixels featuring change values above ±0.3 were classified as significant IS increases or decreases accordingly. The classification was subsequently examined on the basis of high resolution QB images and was found to corroborate the chosen threshold values.

The change map was then transformed to a vector data format. As the change map covers a large extent, and the area of interest not only focuses on the inner centre of the city, small areas of change were excluded in order to match the level of detail to the respective working scale. Thus, the sizes of the individual polygons were determined, and only those with a minimum size of 300 m² (= 3 pixel) were regarded as *significant changes* and were represented

on the map. However, the level of detail determined by the minimum mapping unit is alterable according to the designated working scale and research question.

5.5 Calculation of IS averages for administrative units

The last processing step comprised the generation of average IS values as well as average IS change statistics for the administrative unit of a commune. Communes in Vietnam are the administrative units below the provinces in the administrative hierarchy of the country. Within the study area, there are a total of 84 communes of different sizes, which vary inversely proportional to the population density. A list of all communes within Can Tho Province can be found in ANNEX C.

In order to calculate average values for each commune, additional geodata was required, which was supplied by one of the Vietnamese Project Partners. The data constituted a vector file comprising all communes within the country. After extracting the communes located in the study area, the administrative units had to be reduced to the settlement areas only, in order to exclude non-relevant areas from the calculation process. This was done by intersecting the administrative units with the settlement footprints generated in CHAPTER 5.1, whereby the settlement areas were divided and marked according to their respective communes by an individual *Zone ID*. As water areas constitute neither pervious nor impervious entities, they had to be excluded from the reference area for aggregation. This was done by masking out all water areas from the modified settlement footprint by means of a water mask. The latter was derived from the TSX scenes 2009-01-24 and 2009-01-13 and was made available for this study by VERONIKA GTAIGER (2010).

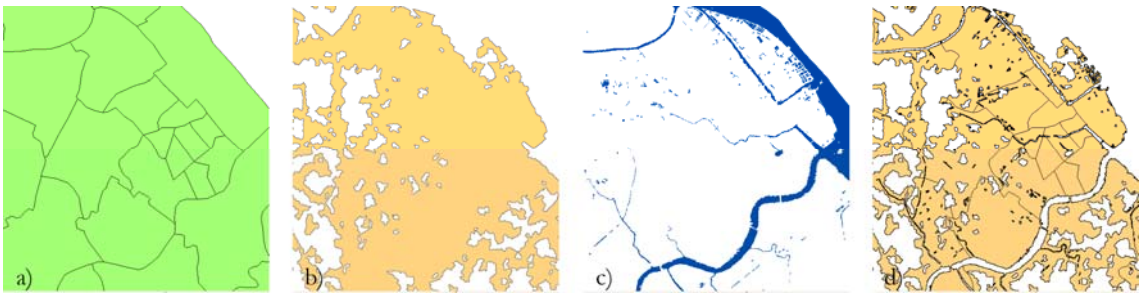

Fig. 5-12: Administrative units a); settlement footprint b); water mask c); calculation basis for aggregation process d)

The resulting reference area formed the calculation basis for the zonal aggregation. Hereby, the pixel values of the IS maps of 2005 and 2009, as well as the values of the generated IS

change map were each aggregated by means of a zonal Map Algebra function according to equation (5.8).

$$\frac{\sum_1^q ISV * A}{\sum_1^q A} \tag{5.8}$$

Here, ISV stands for the individual IS values of a pixel, A for its extent comprising 100m² and q for the number of pixels in a particular zone. Thereby equation (5.8) is applied separately to each zone, indicated by the zone ID. Finally, the resulting average values were attached as new attributes to the respective communes of the administrative vector layer.

5.6 Accuracy Assessment Methods

It is obligatory that the final results are assessed for accuracy so that reliable conclusions can be drawn. Furthermore, it is also necessary to evaluate the quality of the main intermediate data products, as any errors in these also affect the quality of the final result. Through the identification and correction of potential errors, the quality of the information ultimately derived can be increased and the work flow optimized.

In the following, the methodologies for determining the quality of the intermediate products, i.e. the settlement masks, the QB land-cover classification, and the SVR models, as well as of the final information products, i.e. the impervious surface masks are discussed in depth. The results of the accuracy assessments, together with the main sources of errors are then presented in the subsequent chapter.

5.6.1 Settlement Mask

For accuracy assessment to be useful, future users must be sure that the results of the assessment truly represent the accuracy of the map. Users must believe that the assessment is objective, and the validation results are repeatable (CONGALTON et al. 2009). As mentioned in CHAPTER 5.1.1, the phenomenon settlement is a depiction of land-use comprising heterogeneous mixtures of land cover types, and its interpretation is highly dependent on context and view point. Thus, it is not possible to reliably and unambiguously delineate settlements visually from other land-use categories, in the absence of further information such as land registry data, either from imagery or from the ground. Consequently, without a clear-cut rule for comparing the classification results with a true reference, variations in accuracy

will occur depending on the perception of the interpreter. Buildings can be relatively unambiguously identified from QB imagery. However, by limiting the concept of *settlements* to the footprints of buildings, the requirements of a settlement mask in the context of impervious surface estimation, are not fulfilled (see CHAPTER 5.1.1). Assuming that most of the pervious and impervious terrain features defining settlements are in direct vicinity of buildings, emanating from these, different radii of tolerances were introduced to represent the operational area of the inhabitants:

- Settlement definition S25 signifies all areas within *25 meters distance from a building.*
- Settlement definition S50 signifies all areas within *50 meters distance from a building.*
- Settlement definition S75 signifies all areas within *75 meters distance from a building.*
- Settlement definition S100 signifies all areas within *100 meters distance from a building*

These definitions provide a clear cut and transparent concept of the phenomenon *settlement* and fulfil the requirements of both accuracy assessment and those of impervious surface calculation, mentioned in CHAPTER 5.1.1. In addition, by applying successive radii, the suitability of the derived settlement masks can be evaluated according to different requirements of scale.

Fig. 5-13: Settlement mask and validation points with different radii (25m, 50m, 75m 100m)

All in all, 600 sample points were randomly distributed stratified to the proportions of the thematic classes (settlement or non-settlement), in order to ensure a constant sample density in each class. In order to account for the different settlement definitions, four different buffers (25m, 50m, 75m, 100m) were applied to each sample point (FIG. 5-13). By doing so, the relevant minimum distances to the next building for each sample could be easily categorised, according to the four definitions on the basis of VHR QuickBird scenes.

Two validation plots were selected, so that the classification results could be examined according to the prevailing settlement structure. Firstly, one plot was located in the urban outskirts of Can Tho City, with the second plot being located rurally in the outer fringe of the province (see FIG. 4-1a). Each plot spanned a quadratic area of 170km². As the QB

scenes were recorded in 2006, all errors of commission were subsequently checked against the SPOT scene 2009 and were corrected, when buildings could be identified within the respective radii. The classified results were then presented together with those of the reference, in the form of an error matrix according to the explanation in CHAPTER 2.5.

5.6.2 QB land-cover classification

The quality of the training data significantly affects the performance of the SVR model and ultimately, the accuracy of the derived IS estimations. All in all, four land-cover classes were derived - *vegetation*, *sealed surfaces*, *water* and *bare soil* – the accuracy of which had to be assessed. Initially, it was intended to validate the classification by examining ground truth data obtained on a field trip in February 2010. A visual comparison of the collected data with the QB scene, forming the basis of the classification, showed however that the time period of about three years, between the collection of the ground truth data and the image recording date, was too long as much change had taken place in the interim, on the ground.

For this reason, accuracy assessment took place by visually comparing the classification results with the actual ground cover situation of the QB image. The pan-sharpened high resolution subset with pixel sizes of 0.6 m supplied high levels of detail, thus ambiguities could be minimised in most cases. Altogether, 443 reference samples were randomly distributed, stratified to the proportions of land-cover, thereby ensuring a minimum number of samples in the category with the least representation, i.e. the bare soil class. Classification and reference results were then stored in an error matrix for further analyses.

5.6.3 Class-specific validation of the SVR models

In order to examine the performance of the SVR classifier, each regression model was applied to the SPOT training subset. The output values were then compared with the corresponding IS training values. By using the training data for model validation, external distortions such as those resulting from radiometric discrepancies could be eliminated. Consequently, deviations from the training values could be exclusively attributed to the performance of the SVR classifier.

However, training and testing on the same data set results in the overestimation of classification accuracy (CONGALTON 1991). To avoid this bias, a special case of cross- validation was applied. The so called Leave One Out (LOO) approach ensures that different pixels

are used to train the regression model than those used for validating it (RICHARDS and JIA 2006). Therefore, each of the seven IS training grids (1) was subdivided, resulting in two new modified IS datasets (see FIG. 5-14a). The division followed a systematic pattern, whereby one of five pixels (totalling 14454 of 72270 pixels) was removed for validation purposes (2), while the remaining pixels (3) were used together with the SPOT training pixels (4) for model building (5). After applying the models (6) to the SPOT training scene (4), the modelled output values were subtracted (7) from the IS values which remained for validation (2). The resulting differences ranged between -1 and 1 and represented deviations of imperviousness between 100% underestimation and 100% overestimation, respectively.

After transforming the pixels of the difference image into vector format (polygons), the deviations were analysed within a GIS, according to the derived land-cover classes from the QB scene (8). Therefore, each polygon was assigned the land-cover category in which its centroid lay (see FIG. 5-14b). Additionally, the polygons were labelled according to whether they represented mixed pixels, i.e. the polygons crossed the border of a land use class, or whether they represented pure pixels.

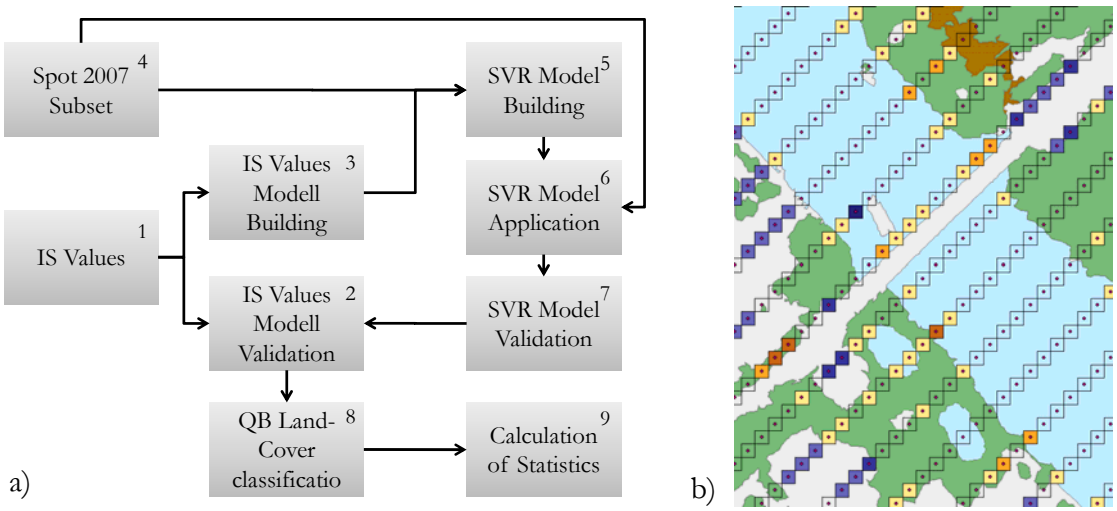

Fig. 5-14: Concept of SVR model validation a); difference values as polygons and spatially joined LC classes b)

In this way, accuracy measures could be calculated (9) for each class separately, which prevented that systematic under- and overestimations between the different land-cover categories were counter-balanced. As the deviations were assumed to be normally distributed, five different measures of descriptive statistics were calculated according to land-cover class and pixel type:

- Global Mean Error (ME): The mean value indicates the trend towards over or under estimation of the calculated impervious surface proportions, when compared with the training values.
- Global Absolute Mean Error (MAE): The absolute global mean indicates the absolute deviation of the estimated percentages of imperviousness from those of the reference data. Therefore, this measure is most significant for indicating the quality of the models.
- Absolute Standard Deviation (ASD): The absolute standard deviation indicates the dissemination of the difference values around the absolute mean value.
- Absolute MAX: indicates the maximal deviation between the modelled and the reference values.
- Absolute MIN: indicates the minimal deviation between the modelled and the reference values.

5.6.4 Site-specific validation of impervious surface maps

The validation of the SVR models presented above are based on the IS training values as reference data. These values do not however accurately reflect the real conditions on the ground, as the training data itself is based on generalised assumptions and thus is inevitably biased in relation to true conditions. As the SVR model validation only focuses on the assessment of the input-output relation, this kind of relative validation is sufficient. However, no reliable statements can be made in how far the modelled values reflect the actual situation on the ground. For this reason, an attempt was made to provide an absolute validation basis, which consists of ground truth information gathered during a field trip, in February 2010. During this time, exact coordinates were collected from several hundred locations in the area. Additionally, detailed information regarding ground cover and land use were documented, and photographs were taken from all cardinal directions. On the basis of this information and on the interpretation of the photographs, final assessments were made about the proportion of impervious surface cover in the locality. As this method constitutes a subjective assessment without additional empirical measurements, it is only reliable when evaluated in broad categories. Thus, five categories were defined according to which the conditions on the ground were rated (see TABLE 5-3 and FIG. 5-15). The IS values were reclassified respectively to a similar classification scheme featuring the same number of classes. In this way, a comparison to the actual category on the ground could be made, in the form of an error matrix.

Table 5-3: Classification scheme used for ground truth validation

GROUND TRUTH CLASSES	Unsealed	Predominantly unsealed	Balanced	Predominantly sealed	Sealed
IMPERVIOUS SURFACE CLASSES	0-20 %	20-40%	40-60%	60-80%	80-100%

Garden behind French colonial building, fruit trees 20 percent - unsealed

Garden with 2-level individual houses 20-40 percent - more unsealed than sealed

Rural settlement - mixed houses with garden 40-60 percent - balanced

CT-Binh Thuy-big road, high building density, 60-80 percent - more sealed than unsealed

Market hall, dense buildings, 100 percent - sealed

Fig. 5-15: Examples of ground truth information gathered at a field trip in February 2010

Chapter 6

Results

This chapter presents the results of the three intermediate products, namely the settlement footprints, the QB land-cover classification and the SVR models, as well as the results of the three final products – the impervious surface maps, the IS change map and the IS statistics per commune.

6.1 Settlement footprints

The settlement footprints derived from the TSX scenes are integrative elements of the impervious surface maps for 2005 and 2009, which are shown in FIG. 6-7 and FIG. 6-8 . The masks though also constitute an independent dataset, which can be used as a basis for other analyses.

The settlement structure of the study area showed a certain pattern, characteristic for the whole Mekong Delta, illustrated in FIG. 6-1. Typical for this region is the absence of individual, clearly demarcated settlements, these only occurring marginally. Instead, a characteristic pattern of continuous, linear settlements, following the course of the main channels and transport lines exists. Such settlements often constitute not more than a single row of buildings on either side of a channel with adjacent spaces for vegetable gardens, domestic animals, or ponds for shrimp farming. These elongated arrangements were especially prevalent in the rural, northern, and western parts of the study area showing clearly delineated structures. In the south and west, the lines of settlements took a more complex, fragmented course showing a pattern of winding ribbons, which branched out into the hinterland, a result of the higher population density and scarcity of building space. The highest

density of buildings was observed in Can Tho City, which comprised one, extensive, undifferentiated urban agglomeration.

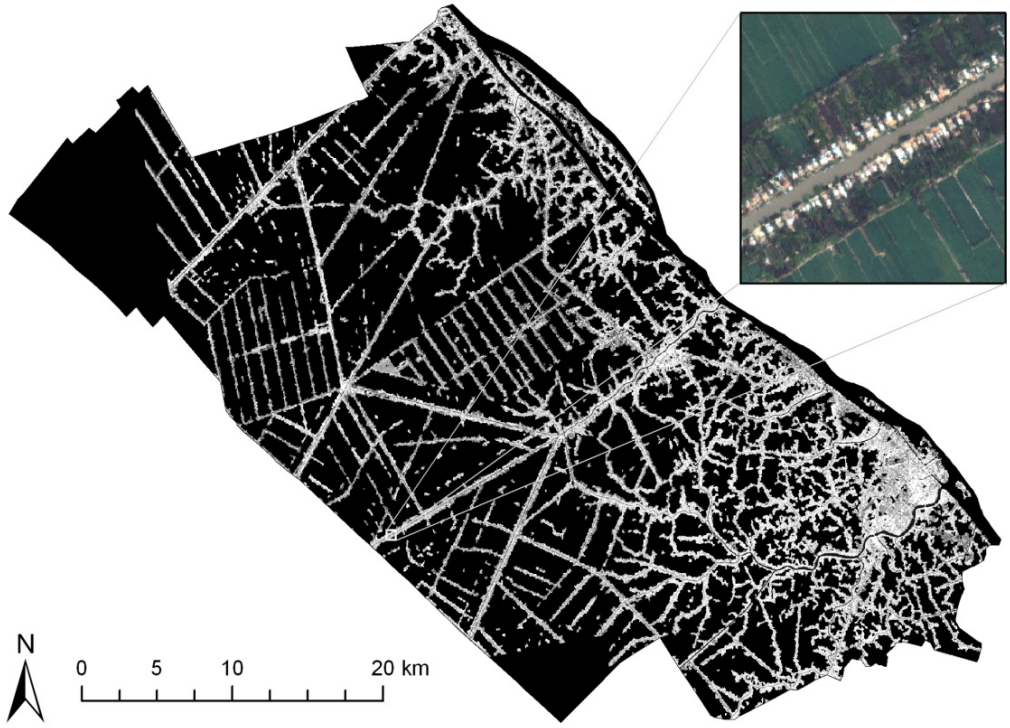

Fig. 6-1: Settlement Mask of Can Tho Province

The validation took place by checking the settlement footprints within two subsets (rural/urban) against 600 randomly distributed reference points, stratified according to the areal proportion of the classes. The vast majority of the errors occurred within the transition zones between settlement and non settlement areas. Thus, the application of the different reference areas (S25/S50/S75/S100) had high effects on the levels of user's and producer's accuracies. The results were organised in an error matrix (see TABLE D-2 and TABLE D-3 in ANNEX D) the basic functionality of which was elucidated in detail, in CHAPTER 2.5.

Errors of omission occurred where in spite of the presence of settlement structures, weak texture and insufficient point scatters were prevalent. This was the case in areas characterised by low mesoscale surface roughness and by insufficient vertical structures for corner reflectors. These areas mostly occurred in the transition zones between the main body of the settlement and the cultivated land/natural environment, where the density of buildings and other vertical structures gradually lessened. Thus, the main body of the settlements, best represented by the conservative settlement definition S25, was accurately identified, as texture here was well pronounced resulting in a high producer's accuracy of ~94% for rural areas and ~91% for urban areas (see TABLE 6-1). When extending the interpretation of a

settlement to the definition S100, areas were included with lower densities of corner reflectors and less pronounced texture and thus errors of omission increased, resulting in a producer's accuracy of ~69% for rural areas and ~74% for urban areas, respectively. Furthermore, in some cases vertical structures existed on the ground, but texture and point scatters were less developed in the image, as was the case in highly vegetated areas in the outer perimeters of the settlements and in the more rural districts. In these regions, the vegetation canopy obscured buildings, walls, corners, and other vertical structures. In addition to such "transition zone-induced errors", urban areas showing less pronounced height variations within the densely built city were also erroneously omitted, though these errors only occurred rarely and were locally restricted. Such omissions arose from flat features such as larger recreation areas, municipal parks, or lakes but also for example, from new building land designated for area coverage or an airport runway as shown in FIG. 6-2. In the intensity image (FIG. 6-2b) these areas feature dark and homogenous image tones, which can be attributed to their low micro- and macroscale surface roughness. Due to the homogeneity in tone, these regions also appear as dark areas in the texture image (FIG. 6-2c) and thus were not identified as settlement areas. The same principle applied to roads when not lying in direct proximity to other settlement structures of vertical character. The roads most affected from this omission were overland routes such as the section still under construction in FIG. 6-2.

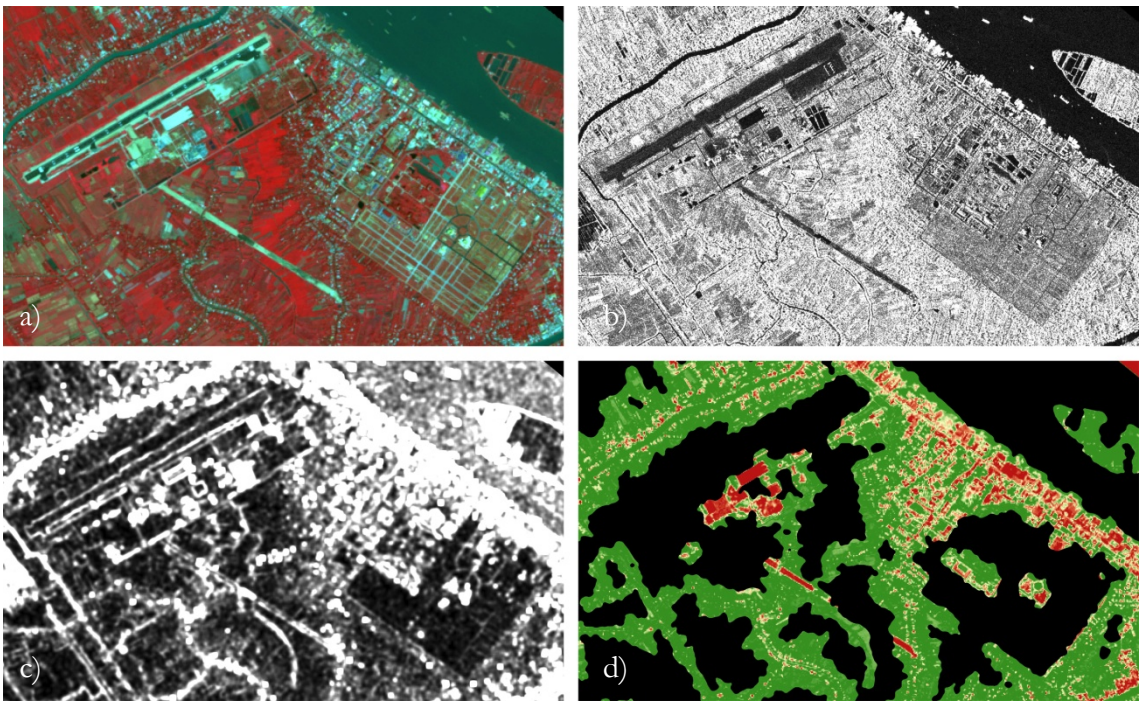

Fig. 6-2: SPOT subset a); intensity image b); texture image c); IS map showing settlement areas only d)

Errors of Commission occurred in areas where distinct textures and high densities of corner reflectors were prevalent, but were characterized by the absence of settlement structures. Dihedral corner reflectors originating from sources other than built-up structures, included river and canal banks, terrace escarpments, dams, sharp vegetation boundaries of paddy fields and palms, as well as the edges of aquaculture ponds. High texture values in the absence of settlement structures, mostly occurred in adjacent areas of contrasting radar reflectivity, such as at the boundaries between water and land surfaces. Water features, having a considerably smoother surface than land features, generally act as specular reflectors (see CHAPTER 2.6.2) resulting in very low return signals compared to the circumjacent land surfaces. In particular, the frequent alternation of channels and ponds with land segments, gave rise to especially high texture values in these areas. Furthermore, the edges of such ponds and river banks formed natural corner reflectors, so that these hydrologic-related facilities constituted the main source of commission errors in the study area. Although a lot of ponds were located in the direct vicinity of buildings, the extent of the water surface almost always exceeded the reference radius of 25m, explaining the rapid decline in user's accuracy for the settlement definition S25 (see TABLE 6-1). The degree of user's accuracy in this case lay between 57% for rural and 75% for urban areas, which improved significantly to a level of 95% and 99% respectively, when extending the reference area to 100m distance from a building (S100), thereby incorporating most aquaculture ponds, such as illustrated in Fig. 6-3.

Table 6-1: Accuracy measures for different settlement definitions

SETTLEMENT DEFINITION	OVERALL ACCURACY		USER'S ACCURACY		PRODUCER'S ACCURACY	
	Urban	Rural	Urban	Rural	Urban	Rural
S25	83%	91%	75%	57%	91%	94%
S50	89%	94%	93%	77%	86%	89%
S75	86%	92%	97%	85%	78%	77%
S100	81%	91%	99%	95%	74%	69%

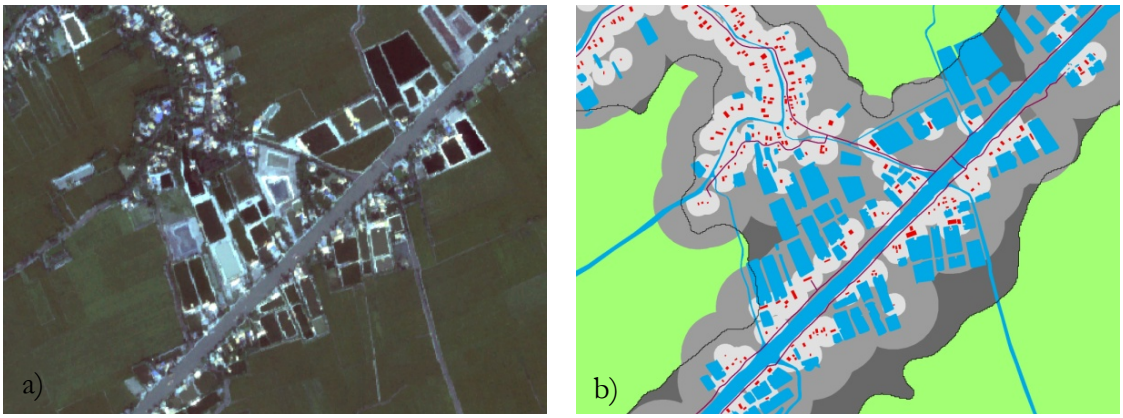

Fig. 6-3: Effect of aquaculture ponds. QB subset a) and settlement classification results (dark grey and black outline) together with the S25 (light grey) and S100 (medium grey) reference area b)

When comparing the results of the urban with those of the rural validation area, it is apparent that the latter showed significantly lower levels of user's accuracy (see TABLE 6-1). This can be attributed to the fact that particularly the rural areas are characterized by numerous channels and aquaculture ponds, causing more commission errors than in urban settings. Although user's accuracies were lower, overall accuracies for the rural subset were about 5-10% higher. The comparison of the spatial distribution of the classes showed that non-settlement areas were the dominant class (80%) in the rural validation scene forming extensive and highly compacted areas, in contrast to the rather fragmented distribution of the urban validation subset (see FIG. 6-4). Consequently, the non-settlement class in the rural subset was characterised by a lower proportion of perimeter relative to its area. As errors mainly occurred in transition zones between settlement and non-settlement areas, the risk of errors was lower for this class compared to non-settlement areas in the urban subset. As a result, the non-settlement class in the rural validation scene featured very high levels of accuracy (TABLE D-3 in ANNEX D.) and was responsible for the higher levels of overall accuracies in rural areas.

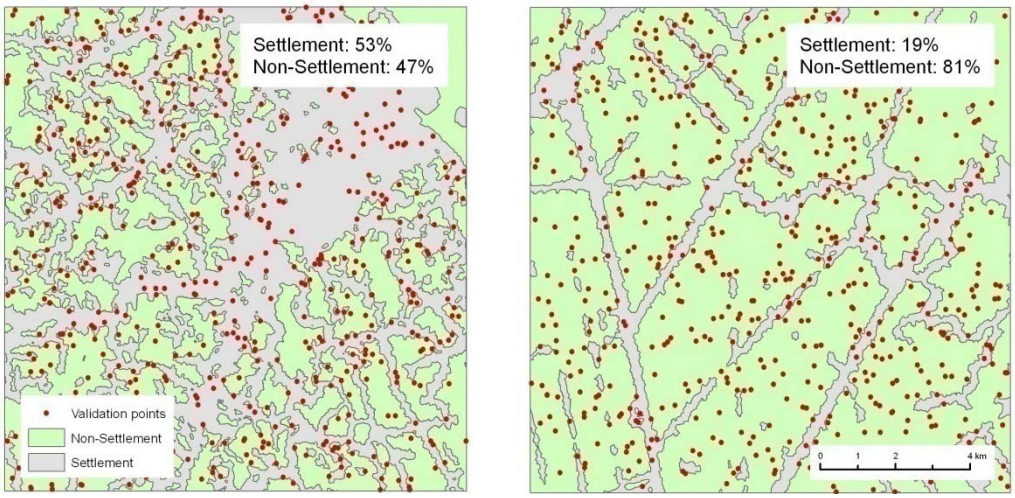

Fig. 6-4: Validation scenes resembling a typical urban and a typical rural area

6.2 QB land-cover classification

The land-cover classification of the QB subset is the second, intermediate product within the processing chain. The accuracy of the four thematic classes - *vegetation*, *water, sealed surfaces* and *bare soil* - was assessed by calculating an error matrix shown in TABLE D-1 in ANNEX D.

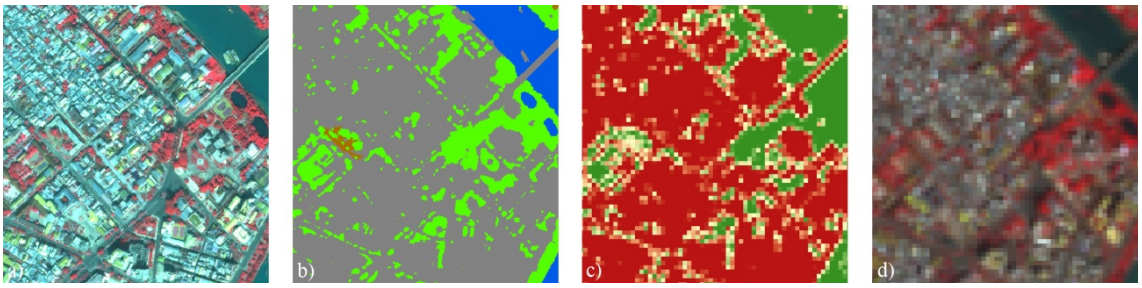

Fig. 6-5: Pansharpened QB image a); land-cover classification b); IS training values c); and corresponding SPOT5 pixels d)

The use of high resolution image data significantly reduced the mixed pixel problem and provided a basis on which higher levels of detail could be obtained, when compared with the SPOT training image (see FIG. 6-5). Single trees, small vegetation patches, water ponds, streets and individual buildings were correctly identified resulting in a detailed representation of the prevailing settlement structures. The accuracy of the classification was high with an overall accuracy of ~96% and only showed low differences in quality (< 4%) over the categories *water*, *vegetation* and *sealed surfaces* (see TABLE 6-2). The accuracy of the class *bare soil* however lay with a kappa of 86% below average though still gave a satisfactory result. The lower rate of accuracy arose from the well-known confusion when discriminating *bare soil* from non-photosynthetic *vegetation* and different kinds of impervious surface materials, due to their similarity in spectral properties (see FIG. 6-6). Since *bare soil* was only represented by a comparably small proportion of land cover within the QB subset, the accuracy of *bare soil* was mostly affected form this confusion when compared to vegetation or sealed surfaces.

In addition, some distortion related to shaded areas occurred, which were not covered by the error matrix. The incorrect assignment of shadow areas is a well known source of uncertainty when classifying urban environments from high resolution data. Although the implemented method which marked shadow objects as either sealed or vegetation areas worked quite well in most cases, there were still some false assignments. Furthermore, some large area shadows were so extensive that they obscured numerous pervious and impervious objects, so that a flat assignment of the whole shadow inevitably led to wrong results.

Table 6-2: Producer's and user's accuracy as well as the kappa coefficient of the QB land-cover classes

THEMATIC CLASS	PRODUCER'S ACCURACY	USER'S ACCURACY	KAPPA
Vegetation	99%	96%	98%
Sealed	96%	96%	98%
Water	99%	100%	97%
Bare soil	86%	92%	86%

6.3 SVR Models

All in all, seven SVR models were generated, which differed according to the assignments of the impervious characteristics of *water* and *bare soil* areas. These where then applied to the application data and additionally, within the course of the validation procedure, to the SPOT training scene. The latter was done in order to obtain a radiometric-stable validation basis from which the variations to the modelled IS values could be analyzed (see CHAPTER 5.6.3).

The modelled values demonstrated very high levels of concordance with the training IS-values when the mean deviations (ME) on the basis of the whole scene were examined (see TABLE 6-3). Mean Absolute Errors (MAE) and standard deviations (SD) however were with 8-10% and 13-15% considerably higher and revealed that over- and underestimations occurred which were finally balanced out.

Table 6-3: Global statistical measures for each SVR model

MODEL	MEAN (ME)	ABSOLUTE MEAN (MAE)	MINIMUM	MAXIMUM	STANDARD DEVIATION (SD)
W0B0	0.0060	0.0925	0	1	0.1455
W0B05	0.0072	0.0907	0	1	0.1247
W0B1	0.0031	0.0849	0	1	0.1329
W1B0	-0.0006	0.0962	0	1	0.1541
W1B05	0.0139	0.0950	0	1	0.1592
W1B1	-0.0043	0.0854	0	1	0.1396
WxBx[2]	-	-	-	-	-

When analyzing the results according to land-cover category, the individual contributions to the global MAEs became apparent (see TABLE D-4 and TABLE D-5 in ANNEX D). While IS values amongst the vegetated areas were systematically overestimated with MEs between +3% and +6%, those of sealed surfaces were underestimated featuring MEs between -5% and -10%. This was due to the automatic capping of the IS estimates to a range between 0 and 100% making it impossible for sealed areas to be overestimated or vegetated areas to be underestimated and consequently, estimation errors within these categories inevitably balanced each other. Similarly, the same applied to water and bare soil where they have been assigned characteristic IS values of 100% or 0%. Consequently, MEs and MAEs for pure pixels of these categories featured equal absolute values (see TABLE D-5).

[2] Global statistics of the wxbx model are incommensurable to those of the remaining models

IS estimations amongst b*are soil* areas, showed different degrees of accuracy depending on the model applied (see TABLE 6-4). The highest deviations occurred with an MAE of ~50% when bare soil was regarded as unsealed (B0), whilst the modelled average IS estimations were with 80% imperviousness much closer to the input values, when assigning *bare soil* a maximum input value of 100% imperviousness (B1). An intermediate input value of 50% imperviousness for bare soil areas (B05), in turn resulted in modelled output values just below 70%. Consequently, the spectral influence of *vegetation* on *bare soil* was less pronounced than that of *sealed surface,* which could be ascribed to a closer spectral resemblance of the latter two categories (see FIG. 6-6). When *bare soil* was excluded from the training procedure (Bx), these areas had average IS values of ~54%, which closely corresponded to the modelled output value of the B0[3] models.

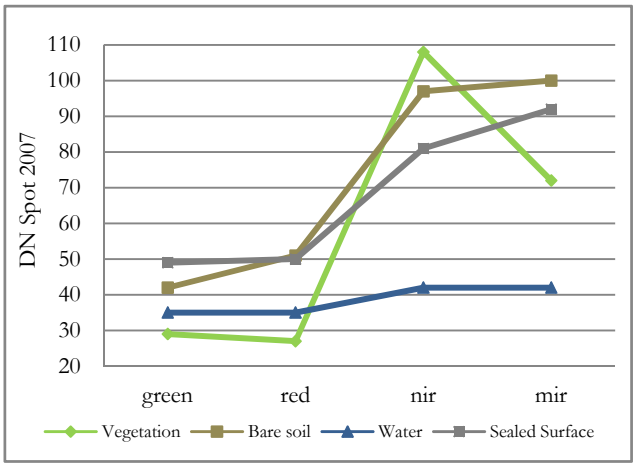

Fig. 6-6: Average reflectance of SPOT training pixels for the derived land cover classes

In addition, a clear trend towards lower levels of accuracy for mixed pixels could be recognized when compared to those from pure land-cover classes (apart from *bare soil*). The MAE of mixed pixels, dominated by vegetation or sealed surfaces, were with ~15% and ~17% up to five times higher, compared to those of the respective pure pixels (see TABLE 6-4). The general lower degree of accuracy of mixed pixels could be attributed to the fact that these were under-represented in the training data, compared to pure pixels. Mixed pixels dominated by *bare soil* however had MAEs equal or lower to those of the corresponding pure pixels. A simple explanation for this is provided by the vegetation-impervious surface-soil (V-I-S) model mentioned in CHAPTER 1.2 (see FIG. 1-3). V*egetation* featured the highest absolute accuracy for the pure land-cover categories and in contrast *bare soil* the lowest. Consequently, it can be assumed that the level of accuracy of a mixed pixel dominated by *vegetation* has to decrease, while in the case of a mixed pixel dominated

[3] B0 model/map: W1B0, W0B0 W1 model/map: W1B1, W1B0
B1 model/map: W1B1, W0B1 W0 model/map: W0B1, W0B0

by *bare soil*, the accuracy level inevitably has to increase with increasing proportions of the other fractions.

When examining estimation performance according to the different models, the variations of the characteristic IS values of *water* areas and *bare soil*, also had effects on the impervious surface estimation for sealed surfaces and vegetation. Those models treating *water* and/or *bare soil* as an impervious entity resulted in output values which were of higher accuracy for sealed areas and of lower accuracy for vegetated areas, in comparison to those models where *water* and/or *bare soil* was regarded as unsealed (TABLE 6-4). Thereby, the influences of water and bare soil can be seen to be more or less independent of each other. This means, when varying the characteristic IS input value of *bare soil,* the specific IS characteristic of *water* had no influence on the classification performance for *vegetated* and *sealed surfaces*.

Table 6-4: Absolute mean error according to model, land-cover class and pixel type

	PURE PIXELS				MIXED PIXELS			
model	**Veg.**	**sealed**	**water**	**bare soil**	**Veg.**	**sealed**	**water**	**bare soil**
W0b0	0,03	0,1	0,04	0,48	0,15	0,17	0,23	0,32
W0b05	0,04	0,08	0,04	0,17	0,15	0,16	0,24	0,16
W0b1	0,05	0,07	0,04	0,2	0,16	0,15	0,24	0,21
W1b0	0,04	0,08	0,08	0,5	0,15	0,15	0,21	0,33
W1b05	0,05	0,07	0,09	0,18	0,16	0,14	0,21	0,17
W1b1	0,06	0,05	0,07	0,2	0,17	0,13	0,21	0,21
Wxbx	0,04	0,06	-	-	-	-	-	-
Area	0,52	0,31	0,15	0,02	0,42	0,44	0,07	0,07

6.4 Impervious surface maps

In the following chapter, the impervious surface maps generated by the different models are evaluated. FIG. 6-7 and FIG. 6-8 show the impervious surface maps of 2009 and 2005, generated with the W0B0 model. It is apparent that errors of omission and commission which occurred in the settlement masks, consequently also manifested themselves in the modelled impervious surface maps. Hence, these errors are not elucidated here as they have already been referred to in CHAPTER 6.1

Impervious surface predictions for 2009 and 2005, with some exceptions, resembled the spatial pattern of the prevailing settlement structures. The highest values were predicted for the very densely built-up centre of the city and were comparatively low for the newly developed, residential districts located in the fringe areas. Open spaces in the urban landscape covered by barren land or bare soil were mapped as low to middle imperviousness, while vegetated areas were characterised by almost 0% imperviousness.

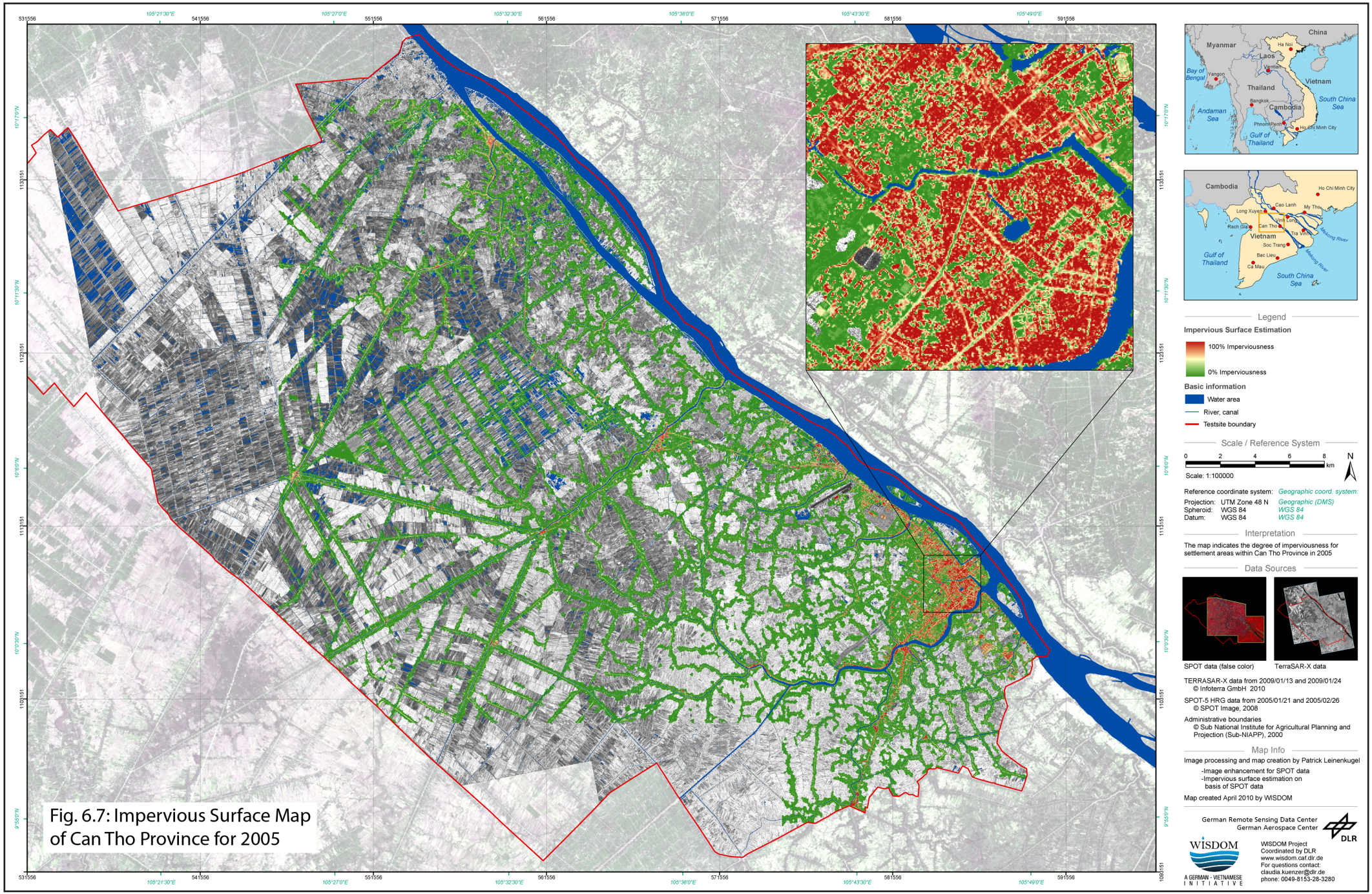

Fig. 6.7: Impervious Surface Map of Can Tho Province for 2005

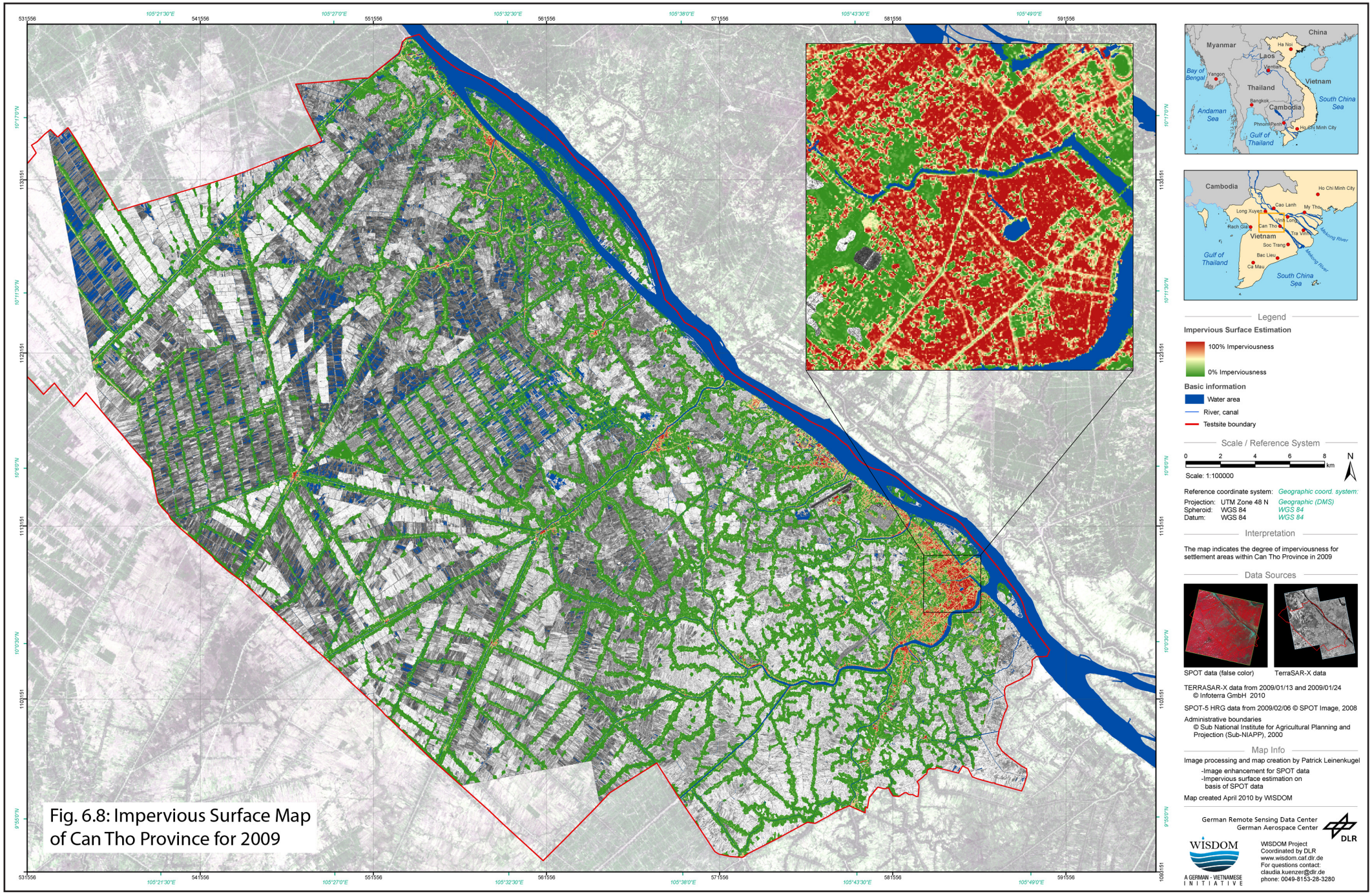

Fig. 6.8: Impervious Surface Map of Can Tho Province for 2009

When examining the individual built-up elements, most of the rooftops were accurately predicted with levels of imperviousness not falling below 95%. In the maps generated by B0 models however, rooftops made of clay bricks were estimated to almost 0% imperviousness and were therefore not identifiable. IS prediction for these rooftops improved significantly when using B1 models, as can be seen in BOX A and BOX B in FIG. 6-9. On the other hand, in B1 maps *bare soil* areas were characterized by very high IS values, as can be seen in BOX C of FIG. 6-9, which made it difficult to distinguish *bare soil* from artificial ground cover materials, such as concrete, tar, or buildings.

A further obvious distortion of actual IS degrees could be found amongst the street network, which was systematically underestimated, particularly in the maps derived from W0 models where they only reached values of ~10% imperviousness (see FIG. 6-10a). These false estimations could be partly accounted for by the spectral proximity of asphalt to water, which both feature spectra with relatively low reflectance values over all bands. Consequently, IS estimations were significantly higher reaching average values of ~60% imperviousness in maps generated by W1 models (see FIG. 6-10b and c). On the other hand, in W1 maps the above mentioned roof tops made of clay bricks were characterised by significantly lower IS estimates, which can be recognised in (see FIG. 6-10b), by the bluish areas in the lower left corner.

Furthermore, it could be observed that modelled degrees of imperviousness within built-up areas varied between the individual dates, though no land-cover change had occurred on the ground. Average imperviousness in 2005-02-26 for example, was about 20-30% lower than in 2005-01-21 but peaks of up to 50% were also observed. FIG. 6-11 shows composites of the two 2005 SPOT scenes (2005-01-21 and 2005-02-26) and of the corresponding modelled IS estimates. As can be seen, discrepancies in both spectral reflectance (a) and IS estimation (b) are clearly apparent.

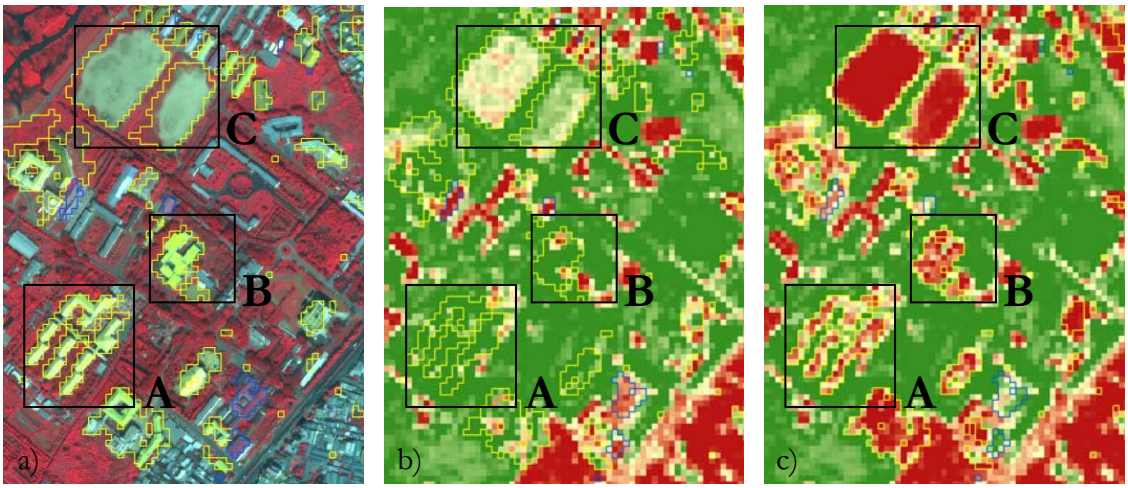

Fig. 6-9: QB subset a); corresponding IS map derived from w0b0 b); and the same subset derived from w0b1 model c); differences between the maps are marked in yellow

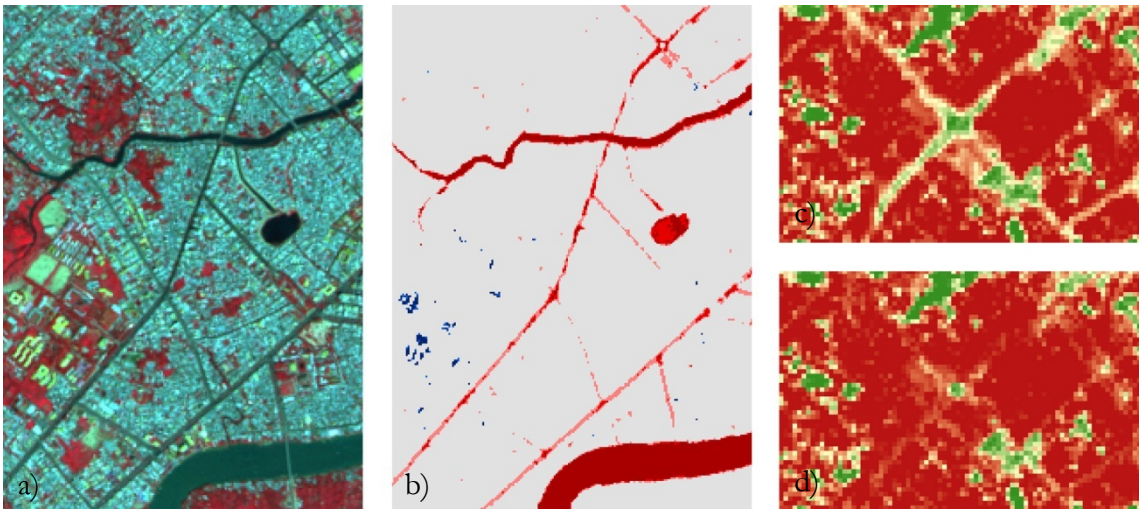

Fig. 6-10: Spot subset a); Increases (red) and decreases (blue) in IS values between maps derived from w0b1 and w0b0 b); IS estimations at a road crossing generated with w0b0 c) and w1b0 d)

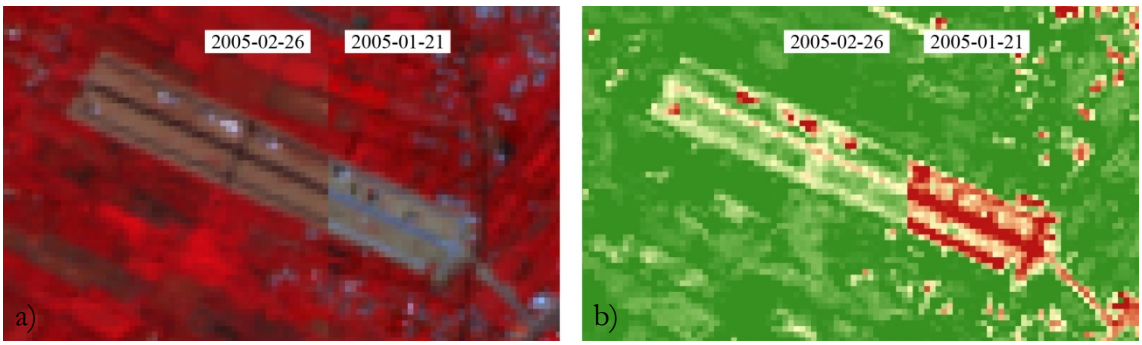

Fig. 6-11: Radiometric variations illustrated by a SPOT composite of 2005 a); corresponding variations in IS estimation due to spectral differences in the SPOT scenes

6.4.1 Ground Truth Validation Results

An attempt to provide an absolute validation was made by comparing the modelled IS values with the respective IS estimations derived from a visual evaluation of 185 ground truth photographs. Altogether, 26 of the 185 sample points differed in their degrees of imperviousness, resulting statistically in an overall accuracy of 86%. However, such accuracy measures feign a false precision of the results, since they were derived on the basis of subjective estimations and not by empirically valid in-situ measurements. Consequently, instead of drawing conclusions from statistically derived accuracy parameters, the results were used to detect the main and most typical sources of errors and trends.

It was remarkable that of the 26 wrongly classified sample points, only four were characterised by higher degrees of imperviousness in the derived map of 2009 than were actually assessed on the ground (see TABLE 6-5). The remaining 22 errors in contrast, were entirely attributable to lower degrees in the impervious surface map. All four cases of IS overestimations arose from cultivated land with pervious ground cover, which however showed high to middle levels of imperviousness in the modelled results. The remaining 22 underestimations of the actual IS conditions could be attributed to distortions resulting from the aerial view of remotely sensed image data: in contrast to microwave radiation, the EMR within the range of the short infrared spectrum or visible light is not capable of penetrating solid materials and thus, cannot reveal surface features hidden under the vegetation canopy. Consequently, treetops and other plants covering actual impervious ground cover implied a systematic underestimation of impervious surface areas. This was especially evident in the less populated settlements located in the rural parts of the study area, which are characterised by a predominantly natural environment, interspersed by small roads, pathways, and single-storey dwellings.

Table 6-5: Error Matrix of ground truth validation

		REFERENCE DATA					CLASSIFIED TOTALS
		unsealed	rather unsealed	balanced	rather sealed	sealed	
Classified Data	unsealed	111	7	2	1	1	122
	rather unsealed	2	7	4	0	0	13
	balanced	1	0	11	5	0	17
	rather sealed	0	0	0	6	2	8
	sealed	0	0	0	1	24	25
Reference totals		114	14	17	13	27	185

6.5 Change Detection

In CHAPTER 0, a change detection analysis was carried out on the basis of the modelled IS estimates of 2005 and 2009. FIG. 6-12 provides a spatial detail of the results and five further subsets are provided in ANNEX B. The upper and middle rows show the original SPOT scenes of 2005 (a) and 2009 (c), together with the corresponding modelled IS estimates (b and d). The lower row presents the change detection results comprising the initial difference image (e) with changes in a continuous range (-100% to +100%), as well as the results of the change classification (f) showing only areas of significant change (>30% difference, >300m² absolute size).

The examples were generated with the w0b05 model on the basis of the unmasked satellite images. Although the settlement mask fulfilled its purpose in excluding extensive, irrelevant areas of change attributable to different crop or flooding conditions between the two recording dates, also a lot of important areas for the change detection analysis were erroneously masked out. Especially dynamic areas designated for building development were incorrectly identified as non-settlement areas (see CHAPTER 6.1). In order to illustrate these errors, the examples are not restricted to the derived settlement areas. Instead non-settlement areas are indicated, having a darker background value in the change classification image (f).

Increases and decreases of imperviousness in this study generally can be attributed to different land-cover transformations which are categorised as follows:

- *vegetated* areas to *bare soil* areas
- *vegetated* areas to *sealed* surfaces
- *bare soil* areas to *sealed* surfaces

} Land transformations resulting in an *increase of imperviousness*

- *bare soil* areas to *vegetated* areas
- *sealed* surfaces to *bare soil* areas
- *sealed* surfaces to *vegetated* areas

} Land transformations resulting in a *decrease of imperviousness*

It can be assumed that demolition of urban features only occurred marginally within the timeframe investigated. Consequently, decreases in IS estimates attributable to land-cover changes from sealed surfaces to bare soil or to vegetated areas, could not be identified in the study area. All other categories mentioned above were present in the study area and were covered by the examples, elucidated as follows:

Land-cover changes from vegetated areas to sealed surfaces ideally result in increases from a minimum to a maximum value of 0% to 100% imperviousness and thus, constitute the most distinct changes in the analysis. Consequently, increases attributable to this category were in most cases correctly and reliably identified, such as new infrastructure developments (A) or building constructions (B) as shown in FIG. 6-12 as well as in FIG. B-5 or FIG. B-3 in ANNEX B. The only exceptions not identified were newly-built clay brick rooftops in the case when B0 models were applied (see CHAPTER 6.4), such as seen in FIG. B-6

Land cover changes from vegetated to bare soil areas also resulted in pronounced IS increases between 50% and 80% dependent on the model applied. Generally, these changes could be attributed to bare soil areas related to new construction activities (C) recently completed, or which were still in progress, as can be observed from FIG. 6-12 as well as from FIG. B-2 or FIG. B-4 in ANNEX B. Distinctions to increases attributable to sealed surfaces however, only were possible when using B0 models.

Land-cover changes from bare soil areas to sealed surfaces resulted in increases of imperviousness between 20% to maximal 50%, dependent on the model applied. Consequently, changes in this category could only be recognized at a rudimentary level from the continuous difference image (e), such as seen in FIG. B-2 or FIG. B-4 in ANNEX B. As significant changes had to show a difference in imperviousness exceeding 30%, these areas of transformation were not detectable as significant changes when using B1 models, as these only resulted in a 20% difference.

Decreases in IS estimates caused by land-cover changes from bare soil to vegetated areas were detected with high accuracy and were the reason for most of the IS reductions in the study area. These changes could be attributed to bare soil areas related to construction activities in 2005 which were overgrown in 2009, clearly recognizable in the boxes D and E of FIG. 6-12 as well as in FIG. B-1, FIG. B-2, or FIG. B-4 in ANNEX B. In some cases decreases in percent IS also occurred in relation to the radiometric discrepancies between the original SPOT images (see CHAPTER 6.4), evident in the upper right and lower left corner of FIG. B-4.

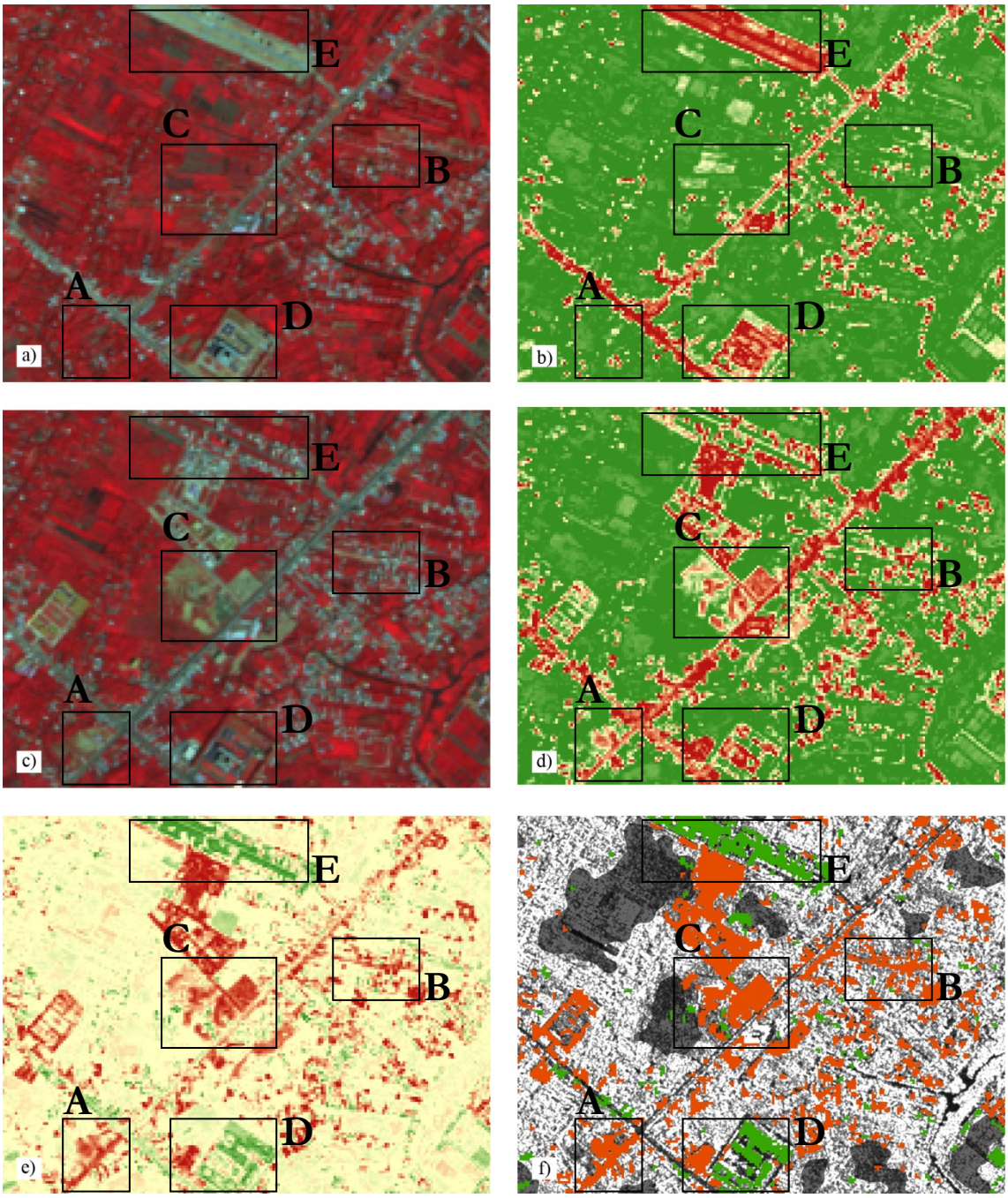

Fig. 6-12: Spot image 2005 a); IS map 2005 b); Spot Image 2009 c); IS map 2009 d); IS difference image 2005-2009 (red: IS increase, green: IS decrease) e); Change map 2005-2009 (red: IS increase, green: IS decrease, black: non-settlement areas) f)

6.6 IS statistics per commune

In CHAPTER 5.5, IS estimations of 2005 and 2009 as well as the changes in impervious surface area for this period, were spatially-aggregated to the administrative units of communes. Average IS estimations ranged from very low values below 5% to peak values reaching up to 80%. Thereby, the dispersion was rather skewed with three quarters of the communes

showing only marginal differences featuring averages from 3% to 10% imperviousness, while the remaining communes had averages varying from 10% to 80% (see FIG. 6-13). Detailed statistics for all communes can be taken from TABLE C-1 in ANNEX C.

The spatial pattern of the prevailing settlement structures for 2005 and 2009 can be observed from displaying the calculated averages in a thematic map (FIG. 6-14a,b), divided into seven classes according to a natural breaks classification (JENKS and CASPALL 1971). High proportions of impervious surface cover could be noticed in the north- and south-eastern part of the province, where the cities *Thot Not* and *Can Tho* are located. Comparatively low averages could be observed in the remaining, predominantly rural areas in the western parts of the province. By far the highest rates were predicted in the very densely populated communes in the centre of *Can Tho* City, while the surrounding communes characterised by suburban residential areas, featured high to medium values, which tended to lessen with increasing distance from the centre. It was also notable that some communes in the hinterland reached medium averages on account of larger settlements like *Co Do* or *Thoi Lai,* located at strategic interconnection points.

On examination and comparison of the detailed values obtained for 2005 and 2009, a clear trend towards higher IS averages in 2009 could not be observed. In fact, some communes in 2009 showed an opposite development with averages which were about 1-3% lower than in 2005. These could be primarily attributed to the previously mentioned, radiometric discrepancies between the original satellite images.

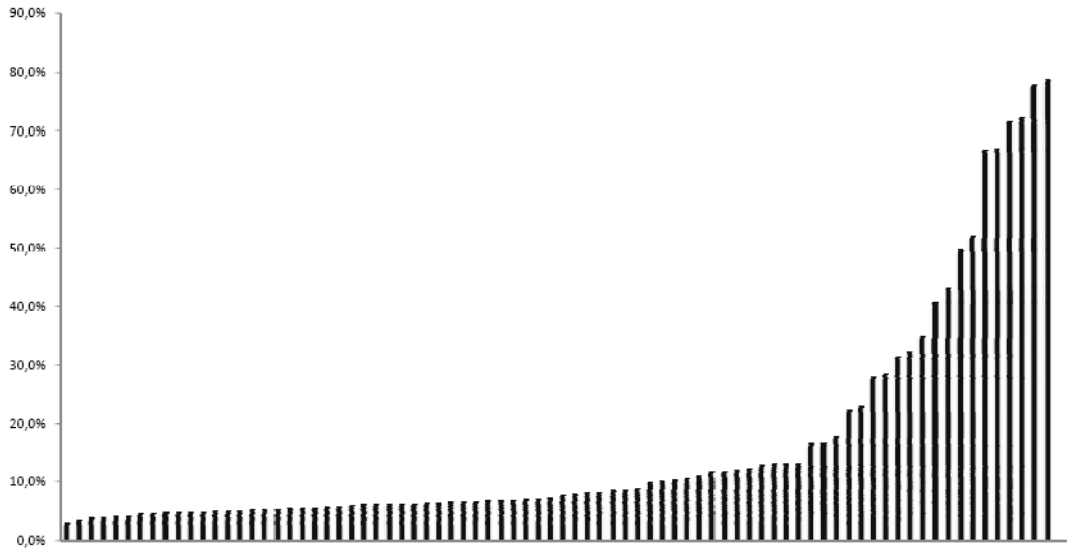

Fig. 6-13: Average IS estimates pro commune derived from the IS map 2009

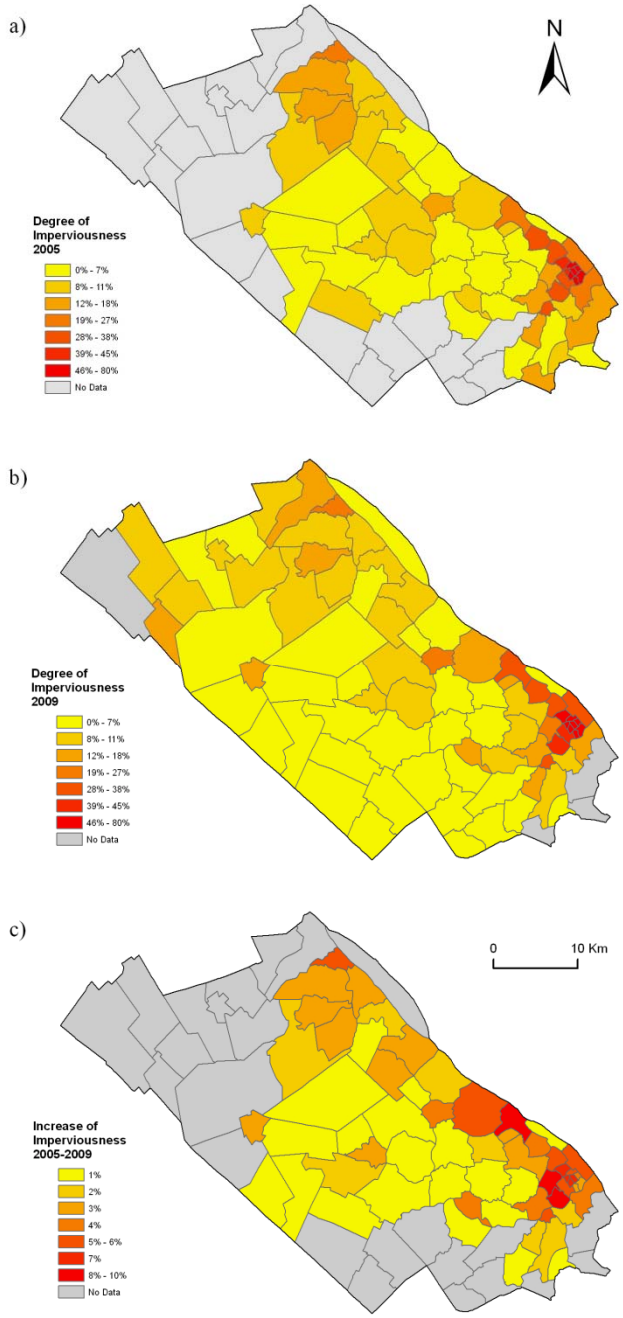

Fig. 6-14: IS statistics per commune for 2005 a) and 2009 b) as well as average increase of impervious cover 2005-2009

Average change in imperviousness shown in FIG. 6-14c, only comprised the significant increases in impervious cover (>30% difference, >300m² absolute size) which were identified in the change detection analysis. In this way, radiometric discrepancies could be diminished and the counterbalance effect of decreases, attributable to overgrown areas of bare soil, could be prevented. Consequently, average changes could solely be attributed to new construction activities and thus, provided a better indicator of urban growth. The map reveals a clear pattern of the construction activities which prevailed within the time period of the study. The highest averages were no longer observed in the centre of Can Tho City, but had shifted to the adjacent northern and western communes. Due to the shortage of space in the central districts indicated by high absolute IS values, construction on open pervious spaces in the centre was hardly possible. This was in contrast to the outer perimeters characterised by lower proportions of impervious cover where enough space was available for new building projects, such as the development of residential areas and infrastructure. Furthermore, the map reveals a lot of construction activities along the western bank of the *Hậu Giang* River, where new port facilities and industrial complexes have emerged. Here, the first signs of a pattern are evident, whereby the two cities *Thot Not* from the north and *Can Tho* City from the south, are gradually merging together to form a continuous line of development along the river.

Chapter 7

Discussion

This work aimed to provide a comprehensive approach for large-area but selective mapping of impervious surface solely based on remotely sensed data sources. Within this context, one of the focal points was *to evaluate the suitability of SAR data for the automated generation of settlement masks, appropriate for defining relevant areas for the impervious surface estimation process.*

The approach for delineating settlements was initially developed for urban agglomerations with relatively homogenous settlement structures, the framework conditions however in this work differed significantly. In order to evaluate the approach for large area analyses, the study area included distinctly different settlement types ranging from a typical urban environment to settlements in rural settings. The contrast in settlement types gave rise to an abundance of differences relating to building height, density and structure, the width of intermediary transition zones to non-settlement areas, as well as the distribution of vegetation and water surfaces within the built environment. These environmental characteristics have a direct impact on the radar return signals including the occurrence and frequency of corner reflectors and the development of texture. In light of this, a main challenge related to the process of settlement delineation was the adjustment of the classification rules, so that thresholds were appropriate for the contrasting settlement types. When adjusting the texture thresholds and the search radii (for extending DBCs and identifying UA) to fit the denser and compacter urban environments, featuring more pronounced textures and higher concentrations of corner reflectors, many rural settlements especially those not located at channels were omitted. Conversely, the adjustment of the parameters to include also those settlement areas having weaker texture and lower building densities led to an unnecessarily generous settlement inclusion, when applied to the denser urban environments. Consequently, the classification represents a compromise between identifying as

many settlement areas as possible and attaining the level of accuracy with which the actual built environment is delineated. Laying priority on either the first or the second argument significantly influences average IS estimations, as increased focus on the first argument, implies greater proportions of pervious ground cover included in the settlement area.

In rural areas, over identification of settlements arose due to the frequent presence of water features which constituted the main source of commission error in this study. The gravity of this error could be explained by the particular hydrologic character of Can Tho Province with its numerous channels and aquaculture ponds, though this issue may not be relevant for other study areas. A major issue occurring in the denser urban environment, was the omission of extensive settlement areas lacking sufficient height variations, which were subsequently ignored in the IS estimation process. If these areas were relatively small, reintegration into the settlement body could easily take place. However, larger areas such as those undergoing development as shown in Fig. 6-2, were regarded as open land and could not be reintegrated and thus remained as non-settlement areas. Although these omitted areas often feature high proportions of impervious surfaces, they only marginally affect average statistics in large area analyses; as such errors are usually limited to a small number of restricted locations. In the context of change detection analyses however, the omission of developing areas is more severe, as these areas are highly dynamic with great potential for change. A further consideration is the omission of a large proportion of the street network, a factor which should not be ignored: as dense networks of overland routes may occur around agglomerations, the exclusion of transport routes in the IS estimation process can significantly influence average statistics.

The high variations in accuracy according to the applied settlement definition, demonstrates the high dependency of validation results on the underlying reference, as well as the necessity for using clear-cut rules when dealing with ambiguous and broad concepts such as that of *settlement*. Consequently, the qualification of the derived settlement masks for impervious surface estimation can only be evaluated in relation to the required measure of scale. When aiming at the extraction of actual built-up structures such as individual buildings or roads, the settlement footprint derived from the approach in this study is of only limited use, as insufficient classification reliability (user's accuracy of only 57% for S25) was reached. Large-area impervious surface estimation however requires a more comprehensive settlement definition encompassing the immediate living environment of the inhabitants, which includes any land-cover related to residential, commercial or industrial usage. In this respect, the broader settlement definitions S50-S100 fulfilled these requirements more ade-

quately, on the basis of which the derived settlement masks showed high levels of producer's and user's accuracy over 75%.

A further focal point concerned *the degree of precision obtainable when applying the SVR concept to SPOT HRG data*. The use of variable training datasets showed that accuracy could only be increased for individual land-cover categories or different fractions of the pixels. There was no model which resulted in a win-win situation, where accuracy for both pixels with high proportions (dominated by sealed surface) and low proportions (dominated by vegetation) of impervious surfaces would improve. Although differences only varied statistically on a low level, the inspection of the impervious surface maps revealed locally restricted, but significant changes in IS estimations, depending on the model applied. The assignment of water to the impervious class significantly increased the accuracy of the road network compared to the remaining models. Bare soil designated "impervious" generally resulted in higher estimations and thus provided better representations of built-up structures, being especially evident for buildings with clay-brick rooftops. These improvements however, only slightly affected the statistical results, as roads and clay-brick rooftops only constituted small proportions in the validation area. However, these improvements in accuracy were also accompanied by negative effects as listed in TABLE 7-1. Consequently, no clear recommendation for a specific model can be made. Instead, the choice of an appropriate model depends on the respective focus of interest and priority.

Table 7-1: Effects of model application

MODELS	PRO	CONTRA
W1	Significantly increases IS values of the street-network	Water related areas (e.g. ponds) are classified as sealed surfaces requiring a very accurate water mask Decreases accuracy of clay brick rooftops
B1	Significantly increases IS values of clay brick rooftops	Bare soil areas feature high IS estimations and thus are hardly distinguishable from built-up structures

Some errors which occurred in connection with IS estimation in this work are well known issues as seen by examining comparable studies. The validation based on ground truth data indicated a systematic underestimation in impervious surface, which could be attributed to tree crowns and bushes obscuring the actual ground. This distortion has been observed in numerous studies (XIAN 2007, WENG 2007, LU and WENG 2007) and arises from the fact that IS estimation is solely defined as a function of surface cover. BAUER ET AL.(2007), estimated this effect as being responsible for an error of less than 6% within an urban setting with varying amounts of tree cover. It can be assumed however, that these effects were more severe in rural settings in the north and west, where vegetation is more prevalent and tree cover denser. Furthermore, a well known problem is the confusion of bare soil with

tarred surfaces on account of their spectral proximity (BAUER et al. 2007, ESCH et al. 2009, WENG 2007). Although the settlement masks excluded most of the bare soil areas, some remained within the settlements and were often misclassified as impervious. Especially in rural areas these assignments did not represent the true conditions on the ground where usually less compacted soil is present. The influence of bare soil could be diminished by using B0 models. Nevertheless, these distortions still remained problematic. In contrast, the well documented phenomena of seasonal influences on the resulting impervious surface estimation were not relevant to this study. This factor could be dismissed as all images were recorded in January and February and additionally, the seasonal variability of the plant phenology (leaf-on/leaf-off) is in any case, relatively weak in low-latitudes compared to middle or high-latitudes.

Table 7-2: Mean absolute error obtained by Esch et al. (2009) compared to the results in this study.

CLASSES	MEAN ABSOLUT ERROR (MAE)				
	Passau	Leipzig	Ludwigshafen	Can Tho W1B1	Can Tho W0B0
0–10	15%	18%	26%	7%	6%
10–20	14%	19%	18%	17%	17%
20–30	13%	18%	17%	18%	20%
30–40	13%	17%	16%	18%	17%
40–50	13%	16%	17%	18%	15%
50–60	14%	16%	19%	17%	16%
60–70	15%	17%	22%	17%	16%
70–80	17%	19%	26%	14%	17%
80–90	16%	21%	29%	14%	18%
90–100	13%	25%	31%	7%	10%

ESCH et al. (2009), applied the SVR approach to Landsat ETM+ data comprising a spectral resolution of seven bands (including a thermal infrared band highly valuable for differentiating between impervious surface and vegetation) and a spatial resolution of 30*30 m. Accuracy was assessed by comparing the modelled IS estimates with reference data according to a ten-class classification scheme (see TABLE 7-2). When applying the same scheme, accuracy obtained in this work showed comparable results with MAEs of between 10% and 20%, but featured a different distribution over the classes. It was evident that the accuracy of this work was higher for low and high estimates (0-10%, 70-100%), and lower for the intermediate IS classes (20-70%), compared to the best results obtained from ESCH et al. (2009). This can be explained by the fact that the training data in this work, with pixel sizes of 10*10m, featured high numbers of pure pixels, whilst mixed pixels were generally underrepresented. It can be assumed that training data with pixel sizes of 30*30 m in contrast, are characterised by higher proportions of mixed pixels, resulting in a sound training basis

for intermediate IS estimations. It can be assumed though that with increasing pixel sizes, the level of accuracy of the high and low IS estimates (pure pixels) and of the intermediate estimates (mixed pixels) will converge.

The last focal point concentrated on the *testing of a change detection method to evaluate the approach for a continuous large-area monitoring of developments in IS cover*. In this context, a major prerequisite is that the level of imperviousness for unchanged ground cover remains consistent over time. The results showed however that in some cases, IS values varied significantly from map to map for the same feature on the ground, which could be traced back to the reflectance properties of the original satellite images. Although intensive measures were taken to reduce the radiometric discrepancies between the original images, it became apparent that the spectral differences were still too high and thus, not satisfactory. These irregularities could result from the different viewing angles from which the images were recorded. It is evident that different viewing angles of the sensor result in varying incidence angles on the ground and viewing azimuths, which in turn result in altered reflectance properties for each scene. These differences can actually be reduced by atmospheric correction, though high variations between the scenes can still remain, as can be seen in this study. The SPOT image recorded in January 2005 for instance, was acquired from the right side of the flight track, which resulted in an incidence angle of -1.33° and a viewing azimuth of 102°. The SPOT image from February 2005 in contrast, was acquired from the left side resulting in a significantly different incidence angle of 10.88° and a view azimuth of 282°. These different recording conditions especially influenced the reflectance over built-up areas which in turn, directly affected the estimation of imperviousness. FIG. 7-1 shows average discrepancies of IS estimations for each commune within the overlapping area of the two 2005 SPOT images. As the time difference was only one month, differences in IS estimations hardly resulted from land-cover changes on the ground. It is apparent that as the proportions of built-up areas increased within the communes average deviations also rose, reaching maximum values up to 8%.

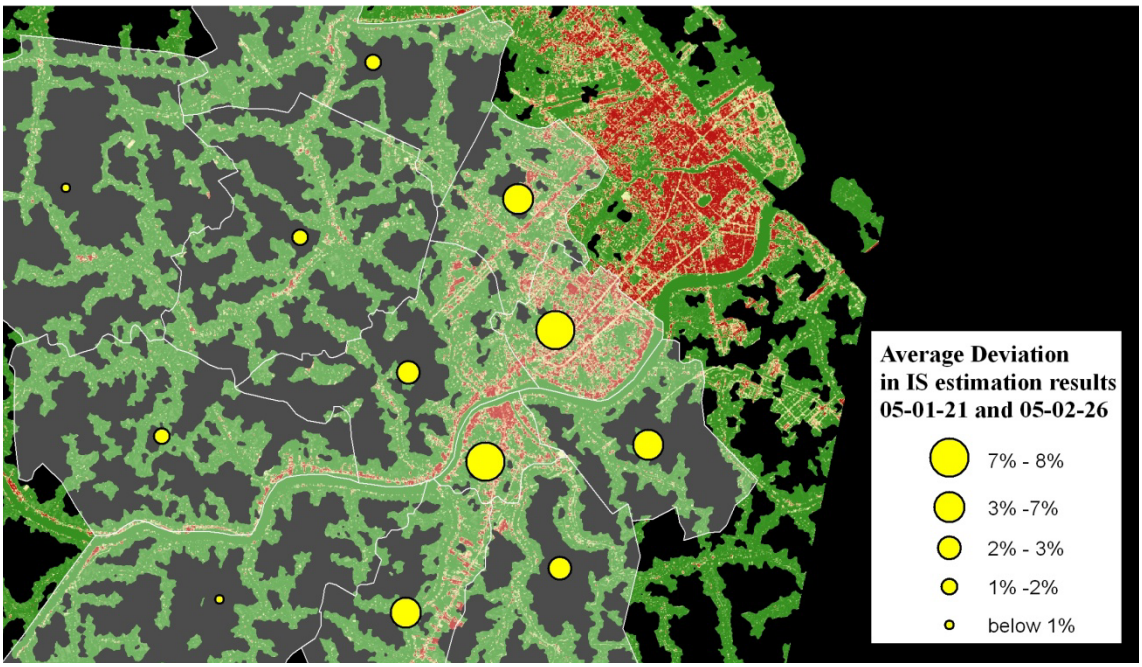

Fig. 7-1: Average deviations in IS estimation results

If a continuous monitoring of impervious surface, for example on a year to year basis, is to be useful, fluctuations in IS estimations due to radiometric discrepancies (in this case up to 50%) have to be significantly smaller than IS variation attributable to real land-cover changes. With a spatial resolution of 10*10m, newly built structures on the land surface resulted in high changes in imperviousness of up to 100% and thus, local changes in imperviousness related to construction activities could be extracted with high accuracy. With larger pixel sizes however, such changes only constitute a small proportion within the extent of the pixel (mixed pixels) and consequently related IS cover changes become negligible in relation to the radiometric fluctuations. This was especially apparent when comparing the statistical average values derived from spatial aggregation. In many communes, average values of 2009 were lower than in 2005. Impervious surfaces estimation for the whole settlement area of Can Tho Province constituted 16.6 % in 2005 and 16.4% in 2009, in spite of the obvious increase in land development. These results demonstrate that a strict radiometric standardisation of the satellite data by means of an accurate atmospheric correction and by a specific histogram matching is absolutely essential.

Chapter 8

Outlook

As mentioned above, rural and urban settlements are characterised by different spatial patterns, which are especially evident in the various density of building structures. Consequently, by applying uniform texture values and search radii, thresholds had to be chosen to compromise between rural and urban areas. Therefore, with respect to settlement delineation further research could be continued to develop adaptable classification rules, which automatically adjust to fit the prevailing settlement structure within a specific local environment. By using the standard distance deviation calculated for the DBCs in an initially larger neighbourhood (A in FIG. 8-1), the diameter for the actual search radii of the region-growing procedure (PUS and UA) could be adjusted to the local pattern of building density.

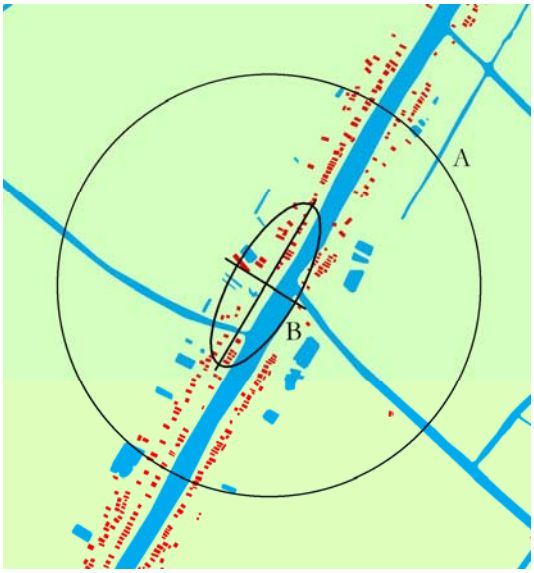

Fig. 8-1: A representation of geometric anisotropy in which the ellipse describes the characteristic distributions of settlements in two dimensions

Furthermore, the main direction of the spatial pattern could be incorporated. As buildings generally follow some linear arrangement (due to roads), they are spatially distributed in a predictable manner in distance and direction. To account for these skewed distributions, application of the standard deviational ellipse (B in FIG. 8-1) as a directional dependent neighbourhood would be more appropriate, whereby the superfluous space occurring in a circular neighbourhood would be minimised (WEBSTER and OLIVER 2007). By applying

these adaptations, texture thresholds may be relaxed so that more settlement areas could be included whilst simultaneously built-up structures could be delineated with higher accuracy.

A further potential research field could focus on the image fusion of optical and TSX radar data in order to provide a combined application data basis which can result in additional information complementary to that gained from optical data. Firstly, efforts could be undertaken to investigate whether accuracy for settlement detection can be improved by using the additional information obtained from optical spectra (inclusion streets and building land). Secondly, by using the microwave backscatter supplementary to the optical spectral information for impervious surface estimation, the well-known spectral confusion between certain land-cover types, such as barren land and tarred surfaces (BAUER et al. 2007) could be addressed. JIANG et al. (2009) tested this approach for InSAR and SPOT imagery for impervious surface calculation and achieved significant improvements for the separation of urban impervious surface from the vacant land/bare ground compared to the use of SPOT imagery alone.

Chapter 9

Conclusion

This work focused on large-area impervious surface mapping by using multi-source remote sensing datasets. On the basis of TSX SAR data, settlements were detected as relevant areas for a SVR-based IS estimation approach, which was applied to SPOT HRG imagery.

The study focused on Can Tho Province, Vietnam, comprising an area of about 1500 km² whereby spatially detailed information on the characteristics and distribution of IS was generated for settlement areas only, which make up approximately 450 km² or ~30% of the whole area. Furthermore, the results were spatially-aggregated according to the administrative units of communes. For the year 2009, it could be shown that ~16.4 % of the settlement areas in Can Tho Province were covered by impervious surface. Proportions of impervious surface differed significantly from commune to commune ranging from less than 3% imperviousness in the rural northern and western areas of the province to more than 80% imperviousness in the densely built centre of Can Tho City.

High levels of user's and producer's accuracy demonstrated that the approach applied for settlement detection has potential as a basis for impervious surface calculation. This implies however that the concept 'settlement' is broadly understood as the direct living environment of its citizens and not restricted to built-up structures only. An equivalent substitute to AKTIS vector data, cannot however be fulfilled by this approach, as the derived masks are unable to delineate the settlements with the same degree of precision. Since the capacity to accurately delineate settlements is dependent on the building density and structure, a higher level of accuracy may be attained by implementing relative parameterisation in place of absolute thresholds. Furthermore, the omission of developing areas and overland roads

constitute a substantial disadvantage compared to AKTIS vector data, which encompasses not only prospective building land but also lineal elements of infrastructure.

The IS estimation results demonstrated that Spot HRG data, with only four spectral bands, provides levels of accuracy comparable to those obtained from Landsat ETM+ data, featuring seven spectral bands. In addition, the application of different training data showed that the IS characteristic of water and bare soil could have strong local influences on the IS estimations of sealed surfaces such as on the street network or on certain rooftop types. These influences however, showed only lower statistical significance in relation to the maps as a whole.

The resulting IS estimates are strongly dependent on the reflectance properties of the original satellite images. Slight radiometric discrepancies between the original scenes therefore can significantly distort the actual conditions, which become more severe with increasing pixel size of the application data. In this respect, the suitability of the approach for a continuous large-area monitoring of IS cover is questionable. Although constructional changes were detected with high accuracy using HRG data, radiometric differences caused implausible results for the comparison of IS averages on the level of administrative units. In light of this, a regular monitoring of impervious surface on the basis of middle to low resolution data (pixel sizes of > 30m) will only provide reliable results when a more enhanced and accurate radiometric correction and histogram matching is applied. Consequently, in addition to the above mentioned prospective research topics further effort has to be undertaken to provide a suitable and effective method of atmospheric correction and radiometric normalisation in the course of the preprocessing.

Although average IS values for most communes in the province are still very low, an enormous dynamic urban development could be observed. It could be shown that construction activities particularly are concentrated along the Mekong and in the provinces surrounding Can Tho City. In view of the rate of development, early and sustainable urban planning would in the long term contribute to improving the quality of living and environmental conditions in this expanding and dynamic region. Information about the degree of imperviousness and its recent development in the area may be a first step towards this goal.

Annex A

Bibliography

A

Adams, J. B. & A. R. Gillespie (2005). Remote sensing of landscapes with spectral images: a physical modelling approach. Cambridge. Cambridge University Press.

Allen, J., V. Patki & A. Pasula (2007). Impervious Cover Analysis for the Saluda-Reedy Watershed in Upstate South Carolina. South Carolina Water Resources Center (SCWRC).

Arnold, C. L. & C. J. Gibbons (1996). Impervious Surface Coverage: The Emergence of a Key Environmental Indicator. In: Journal of the American Planning Association, 62**,** 243 - 258.

B

Baatz, M. & A. Schäpe (2000). Multiresolution Segmentation – an optimization approach for high quality multi-scale image segmentation. In: Angewandte Geographische Informationsverarbeitung XII, eds. J. Strobl, T. Blaschke & G. Griesebner, 12-23. Heidelberg. Herbert Wichmann Verlag.

Bachhofer, F. (2008). Ableitung von Versiegelungsgraden basierend auf hochaufgelösten Fernerkundungsdaten mittels "Support Vector Regression" (Diplomarbeit). Tübingen. Eberhard Karls Universität Tübingen.

Bauer, M., B. Loffelholz & B. Wilson (2007). Estimating and Mapping Impervious Surface Area by Regression Analysis of Landsat Imagery. In: Remote Sensing of Impervious Surfaces. CRC Press.

Berk, A., L. S. Bernstein, G. P. Anderson, P. K. Acharya, D. C. Robertson, J. H. Chetwynd & S. M. Adler-Golden (1998). MODTRAN Cloud and Multiple Scattering Upgrades with Application to AVIRIS - editions of 1991 and 1992. In: Remote Sensing of Environment, 65**,** 367-375.

Blais, T. & J. P. Hermier (1995). High-performance pointing and scanning mechanisms for ATLID and SPOT 5. In: European Space Mechanisms and Tribology Symposium, ed. W. R. Burke, 1-81.

Blaschke, T. (2010). Object based image analysis for remote sensing. In: ISPRS Journal of Photogrammetry and Remote Sensing, 65**,** 2-16.

Blaschke, T. & J. Strobl (2001). What's wrong with pixels? Some recent developments interfacing remote sensing and GIS. In: GIS - Zeitschrift für Geoinformationssysteme, 14**,** 12-17.

Bolay, J.-C., S. Cartoux, A. Cunha, T.-T. N. Du & M. Bassand (1997). Sustainable development and urban growth: Precarious habitat and water management in Ho Chi Minh City, Vietnam. In: Habitat International, 21**,** 185-197.

Brabec, E., S. Schulte & P. L. Richards (2002). Impervious Surfaces and Water Quality: A Review of Current Literature and Its Implications for Watershed Planning. In: Journal of Planning Literature, 16**,** 499-514.

Burges, C. J. C. (1998). A tutorial on support vector machines for pattern recognition. In: Data Mining and Knowledge Discovery, 2**,** 121-167.

C

Cablk, M. E. & T. B. Minor (2003). Detecting and discriminating impervious cover with high-resolution IKONOS data using principal component analysis and morphological operators. In: International Journal of Remote Sensing, 24**,** 4627 - 4645.

Chabaeva, A., J. Hurd & D. Civco (2007). Quantitative Assessment of the Accuracy of Spatial Estimation of Impervious Cover. In: ASPRS Annual Conference Proceedigns 2007. Tampa, Florida.

Chih-Chung, C. & L. Chih-Jen (2010). LIBSVM: a Library for Support Vector Machines. Available URL: http://www.csie.ntu.edu.tw/~cjlin/libsvm (accessed 14 June, 2010).

Chih-Wei, H., C. Chih-Chung & L. Chih-Jen (2008). A Practical Guide to Support Vector Classification. Taipei, Taiwan.

Congalton, R. G. (1991). A review of assessing the accuracy of classifications of remotely sensed data. In: Remote Sensing of Environment, 37**,** 35-46.

Congalton, R. G. & K. Green (2009). Assessing the accuracy of remotely sensed data principles and practices. Boca Raton. CRC Press/Taylor & Francis.

Cristianini, N. & J. Shawe-Taylor (2000). An Introduction to Support Vector Machines and Other Kernel-based Learning Methods. Cambridge University Press.

D

Definiens (2007). Definiens Developer 7 User Guide. München. Definiens AG.

Dekker, R., C. Kuenzer, I. Niemeyer, V. Lacroix & E. Stinga (2009). Change Detection Tools. In: Remote sensing from space supporting international peace and security, eds. B. Jasani, M. Pesari, S. Schneiderbauer & G. Zeug, 119-140. Dordrecht; London. Springer.

Dougherty, M., R. L. Dymond, S. Goetz, C. A. Jantz & N. Goulet (2004). Evaluation of impervious surface estimates in a rapidly urbanizing watershed. In: Photogrammetric Engineering and Remote Sensing, 70**,** 1275-1284.

E

Esch, T. (2006). Automatisierte Analyse von Siedlungsflächen auf der Basis höchstauflösender Radardaten (Dissertation). Würzburg. Julius-Maximilians Universität Würzburg.

Esch, T., V. Himmler, G. Schorcht, M. Thiel, T. Wehrmann, F. Bachofer, C. Conrad, M. Schmidt & S. Dech (2009). Large-area assessment of impervious surface based on integrated analysis of single-date Landsat-7 images and geospatial vector data. In: Remote Sensing of Environment, 113**,** 1678-1690.

Esch, T., G. Schorcht & M. Thiel (2007). Satellitengestützte Erfassung der Bodenversiegelung in Bayern. Augsburg. Bayerisches Landesamt für Umwelt.

Esch, T., M. Thiel, M. Bock, A. Roth & S. Dech (2008). Improvement of image segmentation accuracy based on multiscale optimization procedure. In: IEEE Geoscience and Remote Sensing Letters, 5**,** 463-467.

Esch, T., M. Thiel, A. Schenk, A. Roth, A. Muller & S. Dech (2010). Delineation of Urban Footprints From TerraSAR-X Data by Analyzing Speckle Characteristics and Intensity Information. In: IEEE Transactions on Geoscience and Remote Sensing, 48**,** 905-916.

Evers, H.-D. & S. Benedikter (2009). Hydraulic bureaucracy in a modern hydraulic society – Strategic group formation in the Mekong delta, Vietnam. In: Water Alternatives, 2**,** 416-439.

F

Foody, G. M. (2002). Status of land cover classification accuracy assessment. In: Remote Sensing of Environment, 80**,** 185-201.

Fritz, T. & M. Eineder (2009). TerraSAR-X Ground Segement Basic Product Specification Document. 1-108. German Aerospace Centre DLR.

Frulla, L. A., J. A. Milovich & D. A. Gagliardini (2000). Automatic computation of speckle standard deviation in SAR images. In: International Journal of Remote Sensing, 21**,** 2883 - 2899.

G

Gillies, R. R., J. Brim Box, J. Symanzik & E. J. Rodemaker (2003). Effects of urbanization on the aquatic fauna of the Line Creek watershed, Atlanta - a satellite perspective. In: Remote Sensing of Environment, 86**,** 411-422.

Goetz, S. & G. Fiske (2008). Linking the diversity and abundance of stream biota to landscapes in the mid-Atlantic USA. In: Remote Sensing of Environment, 112**,** 4075-4085.

Goodman, J. W. (1976). Some fundamental properties of speckle. In: Journal of the Optical Society of America, 66**,** 1145-1150.

Gstaiger, V., S. Gebhardt, J. Huth, T. Wehrmann & C. Kuenzer (2010). Multi-sensoral derivation of inundated areas using TerraSAR-X and ENVISAT ASAR data. In: International Journal of Remote Sensing.

Gualtieri, J. A. & R. F. Cromp (1998). Support Vector Machines for Hyperspectral Remote Sensing Classification, Proceeding of the SPIE. 221–232. SPIE, 1998.

H

Henderson, F. M. & K. A. Mogilski (1987). Urban Land Use Separability as a Function of Radar Polarization. In: International Journal of Remote Sensing, 8**,** 441-448.

Herold, M., N. C. Goldstein & K. C. Clarke (2003). The spatiotemporal form of urban growth: measurement, analysis and modeling. In: Remote Sensing of Environment, 86**,** 286-302.

Himmler, V. (2008). Erhebung von Versiegelungsdaten mittels Fernerkundung und geographischer Informationsverarbeitung (Diplomarbeit). Würzburg. Julius-Maximilians-Universität Würzburg.

Hofmann, P., J. Strobl, T. Blaschke & H. Kux (2008). Detecting informal settlements from QuickBird data in Rio de Janeiro using an object based approach. In: Object-based image analysis spatial concepts for knowledge-driven remote sensing applications, eds. T. Blaschke, S. Lang & G. Hay, 531-553. Berlin. Springer.

Hu, X. & Q. Weng (2009). Estimating impervious surfaces from medium spatial resolution imagery using the self-organizing map and multi-layer perceptron neural networks. In: Remote Sensing of Environment, 113**,** 2089-2102.

Hung, M.-C. & K. Germaine (2008). Delineating Impervious Surface Utilzing High-spatial Resolution Multispectral Imagery And Lidar Data. In: Proceedings of the American Society for Photogrammetry & Remote Sensing (ASPRS) Annual Conference 2008. Portland.

J

Jat, M. K., P. K. Garg & D. Khare (2008). Modelling of urban growth using spatial analysis techniques: a case study of Ajmer city (India). In: International Journal of Remote Sensing, 29**,** 543 - 567.

Jenks, G. F. & F. C. Caspall (1971). Error On Choroplethic Maps: Definition, Measurement, Reduction. In: Annals of the Association of American Geographers, 61**,** 217-244.

Jensen, J. R. (1986). Introductory digital image processing : a remote sensing perspective. New Jersey. Prentice Hall.

Jensen, J. R. (2007). Remote sensing of the environment: an earth resource perspective. New Jersey. Prentice Hall.

Jiang, L., M. Liao, H. Lin & L. Yang (2009). Synergistic use of optical and InSAR data for urban impervious surface mapping: a case study in Hong Kong. In: International Journal of Remote Sensing, 30**,** 2781 - 2796.

K

Kiermaier, S. (2010). Radiometrische Normalisierung und automatisierte Trainingsdatengenerierung als Grundlage zur Landnutzungsklassifikation von Zeitseriendaten (Bachelorthesis). München.

Kuenzer, C. (2005). Demarcating Coal Fire Risk Areas Based on Spectral Test Sequences and Partial Unmixing Using Multi Sensor Remote Sensing Data (Dissertation). Vienna. Technical University Vienna.

Kuenzer, C., T. Wehrmann, S. Gebhardt, M. Schmidt & H. Mehl (2009). A Water Related Information System for the Mekong (Lancang). In: Proceedings of the 6th International Symposium on Digital Earth (ISDE6). Beijing, China.

L

Lee, S. & R. G. Lathrop (2005). Sub-pixel estimation of urban land cover components with linear mixture model analysis and Landsat Thematic Mapper imagery. In: International Journal of Remote Sensing, 26**,** 4885 - 4905.

Li, G. & Q. Weng (2007). Measuring the quality of life in city of Indianapolis by integration of remote sensing and census data. In: International Journal of Remote Sensing, 28**,** 249 - 267.

Lillesand, T. M., R. W. Kiefer & J. W. Chipman (2004). Remote sensing and image interpretation. Hoboken. Wiley.

Liu, J. G. (2000). Smoothing Filter-based Intensity Modulation: a spectral preserve image fusion technique for improving spatial details. In: International Journal of Remote Sensing, 21**,** 3461 - 3472.

Lu, D. & Q. Weng (2006). Use of impervious surface in urban land-use classification. In: Remote Sensing of Environment, 102**,** 146-160.

Lu, D. & Q. Weng (2007). Mapping Urban Impervious Surfaces from Medium and High Spatial Resolution Multispectral Imagery. In: Remote Sensing of Impervious Surfaces. CRC Press.

Lu, D. & Q. Weng (2009). Extraction of urban impervious surfaces from an IKONOS image. In: International Journal of Remote Sensing, 30**,** 1297 - 1311.

Lu, D., Q. Weng & G. Li (2006). Residential population estimation using a remote sensing derived impervious surface approach. In: International Journal of Remote Sensing, 27**,** 3553 - 3570.

Luo, L. & G. Mountrakis (2010). Integrating intermediate inputs from partially classified images within a hybrid classification framework: An impervious surface estimation example. In: Remote Sensing of Environment, 114**,** 1220-1229.

M

Mather, P. M. (2004). Computer processing of remotely sensed images: an introduction. Chichester.

Mather, R. (2009). Wetlands in the Mekong Basin. In: Asian Water**,** 19-22.

Meinel, G., I. Schubert, S. Siedentop & M. F. Buchroithner (2007). Europäische Siedlungsstrukturvergleiche auf Basis von Corine Land Cover - Möglichkeiten und Grenzen. In: REAL CORP 2007, Proceedings, eds. M. Schrenk, V. V. Popovich & J. Benedikt, 645-656. Wien.

Melgani, F. & L. Bruzzone (2004). Classification of hyperspectral remote sensing images with Support Vector Machines. In: IEEE Transactions on Geoscience and Remote Sensing, 42**,** 1778 –1790.

Myint, S. W. & G. S. Okin (2009). Modelling land-cover types using multiple endmember spectral mixture analysis in a desert city. In: International Journal of Remote Sensing, 30**,** 2237 - 2257.

N

Niemeyer, I., P. R. Marpu & S. Nussbaum (2008). Change detection using object features. In: Object-based image analysis spatial concepts for knowledge-driven remote sensing applications, eds. T. Blaschke, S. Lang & G. Hay, 185-201. Berlin. Springer.

O

Openshaw, S. & P. Taylor (1979). A million or so correlation coefficients: three experiments on the modifiable area unit problem. In: Statistical Applications in the Spatial Sciences, ed. N. Wrigley, 127-144. London. Pion.

P

Pohl, C. & J. L. Van Genderen (1998). Review article Multisensor image fusion in remote sensing: concepts, methods and applications. In: International Journal of Remote Sensing, 19**,** 823 - 854.

Powell, R. L., D. A. Roberts, P. E. Dennison & L. L. Hess (2007). Sub-pixel mapping of urban land cover using multiple endmember spectral mixture analysis: Manaus, Brazil. In: Remote Sensing of Environment, 106**,** 253-267.

Powell, S. L., W. B. Cohen, Z. Yang, J. D. Pierce & M. Alberti (2008). Quantification of impervious surface in the Snohomish Water Resources Inventory Area of Western Washington from 1972-2006. In: Remote Sensing of Environment, 112**,** 1895-1908.

Prasada Mohapatra, R. & C. Wu (2007). Subpixel Imperviousness Estimation with IKONOS Imagery. In: Remote Sensing of Impervious Surfaces. CRC Press.

Pu, R., P. Gong, R. Michishita & T. Sasagawa (2008). Spectral mixture analysis for mapping abundance of urban surface components from the Terra/ASTER data. In: Remote Sensing of Environment, 112**,** 939-954.

Q

Quang, N. & H. Detlef Kammeier (2002). Changes in the political economy of Vietnam and their impacts on the built environment of Hanoi. In: Cities, 19**,** 373-388.

R

Richards, J. A. & X. Jia (2006). Remote sensing digital image analysis an introduction. Berlin. Springer.

Richter, R. (2008). Atmospheric/Topographic Correction for Satellite Imagery (ATCOR-2/3 User Guide, Version 7.0 BETA)

Ridd, M. K. (1995). Exploring a V-I-S (vegetation-impervious surface-soil) model for urban ecosystem analysis through remote sensing: comparative anatomy for cities. In: International Journal of Remote Sensing, 16**,** 2165 - 2185.

Riedel, T., C. Tiel & C. Schmullius (2008). Fusion of multispectral optical and SAR images towards operational land cover mapping in Central Europe. In: Object-based image analysis spatial concepts for knowledge-driven remote sensing applications, eds. T. Blaschke, S. Lang & G. Hay, 493-511. Berlin. Springer.

Rogan, J., J. Franklin, D. Stow, J. Miller, C. Woodcock & D. Roberts (2008). Mapping land-cover modifications over large areas: A comparison of machine learning algorithms. In: Remote Sensing of Environment, 112**,** 2272-2283.

Ryerson, R. A., S. A. Morain, A. M. Budge, F. M. Henderson, A. J. Lewis, A. N. Rencz & American Society for Photogrammetry and Remote Sensing. (1998).

Manual of remote sensing: Principles and applications of imaging radar. New York. Wiley.

S

Schneider, A., M. A. Friedl & D. Potere (2010). Mapping global urban areas using MODIS 500-m data: New methods and datasets based on 'urban ecoregions'. In: Remote Sensing of Environment, In Press, Corrected Proof.

Schölkopf, B. & A. J. Smola (2002). Learning with kernels: support vector machines, regularization, optimization, and beyond. Cambridge, Mass. MIT Press.

Schölkopf, B. & A. J. Smola (2004). A tutorial on support vector regression. In: Statistics and Computing, 14**,** 199-222.

Siedentop, S. & S. Fina (2008). Urban Sprawl beyond Growth: from a Growth to a Decline. Perspective on the Cost of Sprawl. In: Paper prepared for the 44th Isocarp Conference. Dalian, China.

T

Taubenböck, H. (2008). Vulnerabilitätsabschätzung der erdbebengefährdeten Megacity Istanbul mit Methoden der Fernerkundung. Würzburg. Julius-Maximilians Universität Würzburg.

Tibaijuka, A. (2008). Address by Mrs. Anna Tibaijuka, Under-Secretary-General and Executive Director of UN-HABITAT. In: Forum on Sustainable Urbanization in the Information Age. United Nations Headquarters, New York. UN/Habitat. The United Nations Human Settlements Programme.

Tucker, C. J. (1979). Red and photographic infrared linear combinations for monitoring vegetation. In: Remote Sensing of Environment, 8**,** 127-150.

Tzotsos, A. (2006). A support vector machine approach for object based image analysis.

Tzotsos, A. & D. Argialas (2008). Support Vector Machine Classification for Object-Based Image Analysis. In: Object-based image analysis spatial concepts for knowledge-driven remote sensing applications, eds. T. Blaschke, S. Lang & G. Hay, 663-677. Berlin. Springer.

U

Ulaby, F. T., F. Kouyate, B. Brisco & T. H. Lee Williams (1986). Textural Information in SAR Images. In: IEEE Transactions on Geoscience and Remote Sensing, 24**,** 235-245.

V

Van de Voorde, T., T. De Roeck & F. Canters (2009). A comparison of two spectral mixture modelling approaches for impervious surface mapping in urban areas. In: International Journal of Remote Sensing, 30**,** 4785-4806.

Van der Linden, S. & P. Hostert (2009). The influence of urban structures on impervious surface maps from airborne hyperspectral data. In: Remote Sensing of Environment, 113, 2298-2305.

Vapnik, V. N. (1995). The nature of statistical learning theory. New York. Springer.

Vapnik, V. N. (1998). Statistical learning theory. New York. Wiley.

W

Webster, R. & M. A. Oliver (2007). Geostatistics for environmental scientists. Chichester. John Wiley & Sons.

Weng, Q. (2007). Remote Sensing of Impervious Surfaces: An Overview. In: Remote Sensing of Impervious Surfaces. CRC Press.

Weng, Q., X. Hu & H. Liu (2009). Estimating impervious surfaces using linear spectral mixture analysis with multitemporal ASTER images. In: International Journal of Remote Sensing, 30, 4807-4830.

Weng, Q., X. Hu & D. Lu (2008). Extracting impervious surfaces from medium spatial resolution multispectral and hyperspectral imagery: a comparison. In: International Journal of Remote Sensing, 29, 3209 - 3232.

Weng, Q. & D. Lu (2009). Landscape as a continuum: an examination of the urban landscape structures and dynamics of Indianapolis City, 1991-2000, by using satellite images. In: International Journal of Remote Sensing, 30, 2547 - 2577.

Wilson, J. S., M. Clay, E. Martin, D. Stuckey & K. Vedder-Risch (2003). Evaluating environmental influences of zoning in urban ecosystems with remote sensing. In: Remote Sensing of Environment, 86, 303-321.

Windler, H. & E. Winkler (1950). Zur quantitativen Bestimmung von Siedlungseinheiten. In: Plan und Ortsplanung, 6, 180 ff.

Wu, C. (2009). Quantifying high-resolution impervious surfaces using spectral mixture analysis. In: International Journal of Remote Sensing, 30, 2915 - 2932.

X

Xian, G. (2007). Mapping Impervious Surfaces Using Classification and Regression Tree Algorithm. In: Remote Sensing of Impervious Surfaces. CRC Press.

Xian, G. & M. Crane (2005). Assessments of urban growth in the Tampa Bay watershed using remote sensing data. In: Remote Sensing of Environment, 97, 203-215.

Y

Yang, L. M., C. Q. Huang, C. G. Homer, B. K. Wylie & M. J. Coan (2003). An approach for mapping large-area impervious surfaces: synergistic use of Landsat-7 ETM+ and high spatial resolution imagery. In: Canadian Journal of Remote Sensing, 29, 230-240.

Yang, T. C. (2010). Modifiable Areal Unit Problem. In: Resource Documents. Oswald Tower, Pennsylvania. Population Research Institute (PRI). Pennsylvania State University.

Yuan, F. & M. E. Bauer (2007). Comparison of impervious surface area and normalized difference vegetation index as indicators of surface urban heat island effects in Landsat imagery. In: Remote Sensing of Environment, 106, 375-386.

Internet

D

DIGITALGLOBE (2006). QuickBird. Available at: http://www.digitalglobe.com. S*tatus: 20.05.2009*.

E

Eoearth (2010). Land-use and land-cover change. Available at: http://eoearth.org/article/Land-use_and_land-cover_change S*tatus: 08.03.2010*.

G

GSOV (2010). General Statistics Office Vietnam. Available at: http://www.gso.gov.vn *Status: 10.05.2010*.

R

RST (2010). Remote Sensing Tutorial of the National Aerotnautics and Space Administration (NASA). Available at: http://rst.gsfc.nasa.gov/Sect13/Sect13_2.html *Status: 26.04.2010*.

S

SATIMAGINGCORP (2010). Satellite Imaging Corporation. Available at: http://www.satimagingcorp.com/satellite-sensors/quickbird.html *Status: 15.06.2010*.

U

UN-HABITAT (2009). Available at: http://esa.un.org/unpd/wup/index.htm *Status: 15.06.2010*.

W

WISDOM (2009). Available at: http://hwww.wisdom.caf.dlr.de *Status: 25.08.2010*.

Annex B

Change Detection Examples

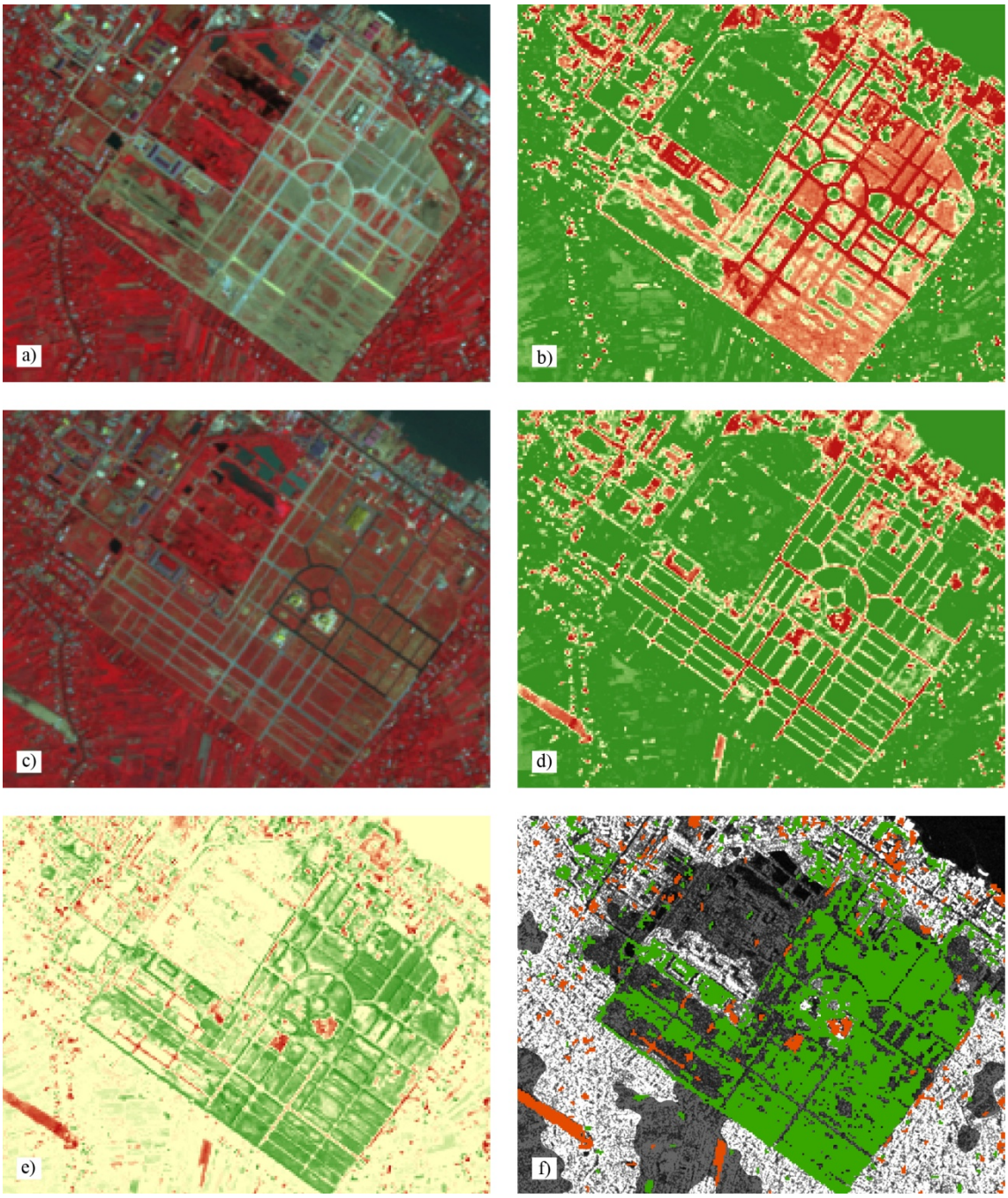

Fig. B-1: Change detection example 1: developing land for building construction

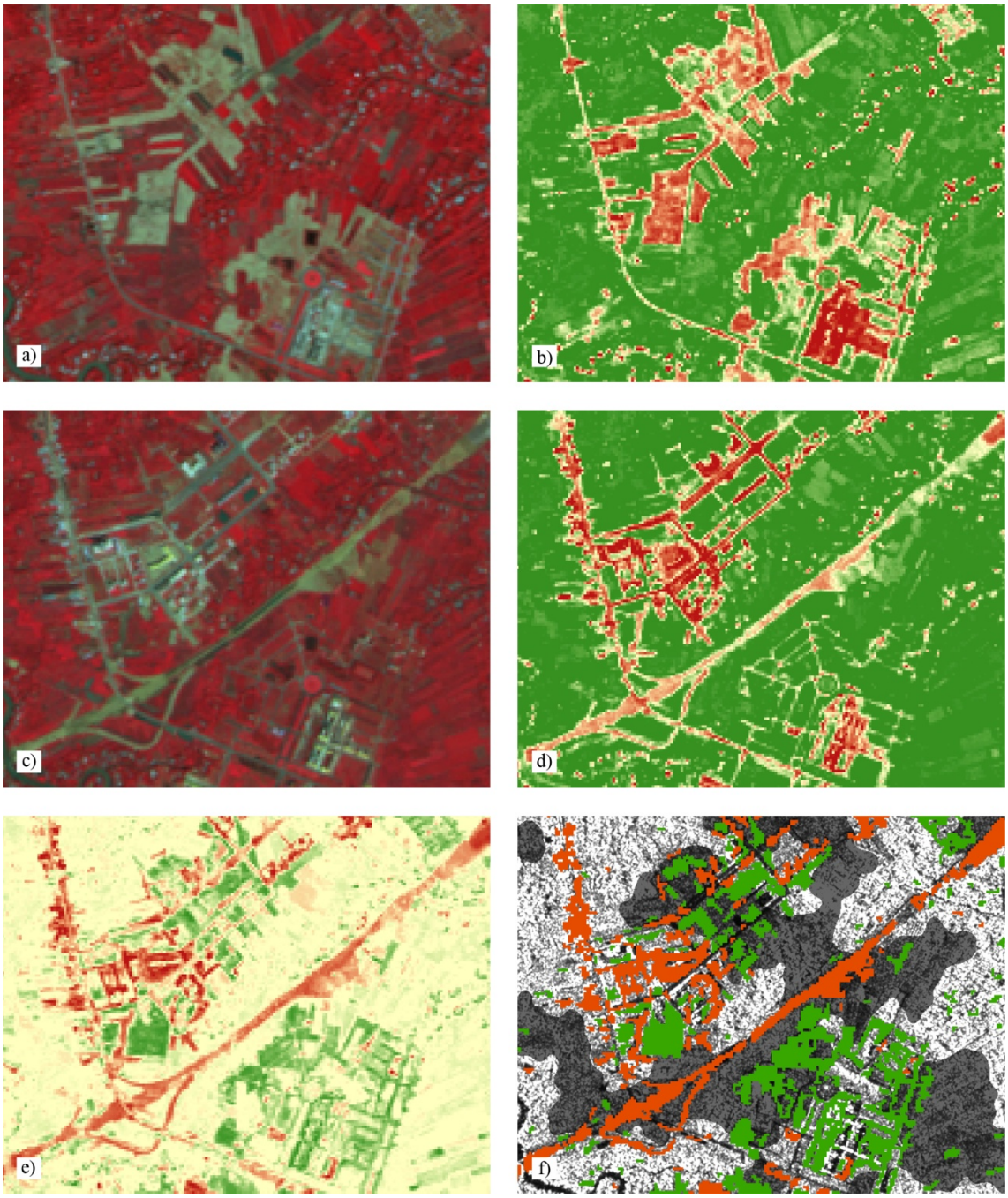

Fig. B-2: Change detection example 2: developing land for building construction, overland routs

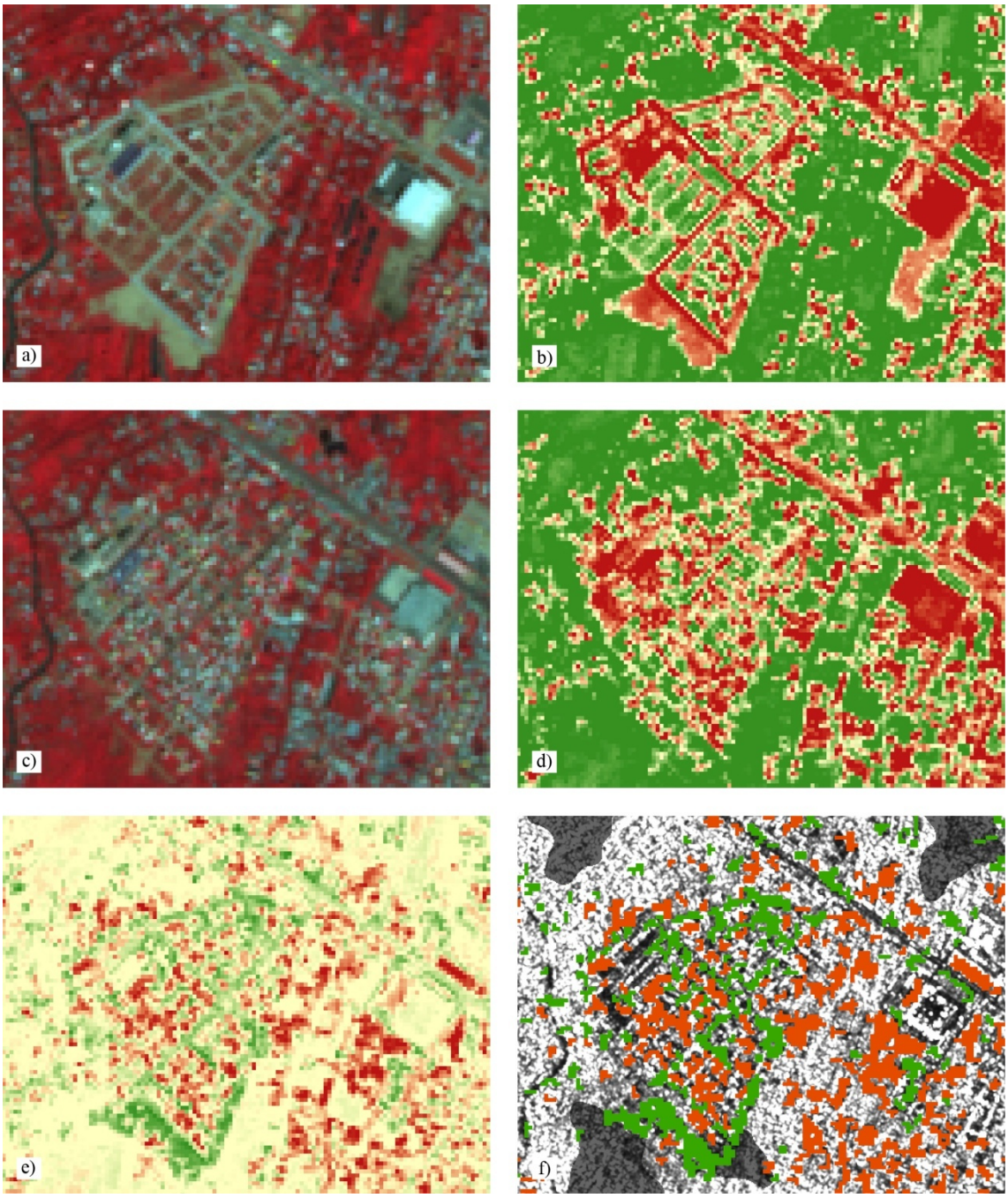

Fig. B-3: Change detection example 3: new residential area

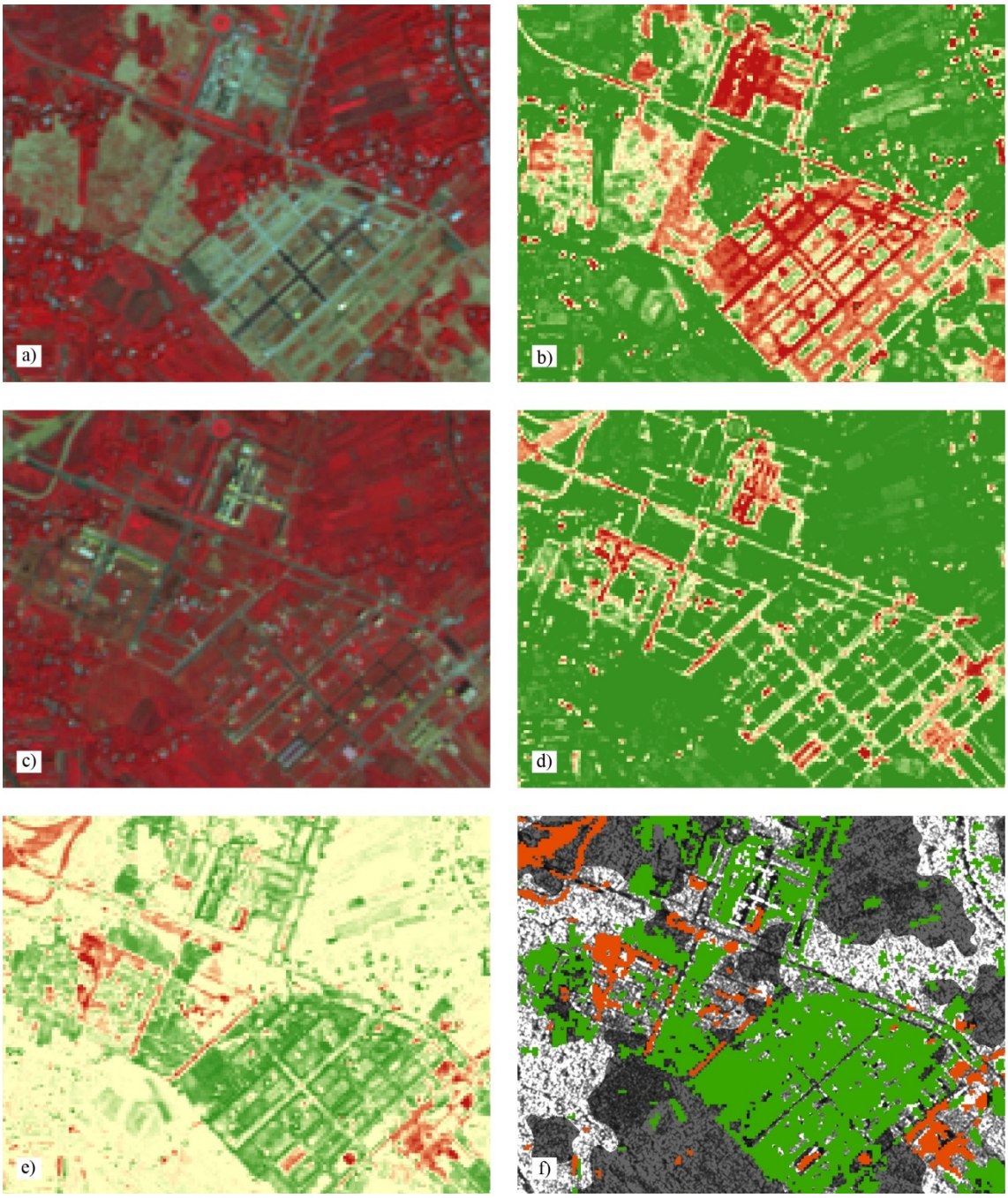

Fig. B-4: Change detection example 4: developing land for building construction

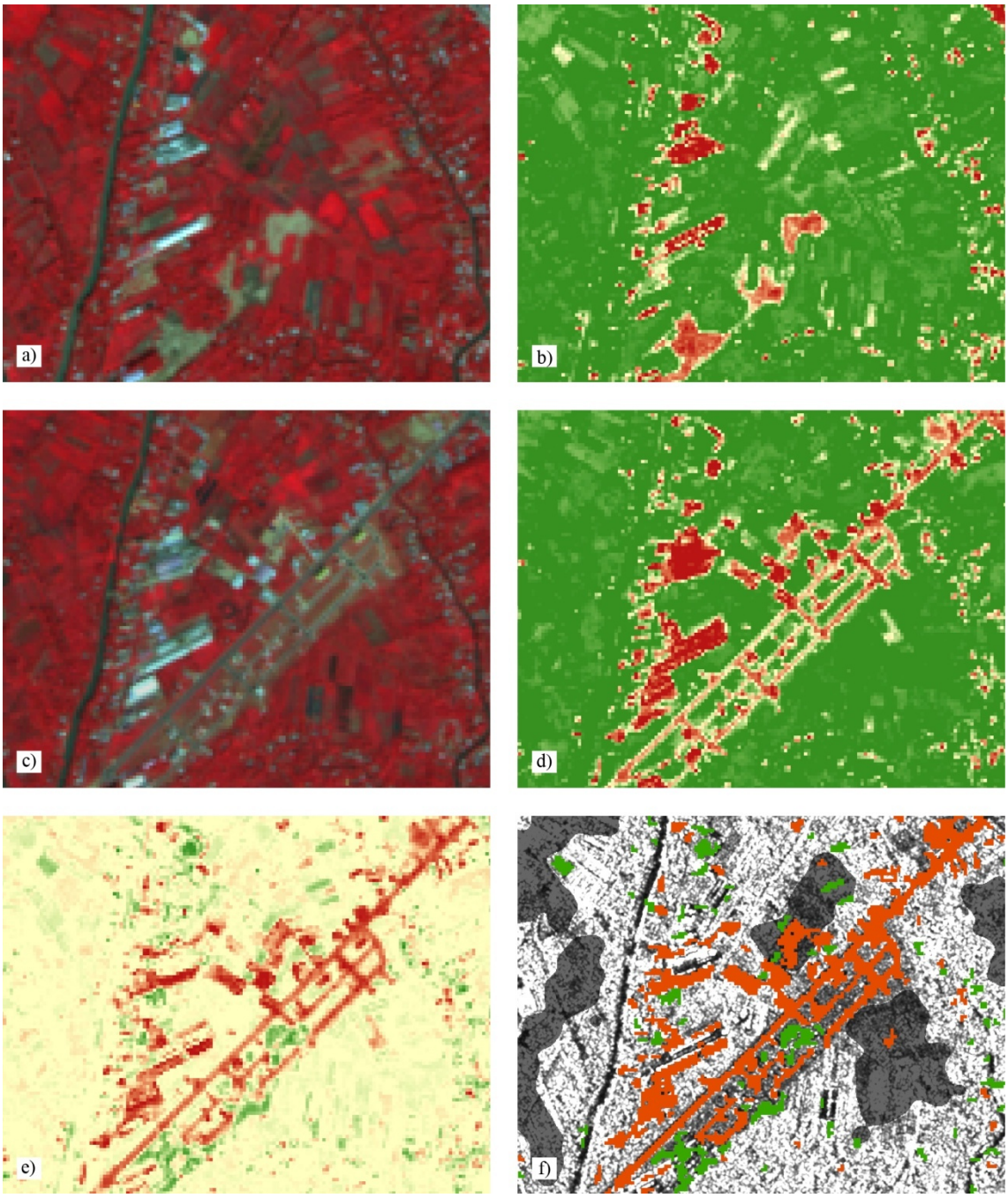

Fig. B-5: Change detection example 5: new road and building construction

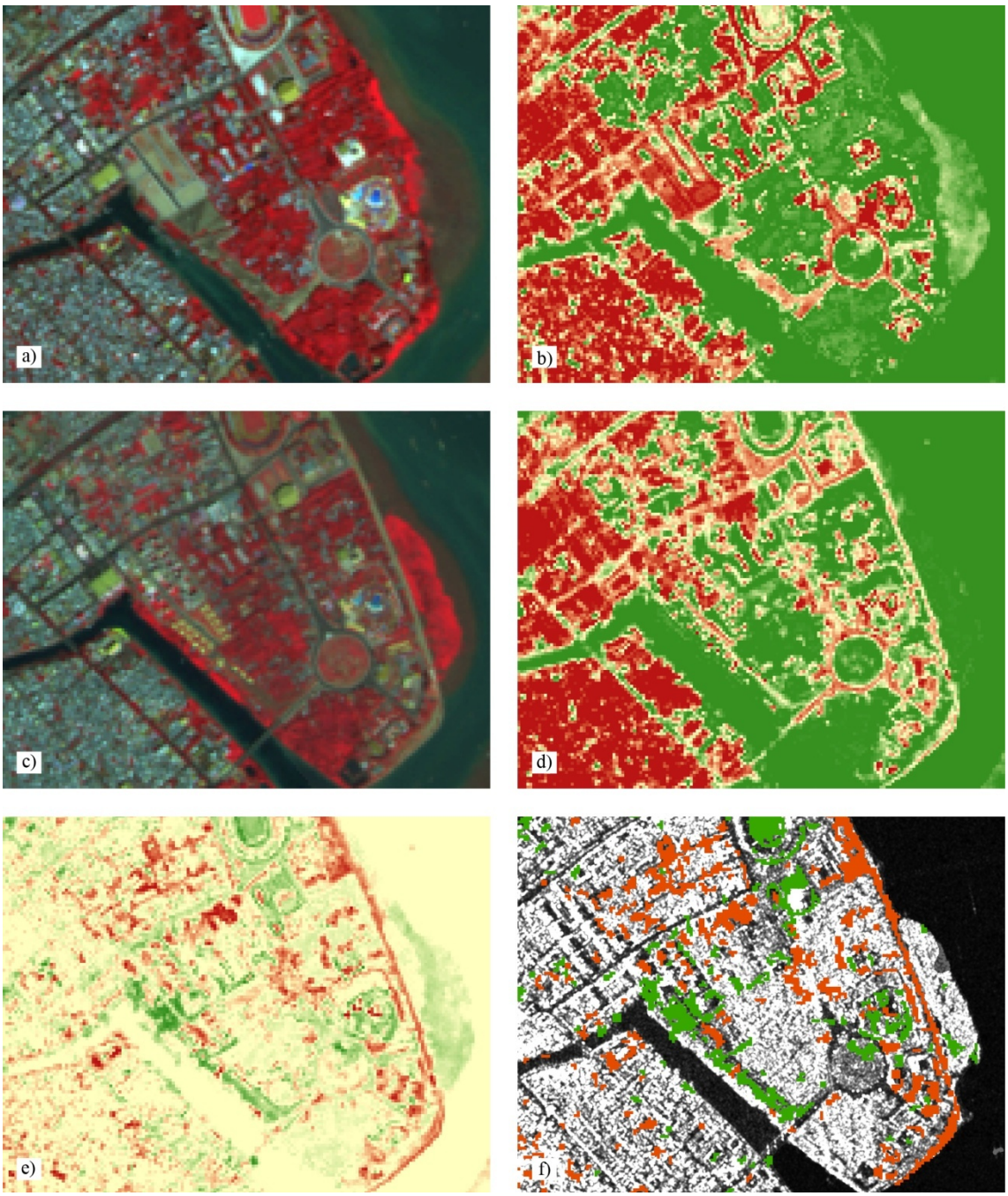

Fig. B-6: Change detection example: new building construction

Annex C

IS Statistics per Commune

Table C-1: IS statistics for each commune

ID	COMMUNE	IMPERVIOUS SURFACE 2005	IMPERVIOUS SURFACE 2009	IMPERVIOUS SURFACE INCREASE 2005-2009
1	Dong Thanh	8,7%	6,2%	0,8%
2	Truong Long A	4,7%	3,9%	1,2%
3	Truong Long Tay	-	5,0%	-
4	Phuong An Hoa	45,4%	49,7%	6,8%
5	Phuong Thoi Binh	61,0%	67,0%	6,3%
6	Phuong An Nghiep	44,9%	52,0%	7,0%
7	Phuong An Cu	69,2%	78,0%	7,4%
8	Phuong An Hoi	75,7%	78,8%	3,9%
9	Phuong An Phu	63,7%	72,2%	7,0%
10	Phuong Long Hoa	6,7%	8,2%	3,0%
11	Giai Xuan	5,0%	5,6%	1,2%
12	Phuong Long Tuyen	6,0%	6,7%	1,5%
13	My Khanh	6,9%	6,9%	1,2%
14	Phuong Thot Not	20,4%	23,0%	5,3%
15	Phuong Trung Nhut	12,5%	10,3%	2,6%
16	Thanh Loc	9,5%	6,6%	1,3%
17	Trung Hung	10,9%	8,0%	1,9%
18	Phuong Trung Kien	10,0%	10,4%	3,4%
19	Dinh Mon	8,5%	6,9%	1,5%
20	Tan Thoi	5,4%	5,4%	1,1%
21	Phuong Tan An	69,9%	71,5%	3,5%
22	Phuong An Lac	67,0%	66,6%	3,0%
23	Phuong Xuan Khanh	37,9%	40,6%	6,1%
24	Phuong Hung Loi	36,2%	43,1%	9,8%
25	Phuong Ba Lang	14,1%	13,1%	2,3%
26	Thanh Thang	-	-	-
27	Vinh Trinh	10,8%	7,1%	2,7%
28	Phuong Hung Thanh	8,0%	7,7%	1,6%
29	Phuong Hung Phu	20,2%	16,7%	4,1%
30	Phuong Thoi An	6,8%	6,1%	1,7%
31	Phuong Phuoc Thoi	8,9%	13,1%	6,0%

32	Nhon Nghia	4,4%	5,2%	0,9%
33	Truong Thanh	6,2%	5,0%	0,9%
34	Truong Long	5,3%	4,8%	1,0%
35	Phuong Thoi An Dong	5,2%	6,1%	1,8%
36	Phuong Truong Lac	5,9%	5,8%	1,1%
37	Truong Xuan	8,4%	6,3%	1,2%
38	Truong Xuan A	9,0%	4,6%	1,1%
39	Dong Thuan	7,4%	5,2%	1,2%
40	Dong Binh	7,7%	4,1%	0,8%
41	Thi tran Co Do	11,4%	11,6%	3,2%
42	Thanh Phu	9,2%	4,8%	1,9%
43	Thoi Thanh	8,6%	6,6%	1,5%
44	Thi tran Thoi Lai	8,8%	10,1%	3,4%
45	Phuong Phu Thu	14,5%	-	-
46	Phuong Thoi Thuan	13,9%	13,2%	3,1%
47	Phuong Tan Loc	7,8%	4,8%	1,4%
48	Phuong Binh Thuy	29,7%	27,9%	4,3%
49	Phu An	6,7%	-	-
50	Tan Phu Thanh	7,2%	6,2%	1,2%
51	Nhon Nghia A	3,5%	5,0%	0,8%
52	Phuong Cai Khe	27,3%	28,5%	5,4%
53	Thanh Xuan	3,9%	4,2%	0,3%
54	Thi tran Rach Goi	-	5,5%	-
55	Thi tran Cai Tac	18,3%	-	-
56	Thoi Hung	6,7%	4,7%	1,1%
57	Thoi Dong	5,8%	4,6%	0,8%
58	Dong Hiep	7,2%	5,3%	1,1%
59	Thoi Lai	7,2%	5,4%	1,5%
60	Xuan Thang	6,6%	3,8%	0,7%
61	Phuong Long Hung	8,6%	7,8%	2,5%
62	Phuong Thoi Long	7,3%	8,5%	2,9%
63	Phuong Thoi Hoa	6,8%	6,3%	1,3%
64	Phuong Chau Van Liem	16,0%	17,9%	3,8%
65	Phuong Thuan Hung	9,4%	8,5%	2,2%
66	Phuong Tan Hung	8,7%	6,0%	1,4%
67	Trung An	14,5%	12,2%	2,9%
68	Trung Thanh	12,9%	9,9%	3,1%
69	Thanh Tien	-	6,6%	-
70	Phuong An Khanh	15,6%	22,2%	9,1%
71	Phuong An Binh	15,0%	16,7%	4,4%
72	Phuong Tra Noc	25,6%	32,4%	9,0%
73	Phuong Tra An	10,7%	12,2%	3,3%
74	Phuong Bui Huu Nghia	4,9%	2,9%	0,6%
75	Phuong An Thoi	29,4%	31,4%	5,9%
76	Phuong Thuong Thanh	6,6%	7,2%	1,9%
77	Phuong Le Binh	31,7%	35,0%	6,0%
78	Nhon Ai	6,1%	6,4%	1,4%
79	Thi tran Phong Dien	9,4%	13,0%	4,4%
80	Thanh An	-	8,9%	-
81	Thi tran Thanh An	-	11,7%	-
82	Thanh My	5,7%	3,6%	0,5%

83	Thanh Quoi	-	5,4%	-
84	Thi tran Vinh Thanh	-	10,9%	-

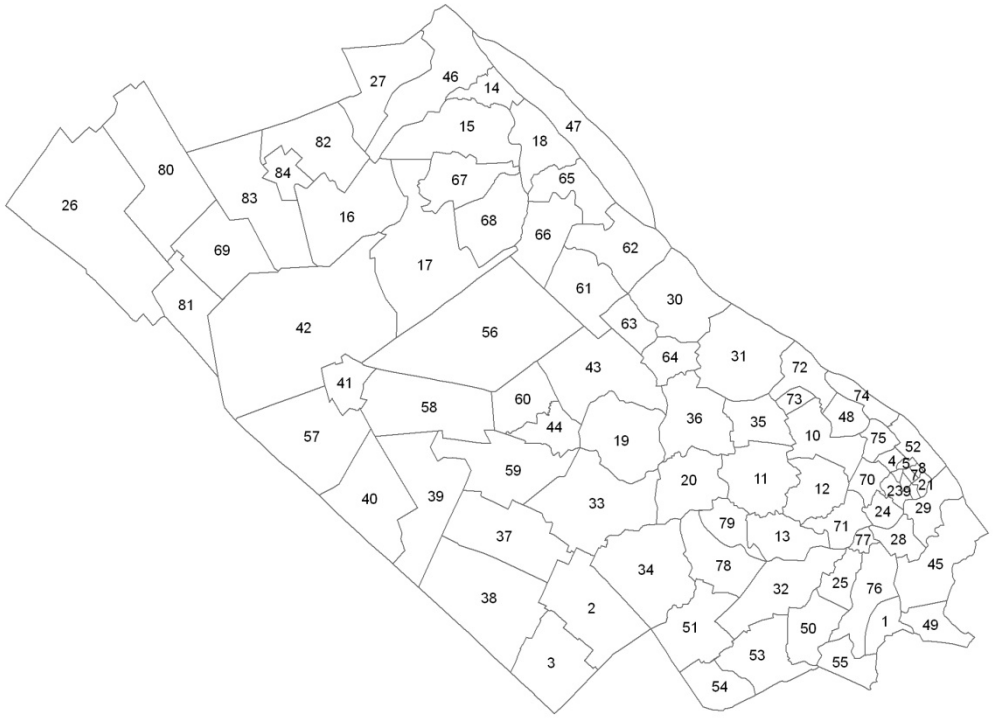

Fig. C-1: Overview of the communes in Can Tho Province (indexed according to Table C-1)

Annex D

Validation Results

Table D-1: Error Matrix resulting from validation of the QB land-cover classification

		REFERENCE DATA				CLASSIFIED TOTALS
		vegetation	sealed	water	bare soil	
Classified Data	vegetation	156	0	1	6	163
	sealed	0	111	0	5	116
	water	0	0	92	0	92
	bare soil	1	5	0	66	72
Reference totals		157	116	93	77	443

Table D-2: Validation results for settlement classification in the urban validation subset

VALIDATION URBAN		REFERENCE DATA				
		Settlement	No-settlement	Total	User's accuracy	
Classified Data	Settlement	236	60	316	**74,68%**	S25
	No-settlement	24	260	284	**91,55%**	
	Total	260	320	600		
	Producer's accuracy	**90,77%**	**81,25%**		**82,67%**	
	Settlement	295	21	316	**93,35%**	S50
	No-settlement	47	237	284	**83,45%**	
	Total	342	258	600		
	Producer's accuracy	**86,25%**	**91,86%**		**88,67%**	
	Settlement	307	9	316	**97,15%**	S75
	No-settlement	77	207	284	**72,89%**	
	Total	384	216	600		
	Producer's accuracy	**79,95%**	**95,83%**		**85,67%**	
	Settlement	313	3	316	**99,05%**	S100
	No-settlement	112	172	284	**60,56%**	
	Total	425	175	600		
	Producer's accuracy	**73,65%**	**98,29%**		**80,83%**	

Table D-3: Validation results for settlement classification in the rural validation subset

VALIDATION RURAL		REFERENCE DATA				
		Settlement	No-settlement	Total	User's accuracy	
Classified Data	**Settlement**	64	49	113	**56, 64%**	**S25**
	No-settlement	4	483	487	**99,18%**	
	Total	68	532	600		
	Producer's accuracy	**94,11%**	**90,79%**		**91,27%**	
	Settlement	87	26	113	**76,99%**	**S50**
	No-settlement	11	476	487	**97,74%**	
	Total	98	502	600		
	Producer's accuracy	**88,78%**	**94,82%**		**93,83%**	
	Settlement	96	17	113	**84,96%**	**S75**
	No-settlement	28	459	487	**94,25%**	
	Total	124	476	600		
	Producer's accuracy	**77,42%**	**96,43%**		**92,50%**	
	Settlement	107	6	113	**94,69%**	**S100**
	No-settlement	49	438	487	**89,93%**	
	Total	156	444	600		
	Producer's accuracy	**68,59%**	**98,65%**		**90,83%**	

Table D-4: SVR validation results for mixed pixels

	COUNT	MAX NEGATIVE DEVIATION	MAX POSITIVE DEVIATION	MEAN	ABSOLUTE MEAN	ABSOLUTE STANDAR DEVIATION
w1b0 mixed pixels						
vegetation	1567	-0,53	0,90	0,08	0,16	0,13
sealed surface	1646	-0,90	0,45	-0,10	0,15	0,13
water	257	-1,00	0,30	-0,18	0,21	0,25
bare soil	258	-0,14	0,92	0,33	0,33	0,23
w1b1mixed pixels						
vegetation	1567	-0,53	0,82	0,10	0,17	0,14
sealed surface	1646	-0,70	0,50	-0,06	0,13	0,11
water	257	-1,00	0,26	-0,18	0,21	0,26
bare soil	258	-0,94	0,43	-0,16	0,21	0,17
w1b05 mixed pixels						
vegetation	1567	-0,53	0,81	0,09	0,16	0,13
sealed surface	1646	-0,69	0,47	-0,09	0,14	0,11
water	257	-1,00	0,27	-0,18	0,21	0,25
bare soil	258	-0,54	0,65	0,07	0,17	0,13
w0b0 mixed pixels						
vegetation	1567	-0,51	0,85	0,08	0,15	0,13
sealed surface	1646	-0,89	0,47	-0,13	0,17	0,14
water	257	-0,47	0,93	0,22	0,23	0,22
bare soil	258	-0,15	0,88	0,31	0,32	0,22
w0b1 mixed pixels						
vegetation	1567	-0,44	0,80	0,09	0,16	0,14
sealed surface	1646	-0,89	0,50	-0,10	0,15	0,13
water	257	-0,47	0,95	0,22	0,24	0,22
bare soil	258	-0,94	0,42	-0,16	0,21	0,17
w0b05 mixed pixels						
vegetation	1567	-0,44	0,80	0,09	0,15	0,13

sealed surface	1646	-0,89	0,47	-0,11	0,16	0,13
water	257	-0,45	0,93	0,22	0,24	0,21
bare soil	258	-0,54	0,58	0,06	0,16	0,12

Table D-5: SVR validation results for pure pixels

	COUNT	MAX NEGATIVE DEVIATION	MAX POSITIVE DEVIATION	MEAN	ABSOLUTE MEAN	ABSOLUTE STANDAR DEVIATION
w1b0 pure pixels						
vegetation	5523	-0,16	1,00	0,04	0,04	0,10
sealed surface	3324	-1,00	0,65	-0,08	0,08	0,12
water	1616	-1,00	0,02	-0,08	0,08	0,19
bare soil	261	0,00	0,97	0,50	0,50	0,20
w1b1 pure pixels						
vegetation	5523	-0,07	1,00	0,06	0,06	0,12
sealed surface	3324	-0,93	0,09	-0,05	0,05	0,08
water	1616	-1,00	0,02	-0,07	0,07	0,19
bare soil	261	-1,00	0,00	-0,20	0,20	0,19
w1b05 pure pixels						
vegetation	5523	-0,13	1,00	0,05	0,05	0,11
sealed surface	3324	-0,91	0,26	-0,07	0,07	0,09
water	1616	-1,00	0,02	-0,09	0,09	0,19
bare soil	261	-0,50	0,47	0,12	0,18	0,11
w0b0 pure pixels						
vegetation	5523	-0,16	1,00	0,03	0,03	0,08
sealed surface	3324	-0,91	0,62	-0,09	0,10	0,13
water	1616	-0,79	1,00	0,03	0,04	0,11
bare soil	261	0,00	0,92	0,48	0,48	0,17
w0b1 pure pixels						
vegetation	5523	-0,09	1,00	0,05	0,05	0,11
sealed surface	3324	-0,94	0,09	-0,07	0,07	0,11
water	1616	-0,77	1,00	0,04	0,04	0,11
bare soil	261	-1,00	0,00	-0,20	0,20	0,19
w0b05 pure pixels						
vegetation	5523	-0,13	1,00	0,04	0,04	0,09
sealed surface	3324	-0,91	0,27	-0,08	0,08	0,12
water	1616	-0,77	1,00	0,04	0,04	0,11
bare soil	261	-0,50	0,43	0,11	0,17	0,10

Eidesstattliche Erklärung

Hiermit versichere ich an Eides statt, dass ich die vorliegende Arbeit ohne fremde Hilfe und ohne Benutzung anderer als der angegebenen Quellen und Hilfsmittel angefertigt und die den benutzten Quellen wörtlich oder inhaltlich entnommenen Stellen als solche kenntlich gemacht habe.

Diese Arbeit wurde in gleicher oder ähnlicher Form noch bei keiner anderen Prüferin/ keinem anderen Prüfer als Prüfungsleistung eingereicht.

_____

Patrick Leinenkugel